UNIVERSITÀ DEGLI STUDI DI PADOVA

UNIVERSITAS STUDII PATAVINI

FACOLTÀ DI INGEGNERIA
CORSO DI LAUREA MAGISTRALE IN
INGEGNERIA DEI MATERIALI

SYNTHESIS AND CHARACTERIZATION OF SUBSTITUTED APATITES FOR BIOMEDICAL APPLICATIONS

Tesi in
MATERIALI NANOSTRUTTURATI
NANOSTRUCTURED MATERIALS

Relatore:
Prof.
ALESSANDRO MARTUCCI

Presentata da:
RICCARDO GALLO

Correlatore:
Prof.
JEAN-MARIE NEDELEC

Controrelatore:
Prof.
MASSIMO GUGLIELMI

Sessione II, 22/03/2011

Anno Accademico 2010 – 2011

A mia madre, mio padre, mio fratello

Declaration

All the content of this thesis, when not explicitly cited, is my original work. Data were collected from June, 15^{th} to December, 15^{th} 2010 in the laboratories of the LMI (Laboratiore des Metériaux Inorganiques) in the ENSCCF - Université Blaise Pascal (Ecole Nationale Superieure de Chimie de Clermont-Ferrand, France). The general guidelines reported by Mimi Zeiger in "Essentials of Writing Biomedical Research Papers", 2^{nd} ed., McGraw-Hill, (2000) have been followed in editing this work. This thesis has been written with the 1.6.6.1 version of LyX - the document processor.

Abstract

Hydroxyapatite ($Ca_{10}(PO_4)_6OH_2$) is a very well known ceramic biomaterial for its great similarity with the mineral part of the human bone. To increment its bioactivity, Ca^{2+}, PO_4^{3-} and OH^- ions can be substituted with several species. Particularly, OH^- can be easily replaced by F^- to obtain the fluorapatite mineral, which is very suitable for oral applications. Ca^{2+} can be replaced by other alkaline earth metals. Sr^{2+} has been studied as substitute in recent literature and its presences resulted in improvement the overall biological properties.

In the present work, F-substituted hydroxyapatites nanopowders with general formula $Ca_{10}(PO_4)_6OH_{2-x}F_x$ have been synthesized by a simple co-precipitation method ($0 \leq x \leq 2$) and XRD/Rietveld refinement characterization has been performed to understand the influence of the F^- addition on structural properties such as lattice parameters, crystal size, phase composition, and crystallinity degree. An original ion-exchange chromatography characterization set-up has been developed to assess the real content of fluoride in the samples. Powders with Ca/P molar ratios different from $1.\bar{6}$ have been synthesized in order to investigate the role of fluoride in the apatite phase stabilization. The Ca/P=1.50 ratio has been selected to obtain β-TCP/F-enriched hydroxyapatite biphasic calcium phosphate (BCP).

Codoped Sr-F hydroxyapatite with general formula $Ca_{10-y}Sr_y(PO_4)_6OH_{2-x}F_x$ have been synthesized with a nominal molar ratio equal to 1.67 and their structural characterization has been performed to understand the influence of the double doping on the phase composition and on the structural parameters. A preferential Sr substitution in the Ca2 site has been found through the Rietveld refinement of cations sites occupancy factors.

A simple method to fluorinate calcium phosphates powders with Ca/P=1.67 and 1.50 in aqueous solution has been developed. β-TCP is found to be converted in F-rich hydroxyapatite in neutral pH conditions.

The influence of the substitution on ion release properties has been studied through low-pH accelerated tests, and investigations on the stoichiometry of the dissolution have been discussed.

Contents

List of Figures

Part I

State of the art

Chapter 1

Literature review

1.1 Biomaterials and bioceramics

There's been a huge discussion about the statement of a proper definition of *biomaterial*. In the '70s, when biomaterials science started to develop, a biomaterial was intended as a material that was chemically *inert* towards the rest of the organism in which it was implanted. But the first large-scale known *bioactive* material, Bioglass 45S5®, was able to operate a positive interaction with the biological environment: the concept of *bioactivity* was born, and this positive interaction led to the conclusion that a biomaterial should not just be *inert*, not only *non-dangerous* for the living tissues, but preferably infer a positive response from the part of the organism.

A useful definition for the term "biomaterial" comes out from the proceedings of the II Consensus Conference of the European Society of Biomaterials:

> *"A biomaterial is a material intended to interface with biological systems to evaluate, treat, augment or replace any tissue, organ or function of the body"*[1]

It's clear that a biomaterial is *designed* to be implanted in a living organism, or to interact in some way with the living tissues. The definition is particularly significant because it states the importance of the interface between the material and the living tissue: that's why the surface of the biomaterial should be carefully studied, and designed not to result in a negative reaction by the organism.

[1] Proceedings of the II Consensus Conference of the European Society of Biomaterials, Chester (UK), March 1986

One can define a biomaterial also as "any natural or artificial material which is supposed to get in touch with living tissues without causing negative reactions on itself or on the tissues, and is not *completely* disintegrated during this interaction". This definition includes the materials used to store and transport organic fluids, because any of them gets in contact at least with human blood, which is definitely a tissue. At the same time, this definition underlines that a biomaterial must have the specific characteristic to be *biocompatible*, i.e. not to cause chronic inflammation or rejection. Biocompatibility is actually the first request for any biomaterial. The previous definition excludes legitimately drugs from the world of biomaterials, but theoretically it excludes also those completely resorbable polymers used for drug delivery systems which are able to dissolve completely at determined times after the insertion in the organism (PGA/PLA, Ialuronic acid).

In the present work we'll focus on ceramics biomaterials, also called bioceramics, but a general panoramic view on the variety of biomaterials classes will be offered below.

1.1.1 Biomaterials families

The huge world of biomaterials is resumed in figure 1.1.1.

One can classify the different kinds of biomaterials according to chemical composition, effects of the biological interaction on the material, effects of the material on the biological environment, or type of interaction between the material and the organic tissue.

When a biomaterial is considered from a strictly chemical point of view, it could belong to one of the classical materials categories: ceramics (and glasses), metals, polymers or composites. Each category finds specific biomedical application. Metals are commonly used to replace hard load-bearing tissues, and the most famous example is represented by the Titanium alloy (Ti6Al4V) for femur substitution. Composites are suitable for this application too, because of their elastic behavior, which makes these materials more similar than metals to the human bone. Composites find also very important applications in replacing soft tissues, and their relatively recent addition to the class of biomaterials opens wide perspective for tissue regeneration. Polymers are commonly used as surgical suture devices, and one can exploit their chemical features as drug-delivery systems, as mentioned before. Ceramics have been widely used as bore replacement or bone grafts in non-load-bearing applications, because of their brittleness. The main applications of bioceramics are set in reconstruction of small bones, as for example in maxillofacial surgery, dental applications,

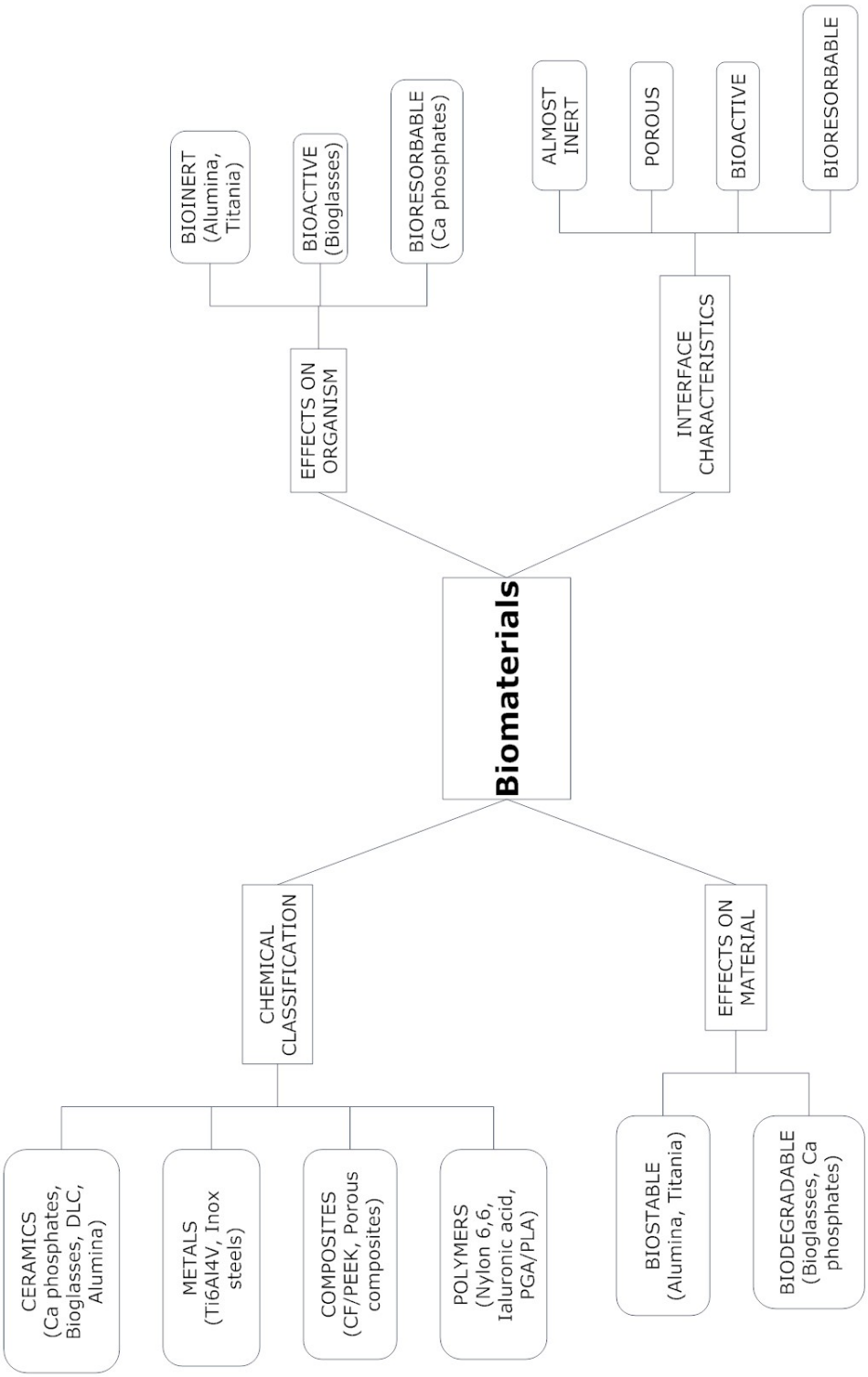

Figure 1.1.1: The classification of biomaterials

and replacement of ear components. When used as coatings, they enhance biocompatibility of the underneath material, and they can be used in load-bearing applications when coupled with other biomaterials.

A biomaterial can either be biostable when inserted in the biological environment, i.e. it has no significant modifications on its surface or bulk, or biodegradable. Biostability is not always desired because the organism often reacts to the recognition of a "non-self" item with the encapsulation in a fibrous tissue, which can limit the efficiency of the device. A controlled degradation, often followed by the conversion of the material in a "self-like" tissue is more suitable and represents the real challenge for the biomaterials designer.

Organism can be more or less influenced by the material's insertion. If just the production of the fibrous capsule is expressed, the material can be considered *bioinert*, but if a surface or bulk transformation occurs, the material is *bioresorbable*. *Bioactivity* is observed when the material plays an active part in new tissue formation. For instance, bioactive glasses show generally not only osteoconduction (i.e. ability of allow bone to grow on material's surface) but also osteoinduction skills (i.e. they promote actively the cell recruiting and thus the formation of new bone). As one can easily see, biostable materials are easily bioinert, and bioresorbable/bioactive materials are necessarily biodegradable.

The interface characteristics are very important, as we mentioned above. Theoretically, any material could increase its biocompatibility by surface modifications, such for example being covered with a porous layer mimicking natural bone's structure, or grafting specific proteins (grow factors) to enhance cell recruiting. The surface status can provide a simple mechanical graft (almost-inert), a strong mechanical hook (in porous materials, with controlled porosity similar to the one of trabecular bone, i.e. pore diameter$\approx$100-300 μm) or a total conversion of the surface and the bulk (bioresorbable). In bioactive materials, the graft is not only mechanical but chemical, i.e. a strong interaction intercurs between the material and the new tissue.

1.1.2 Generalities on bioceramics

It's worth to say that the concept of "bioactive" material is strictly related to the discovery made by prof. L. L. Hench, in the early '70s, that a silica-based glass (the Bioglass 45S5®) showed the ability to promote bone reconstruction. Hench alone or with co-workers [39] described in more than one work the actual mechanism in which a material is resorbed in

biological conditions. The present work's aim is not to understand the bioactivity in bioglasses, but general concepts about bioceramics are related to this kind of materials; further details on this are found in ref. [28]. Hench gave the following definition of "bioactive material" [38]:

> *"A bioactive material is one that elicits a specific biological response at the interface of the material which results in the formation of a bond between the tissues and the material".*

According to many authors, there have been many generations of biomaterials throughout the years:

1. The *first generation* of biomaterials is considered to be set in the '50s and the early '60s, when a material inserted in living tissues was requested only to be *not dangerous*, but it was not bioactive neither bioresorbable, i.e. it was bioinert. Metals and their alloys were the first examples of this generation.

2. In the late '60s the discovering of the Bioglass 45S5® by Hench led to the definition of a *second generation* of biomaterials, having the characterstic of being either *bioactive* or *bioresorbable*. Hydroxyapatite began to be used for biomedical devices too.

3. When in the late '80s composites and nanocomposites of hydroxyapatite with collagen or other resorbable polymers, bone mimicking made this material both bioresorbable and bioactive, and a *third generation* of biomaterials was born.

4. At the end of the '90s the *tissue engineering* took place, i.e. the set of techniques that aims to design living tissues starting from artificial scaffolds, but resorbed and recreated by the organism itself. The material is then only a part of an engineered organ, and a so-called *fourth generation* of biomaterials is still developing.

It's worth to notice that the first biomaterial (Bioglass 45S5®) has been created when the world was looking for a cure for many damaged parts in soldiers involved in war accidents [41]. But after this, biomaterials started to develop exponentially in terms of publications per year, worldwide market, and clinical applications. This is most likely due to the global population aging, i.e. the trend of the population to become older and older throughout

the years, as expressed in figure 1.1.2. The increasing quote of population aged over 60 is not homogeneously distributed allover the world: the division between Europe, Northern America and some Asian country on one side, and the other countries on the other side is sharp. For instance, Japan (followed by Italy) shows the highest percentage of old people (i.e. aged over 60) that is almost 25% nowadays. On the other side, the average of the so called "developing word" aged over 60 population is approximately 5% (data from nec.co.jp). Anyway, this quote of population needs to keep its living conditions constant (at least if they live in the most developed countries) and to do so, the repair of age-damaged tissues appears to be unavoidable. The above introduced evolution in biomaterials science allowed also to look for medical cares for previously untreatable diseases. One of the most interesting applications of bioglasses is, for instance, the *in situ* treatment with radiotherapy of cancers, like the hepatocellular carcinome (HCC) [40].

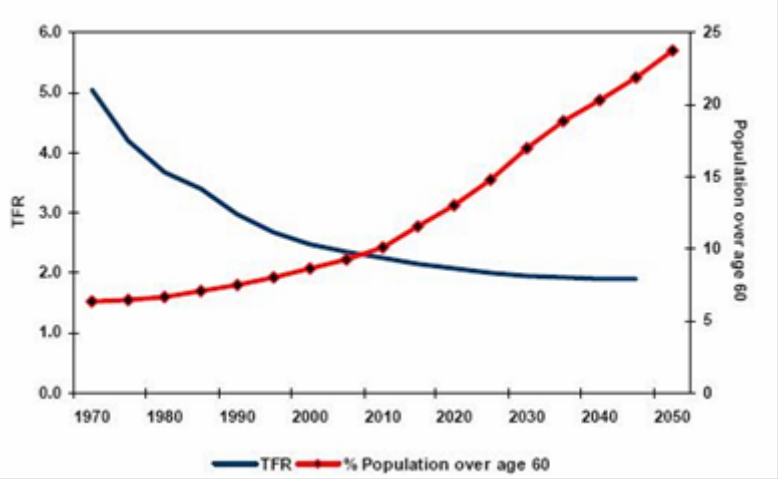

Figure 1.1.2: TFR (total fertility rate) and percentage of population aged over 60 vs time (years), © 2008 CNCA

Calcium phosphates, which are the main subject of this thesis, are *ceramic* biomaterials, *bioresorbable*, and, although the bonding mechanism differs from the one of bioglasses, somehow *bioactive*. In fact, since the definition mentioned above requires the ability of the material to develop a "direct, adherent and strong bonding with bone" [21], bioactivity in calcium phosphates is fully respected. Anyway, they should still be considered osteoconductive but not always oseoinductive. Their position in the huge word of bioceramics is shown in figure 1.1.3.

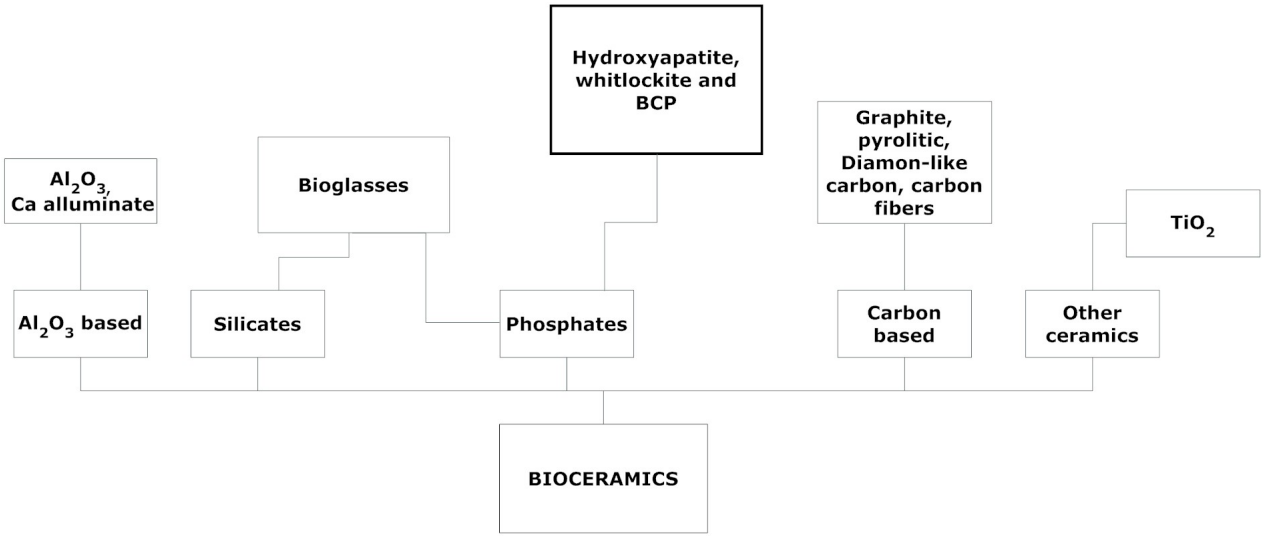

Figure 1.1.3: Resume of ceramic biomaterials

Their use in biomedical devices is known since longtime, and will be shown in the next sections. Further details on biomaterials are available in ref. [77, 2] and particularly on bioceramics in ref. [79].

1.2 Calcium phosphates in human bone

1.2.1 Generalities on human bone

Human bone is a living tissue composed by a mineral part, and an organic part composed of cells, collagen, and non-collagenous proteins as polysaccharides and lipids. Table 1.2.1, taken from ref. [77], resumes the weight percentage of each phase. As one can easily see, the mineral part is prevalent, and the majority of this part is constituted by hydroxyapatite. It's then obvious that this Calcium phosphate has been soon developed as biomaterial for bone replacement.

In human bone, the extracellular matrix is mineralized, differently from other tissues. This feature gives the bone the characteristic to be an "hard tissue". Living cells are hosted inside the matrix and they can be classified into

- **pre-osteoblasts** and **osteoblasts**, responsible of the production of the organic part of the matrix and regulating the deposition of the mineral part.

Inorganic phase (wt %)	**Organic phase (wt %)**
Hydroxyapatite ∼60	Collagen ∼20
Carbonate ∼4	Water ∼9
Citrate ∼0.9	Non-collagenous proteins (osteocalcin, osteonectin, osteopontin, thrompospondin, morphogenetic proteins, sialoprotein, serum proteins) ∼3
Na and Mg ∼1.3	Traces of polysaccharides, lipids and cythokines
Traces of Cl, F, K, Sr, Pb, Zn, Cu, Fe	Primary bone cells: osteoblasts, osteocytes, osteoclasts

Table 1.2.1: Bone composition, adapted from ref. [77]

- **osteocytes**, "sleeping cells" that are trapped in the inner part of the bone, and that can be transformed again in osteoblasts when a new formation of matrix is needed
- **osteoclasts**, which are giant polymorphonuclear cells, able to dissolve the mineral part of the bone

Many types of bone are found in human livings: long, short, flat, irregular, sesamoid. The morphology itself can be either *woven* if collagen fibers are randomly organized, or *lamellar* when collagen fibers are parallel aligned, which gives the structure a better performance in terms of mechanical strength. Almost every bone has got an outer *compact* or *dense* part, and an inner *trabecular* or *spongeous* part, in which tiny branches of bone (trabeculae) are disposed in the 3D space to response the mechanical stress. The outer and inner side of each long bone is commonly covered with soft connective tissue, named *endosteum* and *periosteum*, respectively. Figure 1.2.1, taken from the SEER training modules of the U.S. national cancer institute, shows the morphology of a long bone.

From the materials science point of view, the bone is a *composite* material, at many levels: first of all, it is composed by an *organic* and *inorganic* part. Inorganic matrix, hard but brittle, results to be reinforced by the collagen fibers, as happens in some artificial materials. After this, its tridimensional structure is made of canals with hollows; this structure gives the bone good mechanical properties with low density at the same time.

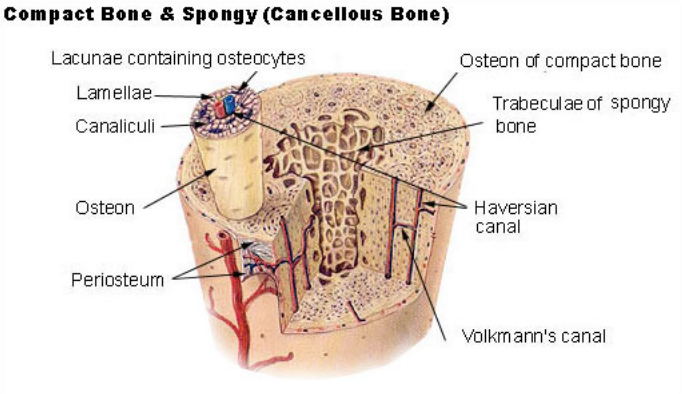

Figure 1.2.1: Morphology of human bone, taken from the U.S. national Cancer Institute, SEER training modules, http://training.seer.cancer.gov

1.2.2 Teeth

Teeth are not only made of bone, but of many tissues, each one with a specific role. One must remember that the first aim of the tooth is to break down food. That is, from a materials science point of view, it is requested to have high hardness, high UTSL (Ultimate Tensile Strength Limit) and high wear resistance at the same time. Figure 1.2.2 helps to understand the following description.

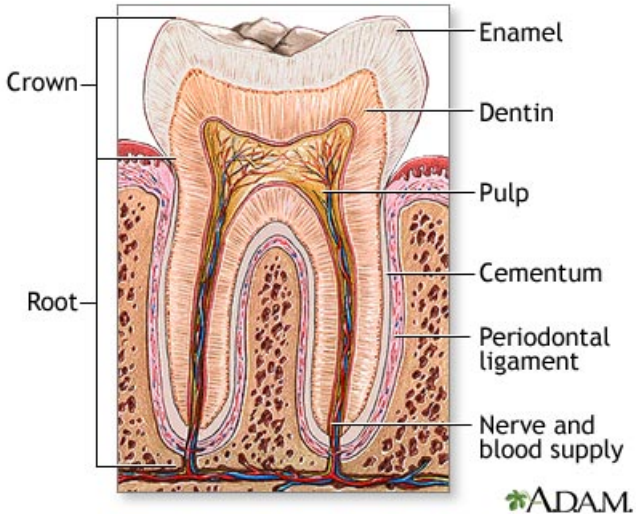

Figure 1.2.2: The tooth structure, from A.D.A.M.^{TM} website, www.lifespan.org

Basically, two parts of the tooth are recognizable: the outer part, the *crown*, is sup-

posed to mechanically break down the food, thus it needs to be hard enough. The material covering this part is the *enamel*, and in fact it the is hardest and most highly mineralized substance in the human body. Its forming cells, the ameoblasts, disappear soon after the enamel formation, and thus the tissue remains cell-less in its mature life. It is composed mainly by well crystallized hydroxyapatite, with only 3-4% wt. content of organic part. Its hardness is ranked 5 in Mohs hardness scale.

Below the enamel stands the *dentin*, which is still constituted by hydroxyapatite in 70% wt., but it's less hard, it's vascularized, and its role is not only to support the enamel, but also to connect with a complex tubular system the pulp of the tooth to the crown. Tooth *cementum* covers the dentin all around. Its hydroxyapatite content is only about 50%, but it has the highest fluoride content of all mineralized tissue. The inner part of the tooth, directly connected to blood vessels and nerves, is the pulp, entirely made by connective tissue and hosting the tooth living cells, called odontoblasts.

1.2.3 Bone resorption

The process of bone formation is quite complex and it is fully described elsewhere [2]. We just want to give the reader a general knowledge about the main mechanisms involved in this process, in order to understand the aim of the present work. Some important steps are required for a complete bone resorption.

The bone matrix production, as already told, is leaded by osteoblasts. Their morphology has been developed to secrete many proteins useful for the cell recruiting, such as α and β TGF (transforming growth factor), BMPs (Bone morphogenetic proteins), and IGF (insulin-like growth factor). All of these provide the proliferation of osteoblasts, and/or increase their metabolic activity. After the bone formation, osteoblasts remain in an inactive state. When bone remodeling is required, osteoclasts play a very crucial role. In fact, they break up the mineralized matrix to allow osteoblasts to reform new bone. Osteoclasts are actually great cells which secrete specific enzymes and attack the bone in a specific site called "Howship lacuna". It's very important to say that bone dissolution begins with a local variation of pH: osteoclasts are in fact able to decrease the pH value with a process named "carbonic anhydrase", in which CO_2 and water reaction produces carbonic acid. The protons coming from this and other acids present in the cell (citric, lactic...) are transferred by the membrane out of the cell. Because hydroxyapatite, as we will see, is

not stable in acidic condition, this results in a dissolution of the mineralized part of the matrix. Before moving to other lacunae, the osteoclasts release specific signals to recruit osteoblasts that are able to form new tissue.

1.2.4 Calcium Phosphates

Table 1.2.2, adapted from a work of S.V. Dorozhkin [21], which is a full and exhaustive publication on calcium orthophosphate as bioceramics, shows the most common Calcium phosphates. Phosphates are salts produced by phosphoric acid, H_3PO_4. The prefix *ortho-* is used to distinguish the phosphoric acid (and phosphate ion) from the *poly*-phosphoric one, which is made by chains of more than one phosphoric acid molecule. For instance, pyrophosphoric acid is obtained by reaction $2H_3PO_4 \rightarrow H_4P_2O_7 + H_2O$, i.e. by the condensation of two phosphoric acid molecules. Tripolyphosphoric and tetrapolyphosphoric acid are obtained by similar reactions out of three or four molecules, respectively. Equilibrium constants of phosphoric acid are given by the following reactions [28]:

$$H_3PO_4 + H_2O \rightleftharpoons H_2PO_4^- + H_3O^+ \quad pK_1 = 2.12$$

$$H_2PO_4^- + H_2O \rightleftharpoons HPO_4^{2-} + H_3O^+ \quad pK_2 = 7.21$$

$$HPO_4^{2-} + H_2O \rightleftharpoons PO_4^{3-} + H_3O^+ \quad pK_3 = 12.00$$

The majority of calcium orthophosphates used in biomedical applications are constituted by hydroxyapatite (HA), tricalcium phosphate in β form (sometimes named "whitlockite" when in Ca,Mg-TCP form, or simplyβ-TCP), or in α form. Bioceramics constituted by an intimate mixture of hydroxyapatite and TCP in α or β form are commonly named bi-calcium phosphate (BCP). Their solubility product in neutral pH is reported in table 1.2.2. TCP is not stable in aqueous environment, and it is rapidly converted in hydroxyapatite in the organism with a water absorption close to 8% wt.

The TCP to HA transition is provided in water by the following reaction:

$$2H_2O + 4Ca_2(PO_4)_2 \rightarrow Ca_{10}(PO_4)_6(OH)_2 + 2Ca^{2+} + 2HPO_4^{2-} \tag{1.1}$$

Ca/P molar ratio	Formula	Compound	Solubility at 25°C [-log(K_S)]	Solubility at 25°C [g/L)]	pH stability range
0.5	$Ca(H_2PO_4)_2 \cdot yH_2O$	Monocalcium Phosphate monohydrate (y=1) or anhydrous (y=0, only at T>100°C)	1.14	$\sim 17-18$	0-2
1.0	$Ca(HPO_4) \cdot nH_2O$	Dicalcium Phosphate dihydrate (n=2, Brushite) or anhydrous (n=0, Monetite)	6.59/6.90	∼0.088/0.048	2-6/-
1.33	$Ca_8(HPO_4)_2(PO_4)_4 \cdot 5H_2O$	Octacalcium Phosphate	96.6	∼0.0081	5.5-7.0
1.5	$\alpha - Ca_3(PO_4)_2$, $\beta - Ca_3(PO_4)_2$	α-Tricalcium Phosphate, β-Tricalcium Phosphate	25.5/28.9	∼0.0025/0.0005	-
1.2-2.2	$Ca_xH_y(PO_4)_z \cdot nH_2O$ $n = 3 - 4.5$	Amorphous Calcium Phosphate	-	-	∼5-12
1.5-1.67	$Ca_{10-x}(HPO_4)_x(PO_4)_{6-x}(OH)_{2-x}$ $(0 < x < 1)$	Calcium-deficient Hydroxyapatite	∼85.1	∼0.0094	6.5-9.5
1.67	$Ca_{10}(PO_4)_6(X)_2$ $(X = OH, F)$	Hydroxyapatite, Fluorapatite	116.8/120.0	∼0.0003/0.0002	9.5-12/7-12
2.0	$Ca_4(PO_4)_2O$	Tetracalcium Phosphate, hilgenstockite	38-44	∼0.0007	-

Table 1.2.2: Calcium phosphates classification after S.Dorozhkin [21]

This conversion could destroy the phosphate lattice, but a coating of insoluble HA usually protects the bulk material from this event. As one can see, reaction 1.1 can take place in basic pH conditions, and results to be accelerated by the presence of fluoride anion (see chapter 11).

The production of BCP by tuning the HA and TCP contents allows the designer to control the final product's properties, as shown for instance in figure 1.2.3, which shows the linear shrinkage of pre-calcination powders converted into HA, TCP and 50%-50% BCP.

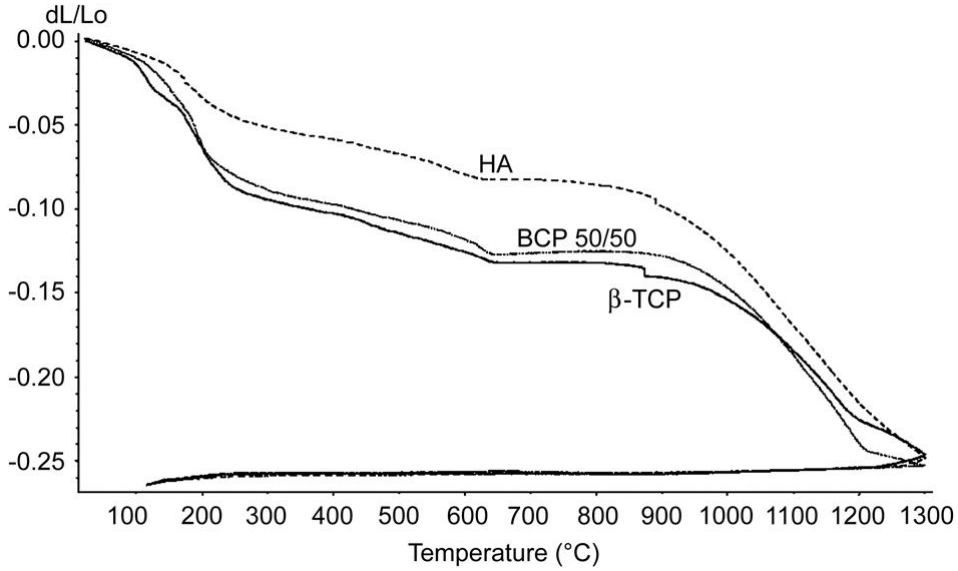

Figure 1.2.3: Ca phosphates mechanical properties: linear shrinkage of amorphous calcium phosphate transformed in TCP, HA or BCP, taken from ref. [27]

1.3 Hydroxyapatite: structure and properties

Apatites are calcium phosphates with general formula $M_{10}(PO_4)_6X_2$, sometimes expressed as $M_5(PO_4)_3X$. In the present work, the first formula will be used as it is is the direct expression of the atoms contained in the unit cell.

The X^- anion can be either an hydroxyl group, i.e. OH^-, or an halogen ion, most of all Cl^- or F^-. In this case, apatites are named hydroxyapatite (often hydroxylapatite), chlorapatite (sometimes chloroapatite) and fluorapatite (or fluoroapatite), respectively, and

in the present work they will be indicated as HA, ClA or FA.

The metal atom, *M*, can be a divalent cation such as an alkaline-earth (Be^{2+}, Mg^{2+}, Ca^{2+}, Sr^{2+} or Ba^{2+}) or non alkaline earth such as Pb^{2+}, Zn^{2+}. A coupled substitution of Na^{+} for Ca^{2+} and CO_3^{2-} for PO_4^{3-} is also possible [94]. If a full substitution of VO_4^{3-} for phosphate group occurs, a *vanadite* compound is obtained; studies on the Silicon substitution for a $Ca_{10}(PO_4)_{6-x}(SiO_4)_x(OH)_{2-x}$ phase formation have also been performed [32].

From the biological point of view, Calcium apatites are the most interesting materials, then from now on the term "apatite" refers to Calcium-based phosphates. When indicating a substituted apatite, the expression M:HA will be often used to refer to the general $Ca_{10-y}M_y(PO_4)_6(OH)_2$ formula in the present work.

Many possible substitutions can occur when apatite is immersed in biological medium. First of all, the carbonate content of biological fluids produces the *carbonation* of hydroxyapatite, that can be either of the A or B type, i.e. the carbonate can substitute the OH^- or the PO_4^{3-} group, respectively. Ion sizes increase in the following order: OH^-< CO_3^{2-}< PO_4^{3-} and thus an increase in the *a* axis is recorded in the first case, and a decrease in the second case. Details on this aspect have been deeply investigated by LeGeros and coworkers [102, 55, 56, 57]. Carbonate substitution and Ca vacancies can result in a variation of the overall Ca/P molar ratio in the product, which is stoichiometrically $\frac{10}{6} = 1.\bar{6}$. Because PO_4^{3-} is stable only at very basic conditions, HPO_4^{2-} and $H_2PO_4^-$ anions can occur in physiologic conditions. Thus, the formation of a hydrogenphosphate-substituted and Ca-deficient apatite is often recorded in literature. Moreover, the physiological equilibrium (in which pH$\backsimeq$7.5) that moves from Brushite or amorphous Ca phosphates and passes through different forms of TCP results finally to favor HA or Ca-deficient HA [79]. One can consider the general formula of biological occurring apatite as:

$$Ca_{10-y}(PO_4)_{6-y}(CO_3)_x(HPO_4)_y(OH)_{2-x}$$

with the *x* value increasing with the age of the organism, and the *y* value decreasing (see ref. [77], after M. Vallet-Regì). The CO_3^{2-} weight percentage in biological carbonated hydroxyapatite (called HCA) ranges usually from 3.2 to 5.8 % wt.

For the above mentioned phenomena, powders with a nominal Ca/P ratio ranging from 1.50 to 1.67 currently form hydroxyapatite when exposed to biological environment.

From the crystallographic point of view, HA structure can be described either as belonging to the monoclinic or to the hexagonal space group. In the present work, the latter group will be considered as it is more useful when considering non-stoichiometric substituted apatite. Lattice parameters of theoretical HA are $a = b = 9.42$, $c = 6.88$ and $\alpha = \beta = 90°$, $\gamma = 120°$. However, these parameters depend not only on non-stoichiometric substitution as described above, but also on synthesis variables such as calcination temperatures. More details on this point are provided in section 5.2.4.

ICSD (Inorganic Crystal Structures Database) references has been used throughout this work to perform Rietveld refinement of apatite phase. Table 1.3.1 shows starting (i.e. unrefined) atomic positions and occupancy factors of each atom in stoichiometric HA[2]. Occupancy factors were user-defined and taken from ref. [7].

Atom	**x (a)**	**y (b)**	**z (c)**	**O.F.**
Ca (1)	$1/3$ =0.3333	$2/3$ =0.6667	0.0007 (8)	$1/3$
Ca (2)	0.2465(4)	0.9933 (5)	$1/4$ =0.250	$1/2$
P	0.3968(7)	0.3693 (8)	$1/4$ =0.250	$1/2$
O (1)	0.331(1)	0.480(1)	$1/4$ =0.250	$1/2$
O (2)	0.579(1)	0.455(1)	$1/4$ =0.250	$1/2$
O (3)	0.3394 (8)	0.2569 (7)	0.0694(8)	1
O (4)	0	0	0.192(3)	$1/6$

Table 1.3.1: ICSD atomic positions and occupancy factors (by user) of stoichiometric HA

When atomic positions are fixed (e.g. 1/3 or 1/2) they have not been refined. Many authors suggest that an F^- for OH^- substitution in apatite lattice results in a decrease of the *a* axis because of the smaller size of the first ion with respect to the latter. Again, the reader should refer to following sections, particularly 5.2.4, and to the $FHA_{1.67}$ samples set characterization for further details (chapter 6). The oxygen atoms of the phosphate are described as O(1), O(2) and O(3), and the one of hydroxyl group is O(4).

Apatites can be considered as regular phosphate tetrahedra around two symmetry-distinct cation sites: a 6-fold Oxygen coordinated 4f site (Ca1) and the 9-fold Oxygen coordinated 6h site (Ca2), with 4f/6h ratio equal to 4/6=2/3. Figure 1.3.1, taken from

[2]More precisely, in its asymmetric unit, see next chapter for details.

Michie et al. [70], represents the primitive unit cell in apatite structure, viewed along the [0001] direction[3].

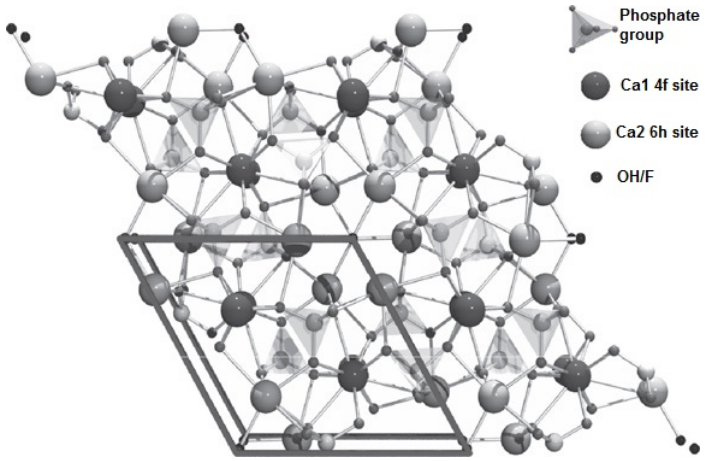

Figure 1.3.1: Apatite crystal structure viewed along [0001]. The parallelogram highlights the hexagonal primitive unit cell. Picture taken from ref. [70]

Figure 1.3.2, obtained by the author with the Fp-Studio ver 1.0 software from Rietveld refinement data, shows the hexagonal cell in details, and it's helpful to understand the following description.

Two different subsets are hence definable; the first subset consists in the Ca1 position with its 6 coordinated phosphates. Two Ca1 sites are positioned at at level z=0 and two at z=0.5. Ca(2) positions describe instead a double triangle, one set to z=0.25 and the other to z=0.75. Phosphates tetrahedra (6 in total) are disposed in helical arrangement from levels z=0.25 to z=0.75. See picture 2 of figure 1.3.2 for details.

As one can see, the OH^- anions or their substituting are placed along the so-called "*c*-channels". These channels seem to have a crucial role in many apatites properties, such as dissolution rate. In fact, dissolution mechanism starts probably from the leaching of the X^- anions located in this axis. This aspect has been widely investigated by S.V. Dorozhkin and by other authors and will be discussed deeply in chapter 10.

Hydroxyapatite synthesis is known since the early times of biomaterials science; Hench reports that Levitt and co-workers synthesized hydroxyapatite from solid mineral fluorapatite in 1969 [39]. Many methods have been used for the synthesis of this material, and

[3]Total number of Ca sites is 10, which means that Z value is 1 in the case that the general $Ca_{10}(PO_4)_6(OH)_2$ formula is used.

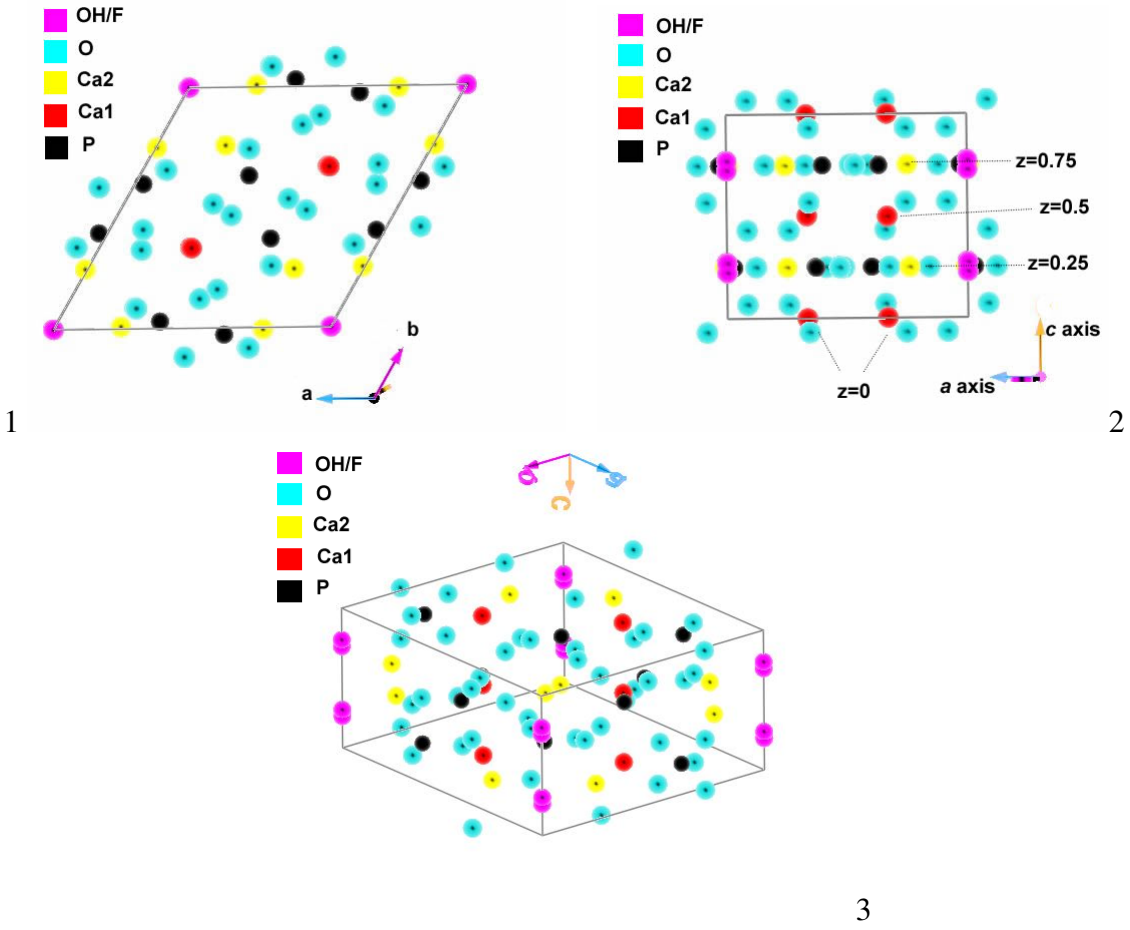

Figure 1.3.2: The apatite primitive unit cell: perpendicularly to *c* axis (1), perpendicularly to *a* axis (2) and bird's eye view (3)

an overview on them is given in chapter 4. Sintering abilities of apatites has been finely studied by many authors [35], but unfortunately the one of hydroxyapatite is generally low when below its transition temperature to pyrophosphate. In fact, sintering procedure is typically performed at 1050-1200°C for 3h, but one can heat up to 1300°C to accelerate the process. At 900°C in dry environment, β-TCP is formed in powders with Ca/P ratio close to 1.50, and decomposes in α-TCP over 1400°. Powders with high P content (i.e. defective apatites) can show α-TCP formation at 1000°C. The presence of both the TCP phase (α or β), together with the Dicalcium phosphate (DCP, Brushite or Monetite mineral) is often considered a contamination when powders need to be sintered. In fact, the TCP allotropic transformation involve a volume change, and the DCP decomposes to Ca pyrophosphate

for T≈600°C.

Polycrystalline hydroxyapatite mechanical properties are strongly dependent on the microstructural parameters. For instance, the "fracture resistance" σ parameter reported by Ravaglioli and Krajewski (ref. [79] after Griffith), depends on grain size (D) according to the equation:

$$\sigma = \sigma_0 + RD^{-1/2} \tag{1.2}$$

where R and σ_0 are material's constants. That's why compressive strength can vary from 500 to 1000 MPa, and Elastic modulus from 80 to 110 GPa. That's quite high, considering that the stiffest biological material is tooth enamel, with 74 GPa. Poisson's ratio is about 0.3, which is very similar to human bone, and fracture toughness about 1 MPa·$m^{0.5}$. Nominal density is 3.16 g/cm^3 (data taken from ref. [77]). It's worth to notice that the main difference between synthesized apatite and biological occurring one stands in the crystallization degree, which is normally very low in biological apatite, but it can reach very high values in synthetic one. Moreover, crystal growth shows often preferred orientation in biological HA, but it's usually uniform in synthetic one.

Synthetic hydroxyapatites find several successful clinical applications, such as oto-laryngic implants, maxillofacial reconstruction, dental or periodontal implants, alveolar ridge augmentation, percutaneous access devices, spinal surgery devices and artificial joints, and as a cover for metals in load-bearing devices [39].

In addition to biomedical applications, pure and substituted hydroxyapatites find interesting employment in catalytic devices, luminescent materials [1], and as ion-exchange chromatography column materials [45]. The tuning of HA properties by addition of several mineral ions is thus an interesting multi-disciplinary subject; anyway, in the present work we'll focus on the biomaterials science aspects.

1.4 Fluorine and Strontium substituted hydroxyapatite

1.4.1 Fluorine role

As introduced before, fluorapatites are very well known minerals among the wide apatites family. The investigation of the whole range of F for OH substitution from pure hydroxya-

patite to pure fluorapatite has been investigated widely by Rodriguez-Lorenzo, Gross and co-workers in more than one work [83, 85, 84, 33, 34, 35, 37]. Historically, this material has been deeply studied from the oral biology and oral healthcare point of view [64], because of its great use in dental applications. Fluoride content in teeth depends strongly on the age of the patient, the environmental conditions, diet and area of the tooth. The tooth root, (cementum and dentine) fluoride content is normally higher than the crown (enamel) one [49]. There's been a huge discussion about drinking water fluoridation (i.e. fluoride addition) as method to prevent tooth decay; on one hand, fluorine is known to aid enamel remineralization, but on the other hand *dental fluorosis* disease can occur. This disease consists in an excessive uptake of fluoride by dental enamel in the first years of childhood. Teeth grow up with an overdose of fluorapatite in the first stages of their life, and this results in white spots or sometimes pitting. Fluoride uptake is not dangerous when teeth are already in their mature stage, because a fluorapatite layer contributes to give the enamel better mechanical properties. For this reasons, F^- content in drinking water has been regulated by more than one association (WHO, American dental association...). It's useless to stress that many oral hygiene products available in commerce (toothpastes, mouthwashes...) reclaim to contain high levels of fluorine.

The mechanism of bone remineralization and caries-induced lesions reducing through fluoride treatments have been investigated since longtime [100], but fluoridated hydroxyapatite found recently interesting applications also in resorbable bone scaffolds, [6, 37]. Bellows and co-workers [4] found that mineralization of osteoid nodules (i.e. the organic portion of the bone matrix that forms prior to the maturation of bone tissue) follows a two-steps process: an initiation phase, depending on alkaline phosphatase bone forming cell activity, and a progression phase that proceeds independently of alkaline phosphatase activity. Alkaline phosphatase is an enzyme responsible of phosphate groups removal from molecules, thus its activity is directly related to the bone formation, and it's known to be stimulated by low contents of fluoride [73]. In resuming, one can say that the biological role of fluoride is to stimulate the differentiation of stem cells in bone-forming cells, and this results in higher mineralization rates [37]. For this reason, F-substituted hydroxyapatite scaffolds attract the attention of the biomaterials designers community. Moreover, fluoride play also a structural role: the substitution of hydroxil groups of hydroxyapatite to form fluorapatite enhances some interesting properties, such as mineral stability but also leads to enhanced crystal growth [4, 22]. The microstructural changes in HA lattices when

F^- is added in the product will be actually object of discussion in the present work.

Concerning other applications, it's worth to notice that fluorapatite greater stability with respect to hydroxyapatite in biological environments can have interesting consequences on the realization of drug-delivery systems, especially if coupled with more soluble products such as TCP. To do this, one must tailor the exact F^- amount in the hydroxyapatite lattice to understand the mechanical and physico-chemical properties of the product, avoiding also to incur in fluorosis which can also lead to worse diseases such as osteoclorosis (abnormally elevation in bone density).

1.4.2 Strontium role

Strontium is to be considered a trace element in human bone, i.e. its amount is generally not higher than 0.054 wt. % [43], but the real value depends on the patient age, diet, and the kind of bone analyzed[4]. Since the early stages of biomaterial science, Sr behavior has been studied because of its chemical affinity to Ca, and for osteoporosis prevention applications. Indeed, some Sr-containing products are currently available in commerce to enhance bone formation, often in form of capsules and reclaiming to have "bone making" skills.

Concerning the biological role of Sr on bone remodeling, P. Marie alone [61] or with co-workers [62] found that:

- Sr promotes pre-osteoblasts cells proliferation and differentiation in osteoblasts, causing a enhanced bone forming activity.
- Sr inhibits a osteoclasts proliferation and activity, decreasing the bone resorption.

For these reasons, Sr is used as anti-osteoporotic agent: in fact bone dissolution by osteoclasts is reduced while bone deposition is increased. The uptake of Sr in human bone can occur from many sources, the most important of which is the Strontium ranelate salt, which chemical formula and structure are visible in figure 1.4.1. Sr ranelate is currently a drug treatment for post-menopausal osteoporosis in several countries [68].

However, Sr^{2+} ion can also be directly inserted inserted in the apatite lattice because of its great similarity to Ca^{2+}. Christoffsen and co-workers prepared Sr-doped samples of hydroxyapatite which resulted to obtain an increase of the bone mineral content (BMC) and

[4]When considering the Sr/Ca ratio, this value becomes 0.1–0.3 wt. ‰

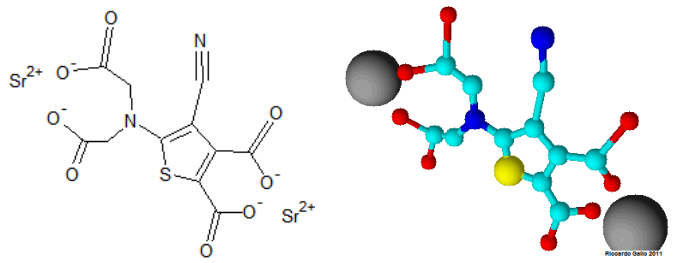

Figure 1.4.1: Strontium ranelate chemical structure

bone mineral density (BMD) of a factor of about 10 when the 10% atomic Sr for Ca substitution was achieved [13]. Renaudin and co-workers [80] confirmed the anti-osteoporotic properties and assessed also some anti-inflammatory skills; in fact, the production of tumor necrosis factor-α (TNF-α) by human monocytes cultured *in vitro* with lipopolysaccharide was found to be decreased when cells are in contact with Sr-doped HA. It seems that the quantity of Sr substitution to obtain an improvement of the osteosynthesis is generally low. A more detailed work on the effect of Sr added to biphasic Ca phosphates (BCP) either in the synthesis step or in the culture medium (as $SrCl_2$) is reported by Braux and co-workers [9], who confirmed the previous considerations; in fact, the expression of MMP-1 and MMP-2 genes (related to cell morphology and matrix metalloproteinases expression) have been monitored, together with the expression of type I collagen. When Sr is present in the BCP particles, it resulted in a neat decrease of the two MMPs production and an increase of the type I collagen expression. Laquerriere and co-workers report that Sr has a positive role in improving the cell adhesion to the implant but it reduces the osteoblasts growth and increases LDH activity (lactate dehydrogenase enzyme, related to tissue breakdown and thus to hemolysis).

On the crystallographic consequences of inserting Sr atoms in the HA lattice, some important studies have been published in the already cited Renaudin work and also by Bigi and co-workers [7]. The first work reports a stabilization of a β-TCP phase in the Sr-doped samples, while the latter does not, most likely because no heat treatment has been performed. It seems that he stabilization of the more soluble TCP phase could be tuned by the Sr addition to obtain BCP products. An increasing in both *a* and *c* axis has been reported when the bigger Sr ion is hosted in a Ca site, with a slight preference for the latter. According to Hill and co-workers, Sr-substitution improves radio-opacity in calcium fluoro-alumino-silicate glasses used for bone replacement and as cements for dental appli-

cations, and enhances also the surface nucleation and precipitation of fluoroapatite in the glass matrix, to obtain some interesting bioglass-ceramic materials [42].

Chapter 2

Characterization techniques: fundamentals

2.1 X-ray powder diffraction and Rietveld refinement

In the present section, the basics of Rietveld refinement on XRD patterns recorded on powdered samples will be illustrated, in order to give the reader a general overview for a better comprehension of the next results. X-ray diffraction is probably the most important technique to characterize crystalline solids, and Rietveld refinement is a useful and very well-known instrument to achieve some important parameters from the XRD patterns. Because of the difficulty to resume all the literature concerning XRD characterization in just the present section, the reader is addressed to more specific works for a full review of the subject, such as ref. [31].

Crystal lattices can be represented as a repeated arrangements of atoms: more precisely, atoms are disposed in primitive unit cells the repetition of which fullfills the tridimensional space. Basing on energetic and geometrical considerations, all the possible primitive unit cells are the ones suggested by Bravais in 1845, and represented in figure 2.1.1. The 14 Bravais lattices representation comes out from the definition of 7 elementary repeating unit cell (cubic, tetragonal, monoclinic, orthorhombic, rhombic, triclinic, and hexagonal) and 4 types of each unit cell (primitive, body centered, face centered, and side centered).

Additional symmetry is then present in the unit cell: every unit cell can be considered as the building block of the crystal because it's repeated in the 3D space. But this building

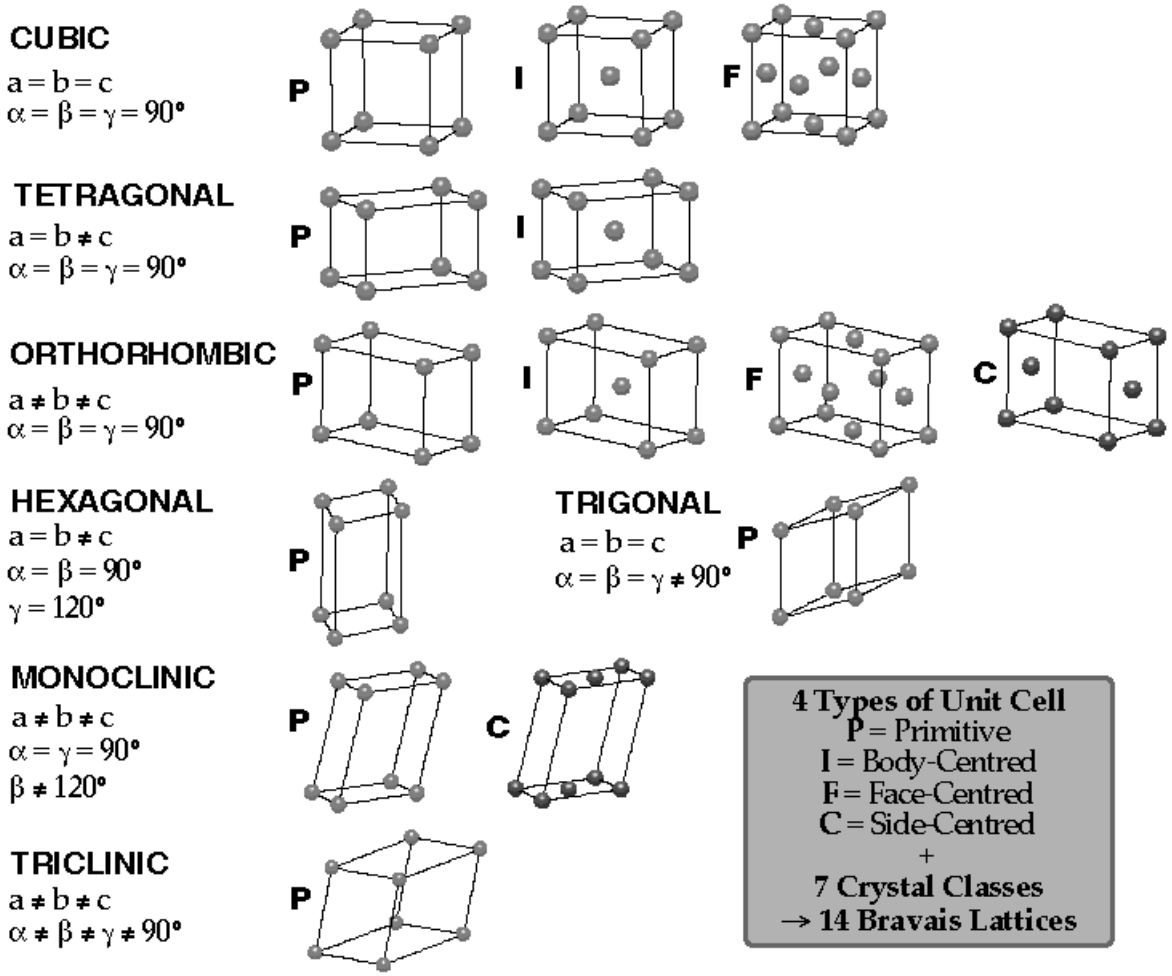

Figure 2.1.1: The 14 Bravais lattices, picture taken from the webpage of Dr S.J. Heyes, University of Oxford, dept. of Chemistry

block is in its turn composed by the symmetrical repetition of a sub-unit, called "asymmetric unit". In fact, in the crystals the following symmetry elements are present: lattice translations, mirror planes, rotation axes, screw axis and glide planes. It's worth to notice that not all the combinations of symmetry elements and lattice types are compatible, but only 230 of them can occur. These correspond to the 230 space group, which are collected in the International Tables for Crystallography, fully available on-line. The most common crystallographic way to indicate a space group is the Hermann-Mauguin notation, in which the first letter represents the type of unit cell (primitive, body-centered...) and the following numbers represent the symmetry operations available along the major axes of the crystal.

For instance, the space group of hydroxyapatite is $P6_3/m$ which means that the cell type is primitive, with 6_3 screw axis[1] and a mirror plane perpendicular to the screw axis (denoted by the slash / followed by *m*).

2.1.1 Bragg's law

William Lawrence Bragg's interpretation of X-ray diffraction in condensed in his famous law:

$$n\lambda = 2d \times sin(\theta) \tag{2.1}$$

Equation 2.1 comes out from the description of crystals as stacks of reflecting planes separated by a distance *d*. Diffraction occurs when the wavelength of the X-ray and its incident angle θ satisfy the Bragg's law, as represented in the schematic illustration of figure 2.1.2.

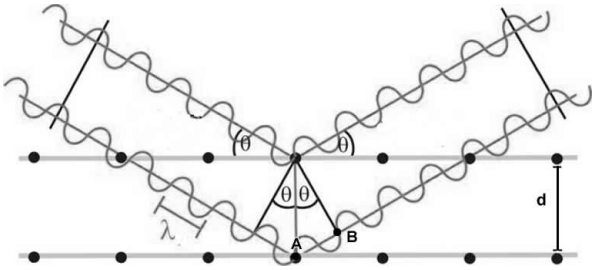

Figure 2.1.2: Schematic illustration of diffraction according to Bragg's interpretation

The X-ray is represented by a plane wave with wavelength λ. To have diffraction, constructive interference must occur between the two reflected rays (i.e. the right side of the drawing); to observe this, the path difference between the first and the second wave after being reflected by one atom must be at least twice the A-B distance in the figure, i.e. twice the $d \times sin(\theta)$ value, or an integer multiple of it (*n* in the formula). The family of planes satisfying Bragg's law for a specific number *n* is denoted as (*nh, nk, nl*) where *h, k* and *l* are Miller's indices.

A rigorous description of this phenomenon should use the concept of *reciprocal lattice* instead of the real one, i.e. a mathematical object in which each reciprocal axis is

[1] This corresponds to a 60° rotation, because 360°/6=60°, with a degree of translation equal to 3, i.e. a translation of 3/6=1/2 of the lattice vector.

perpendicular to two real space axes. This can be resumed by the following expression:

$$\mathbf{i}^* \cdot \mathbf{j} = \begin{cases} 1 & \textbf{if } i = j \\ 0 & \textbf{if } i \neq j \end{cases}$$

The intensity I_{hkl} of the diffracted beam depends on a *structure factor*, named F_{hkl}, which depends in turn on the *scattering* or *atomic form factor,* f_i of each atom and on the average displacement of each atom from its ideal site, U_i, according to eq. 2.2

$$\sqrt{I_{hkl}} \propto |F_{hkl}| \propto \sum_i f_i e^{[2\pi i(hx_i+ky_i+lz_i)]} e^{\frac{-U_i Q^2}{2}} \tag{2.2}$$

The f_i value is particularly important because it states the specific response of each atom to an incident X-ray beam. It depends on the electronic structure of the atom, and on the *momentum transfer* $\boldsymbol{Q}$ value[2]. Its variation against the atomic number Z is shown in figure 2.1.3. The reader should notice from this figure that Fluorine and Oxygen form factors are very similar, and this is consistent with what we'll state later (see section 5.2). For the diffraction of neutrons, the corresponding form factor is much less dependent on the Z number, but still depends on $\boldsymbol{Q}$.

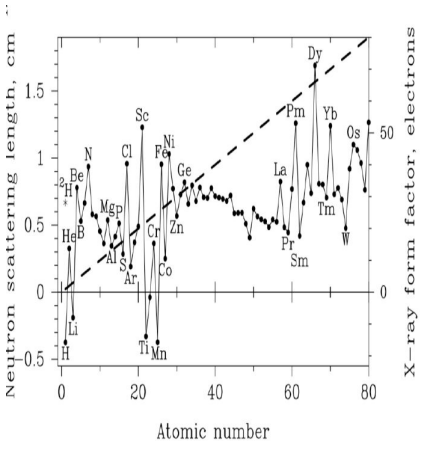

Figure 2.1.3: Form factor f_i dependence on atomic number Z

[2]where $Q = \frac{4\pi sin(\theta)}{\lambda}$

2.1.2 The Debye-Scherrer method

Formerly, Bragg's law has been developed for single-crystal structures, but an adjustment of this theory for powdered samples has been soon developed. The Debye-Scherrer method allowed to collect X-ray diffraction patterns moving from powders by means of an instrument originally made up as sketched in figure 2.1.4, taken from the webpage of the *Museum optischer Instrumente* by Dr. Timo Mappes, (Germany).

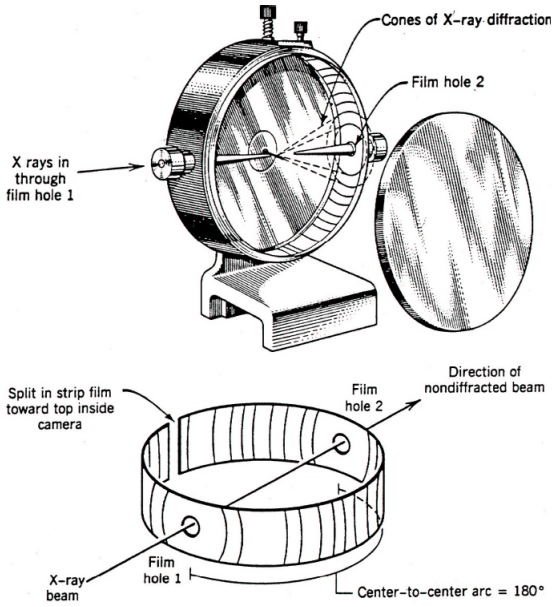

Figure 2.1.4: Debye-Scherrer camera sketch, taken from the webpage of *Museum optischer Instrumente* by Dr. Timo Mappes

The powdered sample is supposed to contain grains oriented randomly in all the possible directions. The incident beam will meet a representative number of crystallites having the right orientation for diffraction, i.e. some of the plane families will satisfy the Bragg's law at a given glancing angle θ, and their reflection will fall on rings with defined 2θ angles. Nowadays the strip film showed in figure 2.1.4 is replaced by a complex system of lenses driving the reflection to a photon detector; if the sample is tilted by an angle θ while the detector rotates around at twice this angle, a "Bragg-Brentano" configuration is obtained. If the sample is stationary and both the X-ray source and the detector are rotated around it, forming a 2θ angle between them, the geometry is called "$\theta - \theta$" .

The diffractogram or XRD pattern is actually a peak diagram reporting the intensity of

diffracted beam, i.e. the numbers of photons (per second) detected at each step against the 2θ value corresponding to that step.

What is worth to say is that this experimental set-up is powerful for multiphase samples analysis , and the broadening of the peaks can provide useful information on the microstructure (e.g. the grain size).

2.1.3 Rietveld refinement

In 1969 Hugo M. Rietveld published a famous article suggesting a method to refine crystal X-ray or neutron diffraction data [81]. In this method, a mathematical modeling of an experimental observed pattern was established. He suggested a least-square approach to refine a theoretical line profile in order to match a recorded profile. The aim of the refinement was indeed to change and adjust many computational parameters to fit the experimental pattern with the calculated one. These parameters can be split into two main categories: computational or *model-depending* parameters and *experiment-depending* parameters [65]. We will focus on the most important experiment-depending parameters, which are the background contribution, the peak broadening and the lattice constants. These are otherwise hard to calculate through the traditional XRD patterns analysis methods.

The original work by Rietveld has been written for neutron diffraction patterns showing gaussian-shaped peaks[3]. The contribution for each *i* step to the reflection can be written as a profile y_i given by the formula:

$$y_i = I_k exp\left[\frac{-4ln(2)}{H_k^2}(2\theta_i - 2\theta_k)^2\right] \tag{2.3}$$

where H_k is the FWHM (full width at half maximum) of the peak, $2\theta_k$ is the center of the reflection (i.e. the calculated position of the Bragg peak corrected for the zero-shift of the counter), I_k is the intensity of the reflection, and $2\theta_i$ is the position of the theoretical profile.

FWHM is provided by a θ_k-dependent formula (known as Caglioti-Paoletti-Ricci formula):

$$H_k^2 = Utan^2(\theta_k) + Vtan(\theta_k) + W \tag{2.4}$$

[3]i.e. $f(x) = a \times e^{-\frac{(x-b)^2}{2c^2}}$

where $U,\ V,\ W$ are refinement parameters for the FWHM. The pre-exponential I_k expression takes into account the step-width of the counter (t), the sum of nuclear and magnetic contribution to reflection (S_k^2, which is strictly related to the structure factor F_k), the multiplicity of reflection (j_k), the Lorentz factor (L_k), and the already mentioned center of reflection and FWHM:

$$I_k = tS_k^2 j_k L_k \frac{2\sqrt{ln(2)}}{H_k\sqrt{\pi}} \tag{2.5}$$

Preferred-orientation effects on the intensity can be considered with an exponential correction that takes into account a "preferred orientation parameter", G and the angle between the scattering vector and the normal to crystallites: $I_{corr} = I_{obs}exp(-G\alpha^2)$.

If one resumes the 2.3 equation in $y_i = I_k exp(-b_k(2\theta_i - 2\theta_k)^2)$, the following empirical correction can improve the fitting of asymmetric profiles:

$$y_i = I_k exp(-b_k(2\theta_i - 2\theta_k)^2) \times (1 - P(2\theta_i - 2\theta_k)^2 \cdot s/tan(\theta_k)) \tag{2.6}$$

The background-corrected profile is given by $y_i = Y_i - B_i$, where Y_i is the recorded intensity and B_i the background contribution.

The peak is supposed not to extend futher than one and a half time its FWHM on both sides of its central position, and in the case of overlap, a simple summation of the contributes to the Bragg reflection of each peak is calculated (see below). Some constraints are obviously considered to help the fitting procedure: atoms are forced to stand still in their positions (with some tolerances) and to be linked each other in a rigid-body structure.

The Rietveld function can be written as:

$$M = \sum_i w_i \left(y_i^{obs} - \frac{1}{c} y_i^{calc} \right)^2 \tag{2.7}$$

i.e. a square difference between the observed profile and the weighted calculated profile. When an overlapping of reflection is recorded, the sum S_i should be considered instead of y_i. The c value represents the $scale\ factor$; in fact, the relationship between the observed and calculated patterns is represented by the formula: $y^{calc} = c \cdot y^{obs}$.

The most important point in Rietveld refinement is determining of the statistical weights

w_i. They can be calculated with the following formula:

$$w_i = \frac{1}{\sigma^2(Y_i) - \sigma^2(B_i)} \tag{2.8}$$

where σ represents the standard deviation (thus, σ^2 is the statistical variance). Because the background variance is otherwise unknown, the second term of the denominator is arbitrarily set to 0.

One can write the 2.6 equation when peak overlapping is observed as follows:

$$y_i = \sum_k w_{i,k} S_k^2 \tag{2.9}$$

and from this equation one can easily define the $w_{i,k}$ expression by comparison with the same eq. 2.6:

$$w_{i,k} = t \cdot j_k \cdot L_k \frac{2\sqrt{ln(2)}}{H_k\sqrt{\pi}} exp(-b_k(2\theta_i - 2\theta_k)^2) \cdot \frac{1 - P(2\theta_i - 2\theta_k)^2 \cdot s}{tan(\theta_k)} \tag{2.10}$$

and this represents the contribution of the Bragg peak at position $2\theta_k$ to the diffraction profile y_i at position $2\theta_i$. The $w_{i,k}$ depends on several parameters, which can be divided into to groups that contribute to define the positions, the FWHMs, the possible asymmetry of the diffraction peaks:

- The first group contains the powder-dependent parameters (preferred orientation):
  - U, V, $W$are the above mentioned FWHM parameters
  - Z is the zero-shift parameter
  - A, B, C, D, E, F are cell parameters according to the reciprocal lattice theory: $1/d^2 = Ah^2 + Bk^2 + Cl^2 + Dkl + Ehl + Fhk$
  - P is the asymmetry parameter
  - G is the preferred orientation parameter
- The second group contains the asymmetric unit cell parameters:
  - c is the overall scale factor

- B_i is the *atomic* isotropic temperature parameter, given by the Debye-Waller isotropic factor[4]
- $x_i,\ y_i,\ z_i$ are the fractional coordinates of the i atom in the unit cell, from now on called the "atomic positions"
- Q is the *overall* isotropic temperature parameter
- n_i is the occupation number, in the present work called "occupancy factor" or O.F.
- $\mathbf{K_{i,j}}$ are components of the magnetic vector of the i atom in the j direction, and are not considered here.

The aim of the technique is to implement the above stated equations in a computer program and to tune (i.e. to *refine*) the above parameters to make the calculated profile fit the observed one. The least-square approach is then employed to minimize the 2.7 equation. Rietveld used the R_p factor to determine the goodness of the fitting:

$$R_{profile} = \frac{\sum |y^2_{i,\ obs} - \frac{1}{c} y^2_{i,\ calc}|}{\sum y^2_{i,\ obs}} \tag{2.11}$$

For a discussion about the agreement of the fitting parameters used in this work, see section 5.2.

It's worth to notice that the fitting procedure allows to refine and thus to know with good approximation some parameters that would be quite hard to achieve with the traditional XRD analyses techniques, such as the lattice parameters or the occupancy factors of every atomic position. On the other hand, the software must start the fitting from a model in which the crystallographic data of the phase are inserted, i.e. a preliminary phase recognition of the powdered sample must be performed.

Figure 2.1.5 shows the fitting of one reflection peak obtained with the FullProf.2k software as described later, and the fitting of a short-range pattern profile, in which the position of every Bragg peak is labelled.

[4]The Debye-Waller factor is calculated by the equation: $DWF = (exp(i\mathbf{q} \cdot \mathbf{u}))^2$, where $\mathbf{u}$ is the center displacement in a scattering movement and $\mathbf{q}$ is the scattering vector. It enters in the definition of the structure factor F_k (not given) and thus on the profile equation.

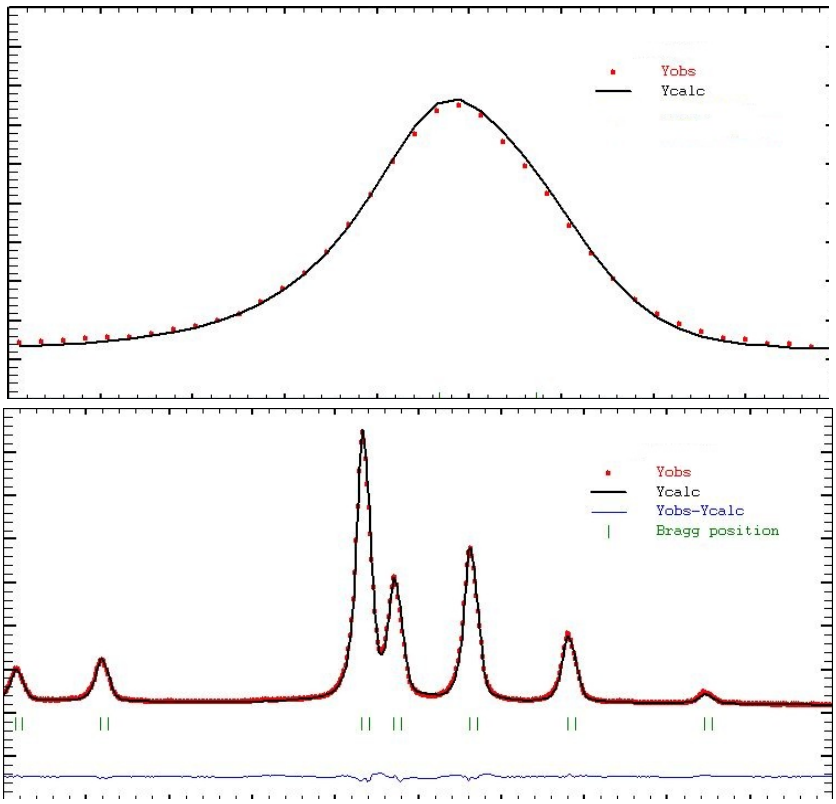

Figure 2.1.5: Fitting of a reflection peak (up) and of a pattern profile (down) with the Rietveld's formula

2.2 High performance liquid ion-exchange chromatography

Ion-exchange chromatography, also called ion chromatography, is a powerful instrument to assess the ion content in a medium. This medium is called "mobile phase" and can be either in gas or liquid phase. It's coupled to a "stationary phase", which can be either liquid or solid. The ion chromatography techniques are classified according to these two phases status; when mobile phase is gaseous and stationary phase is liquid, one can have a "gas/liquid chromatography" abbreviated in GLC. In the same way, we can perform GSC, LLC or LSC. The detection of the ion concentration can be either direct (conductivity measurement) or indirect (chemical suppression of ions).

In the present work, Liquid-solid-chromatography (LSC) with direct conductivity measure is used. It is also called "high performance" chromatography because of the possibility

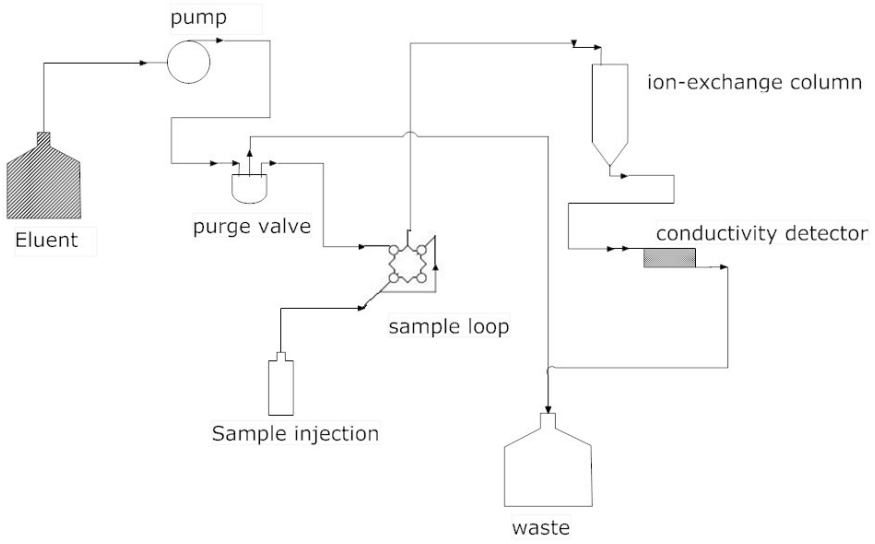

Figure 2.2.1: The HPLC schematic procedure

to discern very weak amounts of ions and separate several chemical species.

In HPLC, the column material (made of porous-glass silica, polystyrene resins or cellulose gels) is grafted by ion-exchanging groups. These groups are balanced by counter-ions and can be *positive* for anionic column, e.g. $-N(CH)_3^+$, or *negative* for cation exchanges, such as $-SO_3^-$.

In stationary conditions, a liquid phase which has the role of transporting the injected sample (the *eluent*) is pumped through the circuit as shown in figure 2.2.1. Sample loop is in "off" position, i.e. the eluent is not mixed with the sample and it can reach the column and afterwards the detector. This latter records the conductivity of the mere eluent, which acts as baseline.

When sample loop is turned in "on" position, the liquid sample is injected and mixed with the eluent, and the following ion-exchange reaction occurs on the column material's surface:

$$E_{stat}^- + A_{mob}^- \rightleftharpoons A_{stat}^- + E_{mob}^- \tag{2.12}$$

where A represents the anion transported in the injected sample and E the counter-anion bonded to the grafted groups. Every ion-exchange reaction has its equilibrium constant, provided by equation 2.13:

$$k_A = \frac{[A^-_{stat}] \times [E^-_{mob}]}{[E^-_{stat}] \times [A^-_{mob}]} \tag{2.13}$$

The K_A value is specific for each ion. Separation is provided by this value. The eluent, in fact, keeps on passing through the column, and the exchanged anions are released towards the detector. The release time after injection depends on ion mobility, especially on its size and charge: the smaller and less charged the ion is, the easier is to remove it from the column-exchange groups, and so the shortest its retention time is. For instance, release times of the most common anions increase as follows: F^- > Cl^- > HNO_3^- > Br^- > NO_3^{2-} > PO_4^{3-} > SO_4^{2-}. Sensibility of the instrument is determined by the α parameter, i.e.:

$$\alpha = \frac{K_2'}{K_1'} = \frac{t_{R_2} - t_0}{t_{R_1} - t_0} \tag{2.14}$$

which is the ratio between the "capacity factors" of two different anions, calculated through the relation $K_i' = t_{R_i} - t_0$, where t_{R_i} is the retention time and t_0 the "dead time" after injection.

When ions are released by the column, the conductivity detector records a great increase of the conductivity of the solution, followed by immediate decrease when all the ions are passed by. This results in a peak in the chromatogram. Different peaks correspond to different retention time, i.e. to different ions. Concentration is related to specific conductivity of the solution through the following law:

$$\sigma = \frac{\Lambda \times c_{eq}}{1000} = \frac{\Lambda \times c \times z}{1000} \tag{2.15}$$

where c is the concentration of the ion, and z is its charge. The peak is given when a variation of conductivity occurs: $\Delta\sigma \propto c_{eq}(\Lambda_A - \Lambda_E)$ where E and A stands for Eluent and Anion, respectively.

Retention times and thus the exact peaks positions depend on many parameters, most of all the pH of the eluent and the flow rate. An example of chromatogram obtained with the anionic column Metrosep Anion Dual 1 by Metrohm^{TM} is shown in figure 2.2.2 (taken from constructor's leaflet).

In the figure, the *system peak* is labelled "7". It consists in a negative peak which is given by the addition of the sample aliquot to the analyzed solution: when sample is

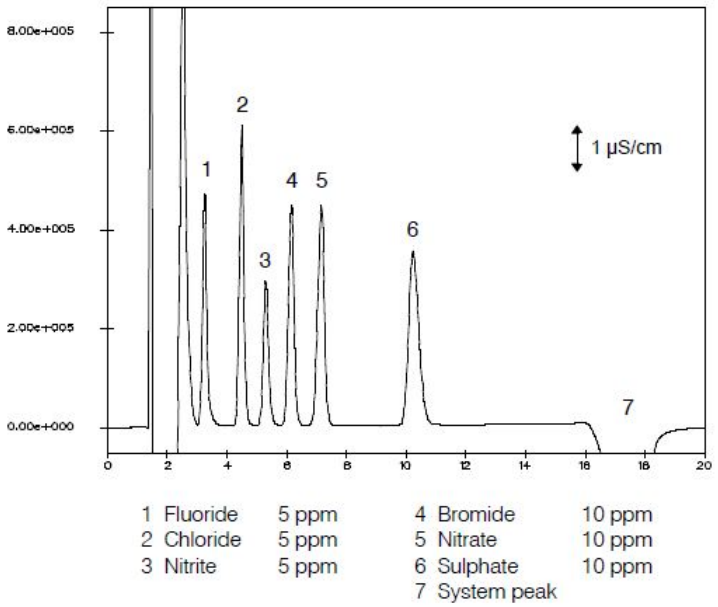

Figure 2.2.2: Example of chromatogram, as shown in Metrosep^{TM} Anion Dual 1 technical documentation (y axis: specific conductivity, [μS/cm]; x axis: retention time, [min])

added, in fact, a negative amount of eluent is pumped through the column and towards the detector, thus a fall in the conductivity is registered.

The instrument calibration is necessary to determine to which ion corresponds each peak in the chromatogram and, at the same time, to correlate the peak height and/or area to the effective concentration of the ion. To do this, one can use either an internal or an external standard calibration. In the first case, a full model is required to understand the exact conductivity variation as a function of ion concentration. One must have several parameters for this model, such as eluent pH, viscosity, temperature, eventual eluent contamination, etc. The direct method (i.e. the external standard calibration) requires to make an hypothesis on the ions present in the analyzed sample. Then, some standards with known concentration are prepared and analyzed through the HPLC. The minimum number of standards can be 2, because of the well-known linearity of the technique, but normally three solutions are prepared. In the present work, this method has been followed and details about it are reported in section 5.3.

For a deeper description of HPLC, the reader should refer to more technical texts, for instance ref. [66].

2.3 Gas absorption specific surface measurements

The use of gas adsorption to understand surface morphology of powdered samples is very often reported in literature, and the backstanding theory being very huge, the review of it is not the aim of this work. The present section wants to be a brief overview on some fundamentals aspects of the technique.

The adsorption of gas molecules to a solid is a common phenomenon due to weak interactions (Van der Waals) between the surface atoms and the gaseous molecules. The opposite phenomenon, i.e. the release of gaseous molecules, is called "desorption". The gas which is employed in this work to perform specific surface measurements is the molecular nitrogen, N_2: this phase is in equilibrium, at each pression, between the adsorbate state and the gaseous state. At costant temperature, one can register the evolution of the repartition of nitrogen between the two phases as a function of the pressure, which can grow from 0 to P_0, i.e. the saturation vapor pressure of the nitrogen. This variation is called "adsorption isotherm". More precisely, the recorded isotherm plots the volume of nitrogen adsorbed for each gram of powder against the relative pressure, i.e. P/P_0. After reaching the highest relative pressure, desorption can begin. The desorption isotherm can differ from the adsorption one, and this is revealing of a certain kind of porosity.

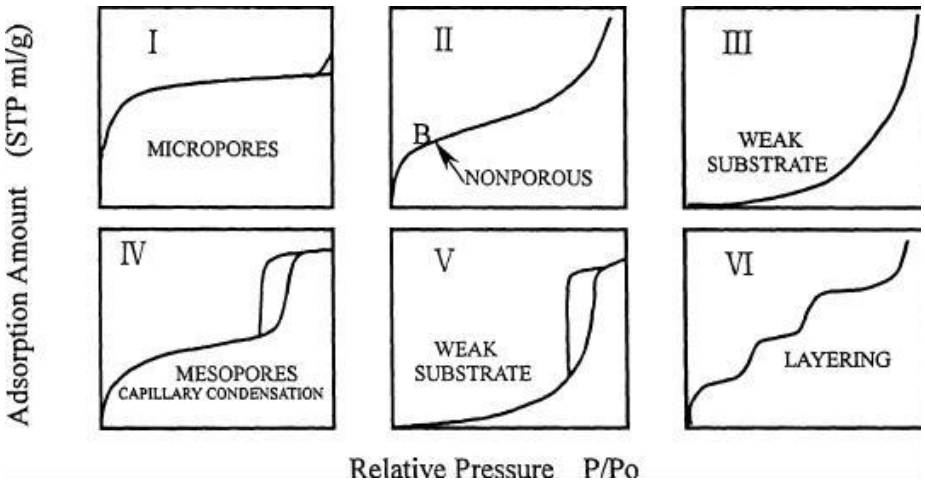

Figure 2.3.1: Adsorption/desorption isotherms according to IUPAC

Figure 2.3.1 shows the IUPAC classification of isotherms, and the corresponding porosity. In fact, when pores are present in the sample, lower pressures are required to remove the adsorbate from their inside. This turns out in a detachment of the desorption curve

from the adsorption one, and the position and of this detachment, i.e the shape of the hysteresis, indicates the pore size and shape. The discussion of this point is not related to our work, because, as the reader will see, no relevant porosity is found in our samples. Let's remember for the reader's interest that porosity is commonly classified in microporosity (d_{pore} < 2 nm), mesoporosity (2 nm < d_{pore} < 50 nm) and macroporosity (d_{pore} > 50 nm).

The specific surface area is measured through the BET (Brunauer, Emmett and Teller) method [10]. This method is based on an extention of Langmuir's theory of multimulecular adsorption, and the BET equation is supposed to be true:

$$\left(V_{ads} \times \left(\frac{P}{P_0} - 1\right)\right)^{-1} = \frac{1}{V_{mono} \times C} + \left(\frac{C-1}{V_{mono} \times C}\right) \times \frac{P}{P_0} \tag{2.16}$$

where V_{ads} and V_{mono} are the volume of the adsorbate gas and of a monolayer of gas. P is the pression to which the sample is exposed. C is a constant depending on the gas properties, according to the expression:showing

$$C = e^{\frac{E_1 - E_L}{RT}} \tag{2.17}$$

in which E_1 and E_L represent the heat of adsorption of the first layer and the heat of liquefaction, respectively, R is the gas constant and T the temperature of the sample. The BET theory is valid in the hypothesis that gas molecules adsorb on a solid in infinite layers, and the Langmuir theory can be applied to each layer. Moreover, it is supposed that there's no interaction between two layers. The BET function, i.e. the first member of eq. 2.16, is plotted against P/P_0 and results to be linear for relative pressures comprise between 0.05 and 0.35, and for type II or IV of IUPAC adsorption isotherms.

Theoretically slope and y-intercept of the BET plot are respectively $(C-1)/(V_{mono} \times C)$ and $1/(V_{mono} \times C)$ and they can easily return the V_{mono} value, which is used in equation 2.18:

$$S_{BET,\ total} = \frac{V_{mono} \times N_A \times A_M}{V_M} \qquad S_{BET,\ specific} = \frac{S_{BET,\ total}}{m} \tag{2.18}$$

where N_A and A_M are the Avogadro's number and the adsorption cross section of the adsorbing species (16.2 Å^2 for N_2), respectively, and V_M is the molar volume of liquid adsorbate (34.7 cm^3/mol for N_2), since the measure is performed at gas condensation temperature. The total BET surface is divided per the sample's mass, m, and this gives the

specific surface area, expressed in m^2/g.

In the present work, the BET method reliability has been confirmed by the goodness of the linear correlation factor of the first 7 points of the BET plot, as explained in section 5.4.

Chapter 3

Statement of the problem

Fluorine and Strontium are well-known doping agents for hydroxyapatites employed in biomedical applications, because they both improve the phosphate bioactivity in many ways. This is confirmed by the increased number of publications throughout the years investigating the role of F^{-} and the role of Sr^{++} ions in hydroxyapatite (see figure 3.0.1, searching inputs: “fluorine AND hydroxyapatite” or “strontium AND hydroxyapatite”). F+Sr doped hydroxyapatites or biphasic Ca phosphates could easily find an application as bone scaffolds.

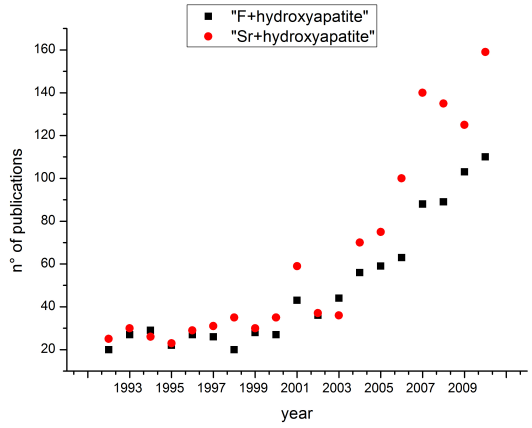

Figure 3.0.1: Number of publications containing the term “Hydroxyapatite” and “fluorine” or “strontium” vs year of publication, according to ScienceDirect, 2010

However, it seems that exists a lack in literature concerning the structural description of a Sr-F codoped product. Some studies in this sense have been reported by Thuy and

co-workers [93], who showed the remineralization improvement on caries-like lesions on dental enamel samples immersed in aqueous solutions containing different concentrations of fluoride and strontium ion. This confirmed the results obtained by M. Curzon in 1988 [14]. The cationic/anionic co-substitution has been investigated by more than one author, as for instance Kannan et al. [47], Yang et al. [101] and Badraoui et al. [1] (see also section 4.4), but as far as we know no systematic study has been performed to understand the biological effects of Sr and F atoms directly incorporated in the product (and not, e.g., up-taken from a solution). Before *in vitro* studies, structural and crystallographic characterizations are needed first.

In the present work, we aim to synthesize and characterize a preliminary series of F-substituted hydroxyapatite nanopowders. Its main structural properties, like phase composition, crystallite size, calcination weight loss, and lattice parameters will be investigated through Rietveld refinement of XRD patterns recorded on powders. The F-doping will be performed also over calcium phosphate powders with nominal Ca/P molar ratio different from the apatite's stoichiometric 1.67 to understand the influence of fluoride addition on apatite phase stabilization. Two paths will be followed to achieve this F-doping: a one-step fluorination with the introduction of the doping agent in the synthesis solution, and an aqueous solution fluorination of previously prepared phosphates.

Then the Sr and F co-substituted synthesis will be performed to obtain products with general chemical formula $Ca_{10-y}Sr_y(PO_4)_6OH_{2-x}F_x$. All the samples will be characterized from the structural point of view via Rietveld refinement of the recorded XRD patterns. The influence of both F and Sr doping on phosphate and fluoride release in acid conditions will be discussed through an original ion-exchange chromatography technique.

Part II

Experimental

Chapter 4

Synthesis procedure for pure and doped hydroxyapatite nanopowders

In the following paragraphs the experimental procedure for the synthesis of pure and doped hydroxyapatite (HA) powders will be shown.

4.1 Choice of the synthesis method

Many methods are reported in literature concerning the synthesis of well crystallized hydroxyapatites starting from a soft-chemistry approach. As a matter of fact, several ways are eligible to synthesize nanopowders composed of this phase. A significant resume of the works in which F-doping is performed over hydroxyapatites for biomedical applications is reported in table 4.1.1.

At the present state of the art, the most common soft-chemistry approach methods are the sol-gel and the precipitation one. Preliminary studies (not reported) have been made to achieve a synthesis of pure HA in both ways. Table 4.1.2, adapted from reference [77], resumes the main advantages and disadvantages of the most recent methods for the synthesis of nanostructured bioceramics.

While sol-gel is a very powerful and useful synthesis technique, especially in order to control microstructure and porosity of the final product, the precipitation method has been selected for further experiments in the present work because of its great diffusion in literature, its easy application, and in order to be able to compare our results with previous works, especially the ones reported by Sandrine Renaudin from the LMI (Laboratoire

Author	Ref	Year	Method	F-doping agent
Basar et al.	[3]	2010	precipitation	NH_4F
Kanchana, Sekar	[46]	2009	single diffusion gel	NaF
Kim et al.	[50]	2003	solid state reaction	CaF_2
Sivakumar, Manjubalar	[89]	2001	LT hydrothermal or HT solid state reaction	HF or NaF
Darroudi et al.	[15]	2010	sol-gel	NH_4F
Bianco et al.	[6]	2010	precipitation	NH_4F
Eslami et al.	[23]	2009	coprecipitation "pH-cycling"	NaF
Cai et al.	[11]	2009	sol-gel	HPF_6
Fathi et al.	[24, 25]	2009	mechanical alloying	CaF_2
Zhu et al.	[106]	2008	BCP porous blocks immersed in ZnF_2	ZnF_2
Zhai et al.	[104]	2007	sonoelectrodeposition + ion exchange	NaF
Wang et al.	[98]	2006	sol-gel	HPF_6
Harrison et al.	[37]	2004	coprecipitation	NH_4F
Miao et al.	[69]	2005	sol-gel	HPF_6
Yao et al.	[102]	2009	precipitation	NaF

Table 4.1.1: Status of art in F-doped hydroxyapatites obtained by soft chemistry techniques

des Metériaux Inorganiques) laboratories in the Upper National School of Chemistry in Clermont-Ferrand (France), as described in ref. [32]; that synthesis method was there employed to obtain Si-doped HA nanopowders, and here modified.

The “precipitation method” described later is based on an acid-base neutralization, as

Method	Advantages	Disadvantages
Precipitation under low T, microwaves, US	simplicity, low production cost, high purity, good stoichiometry control, fine particles with narrow size distribution	agglomeration of particles and residual surface contamination
Sol-gel synthesis	possibility to grow nanosized particles in different matrices, high purity	properties depend on hydrolysis and drying rate
Micelles/ microemulsion	size control by reactive precursor concentration in micelle	high amount of surfactant, sensitive to temperatures
Mechanical deformation	possibility to produce immiscible systems nanomaterials	contamination from the deformation instruments (e.g. milling media) and bad control on particle size and shape
Vapor condensation (sputtering, laser...)	highest purity, high density, fast and directional, ultrafine particle size with narrow size distribution	high costs, low yields
Spray pyrolysis	high purity and homogeneity, high size control	huge quantity of solvent is wasted, low yields
Flame decomposition	commercial quantity production suitable	difficult control of size and shape

Table 4.1.2: Advantages and disadvantages of different synthesis method for nanostructured bioceramics, adapted from ref.[77]

explained by the 4.1 reaction.

$$10Ca(NO_3)_2 \cdot 4H_2O + 6(NH_4)H_2PO_4 + 12NH_4OH \rightarrow \\ \rightarrow Ca_{10}(PO_4)_6(OH)_2 + 20NH_4NO_3 + 24H_2O \tag{4.1}$$

In this reaction, $Ca(OH)_2$ may take the place of Ca nitrate, as well as other phosphates can replace the ammonium dihydrogenphosphate. Some works report in fact the use of phosphoric acid as reactant, together with calcium hydroxide. See for comparison ref.

[53], [71],[7], and [1].

An alkaline pH environment is necessary for the reaction to take place: the use of several bases is reported in literature, such as *NaOH* or *KOH*. We decided to keep the system as chemical homogeneous as possible, so the presence of an ammonium phosphate led to the choice of the ammonium hydroxide.

A detailed description of precipitation mechanisms leading to hydroxylapatite formation is given by Liu and co-workers [60]. The kinetics of hydroxyapatite precipitation at pH 10 to 11 involves several forms of Ca phosphates, according to the suggested conversion:

$$OCP \overset{very\ soon}{\rightarrow} ACP \rightarrow DAP \rightarrow HAP$$

where OCP stands for Octacalcium Phosphate ($Ca_8H_2(PO_4)_6{\cdot}5H_2O$, with Ca/P=1.33), rapidly converted in ACP (Amorphous Ca phosphate, $Ca_3(PO_4)_2{\cdot}xH_2O$, where Ca/P=1.50). XRD patterns supporting this phase existence hypothesis are shown later, labelled "as dried sample". If the solution has enough time to evolute, an apatite or apatite-like phase begins to appear.

First, the Ca-deficient form is observed (DAP), with a chemical formula:

$$Ca_{10-z}(HPO_4)_{6-z}(OH)_{2-z}$$

Then, before the formation of stoichiometric hydroxyapatite (HAP), a mixed form of phosphate is supposed to occur, according to the $Ca_{10\text{-}z}(HPO_4)_z(PO_4)_{6-z}(OH)_{2-z}) \cdot nH_2O$ formula (becoming ACP with z=1, and HAP with z=0). More precisely, Liu and co-workers suggest the possibility that DAP is made of fractions either of ACP or HAP, so it could be expressed in the form of $mACP + nHAP$, where $n, m \leq 1$.

The aging time necessary to obtain apatite formation depends on the temperature, as well as on the pH of the solution. For our purposes, an aging time has been neglected, while a calcination was always performed.

4.2 Synthesis of pure Calcium hydroxyapatite powders by precipitation method

Here follows the description of the standard synthesis procedure adopted through all the present work. All chemical products have been provided by Sigma-Aldrich®, reagent-grade. The water used in all described synthesis has been preliminarily treated and deionized to reach the high purity grade. The pH-meter was provided by Mettler-Toledo (S20 SevenEasy™ pH) and its recalibration was performed about every 2 days as recommended by the producer. Uncertainty on the synthesis weight is ± 0.0002g (due to weighting + zero calibration).

1. A stoichiometric amount of PO_4^{3-} precursor, the ammonium dihydrogenphosphate ($(NH_4)H_2PO_4$, CAS number: 7722-76-1) is added and dissolved under magnetic stirring in 100 mL of water.

2. Meanwhile, a 100 mL water solution with stoichiometric amount of Ca^{2+} precursor was prepared in the same way using calcium nitrate tetrahydrate ($Ca(NO_3)_2{\cdot}4H_2O$, CAS number: 13477-34-4).

3. pH of both solutions has been controlled using 30% volumetric Ammonium hydroxide solution in water ("Ammonia water", NH_4OH, CAS number: 1336-21-6), whose starting pH was about 13. PO_4^{3-} containing solution and Ca^{2+} containing solution basicity were controlled and set respectively to pH$\approx$10 and pH$\approx$11 by adding 7 mL and 0.5 mL of ammonia water. In both solutions pH showed a non significant variation when considering different synthesis.

4. When pH equilibrium was reached, the PO_4^{3-} containing solution was added drop-by-drop in about 3h to the Ca^{2+} containing solution by means of a dropping funnel, as shown in figure 4.2.1. After about 90 mins (half of final mixing time), the pH was monitored and kept over 10 by adding the needed amount of ammonia water (ca. 5 mL). A formation of white precipitates was observed at the very beginning of the drop-by-drop mixing.

5. After the complete addition of the first solution to the second one, pH was again adjusted over 10, then the milk-colour solution was left under soft stirring for 24h at

room temperature.

6. The final slip is then filtered through a paper filter supported on a Büchner funnel connected to a side-arm flask by means of a rubber adapter, with a tube leading to a low-vacuum pump (p≈200 mbars). Powders are then rinsed twice with Ethanol (96% purity) and twice with water. This operation required about 45 mins.

7. The white filtrate is then dried on a glass support to 102.5°C overnight to obtain the "cake", then manually ground by an agate mortar in order to reduce the mean size of the particles and make evaporation easier. Resulting powder is then dried again for about 2h in order to eliminate residual solvent traces, and manually milled again into a fine powder by means of the agate mortar and pestle (see figure4.2.1)

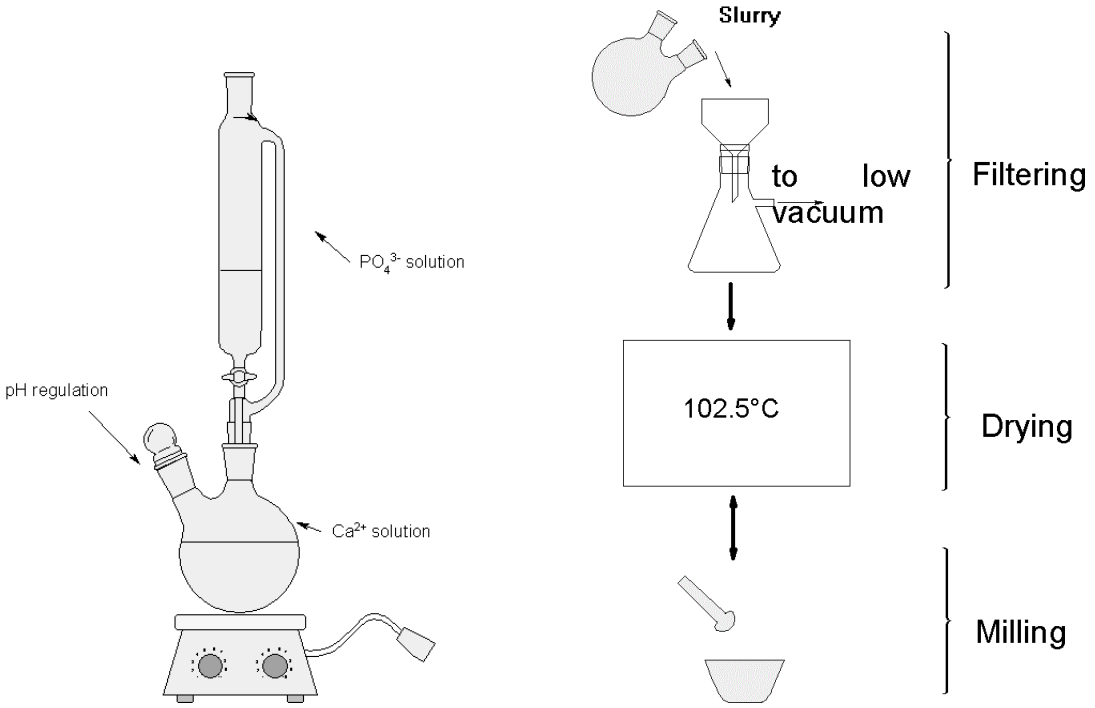

Figure 4.2.1: The drop-by-drop mixing procedure (left) and the filtering, drying and milling operations (right)

Further thermal treatments are required in order to obtain a high cristallinity degree of the HA powders.

As described in the previous paragraph, if enough time is left to the precipitate, spontaneous formation of hydroxylapatite can result even without further thermal treatment. Figure 4.2.2 shows XRD pattern of as-dried calcium phosphate obtained with the above described procedure, compared to a similar product previously aged for 24h in its mother liquor, without stirring, and then dried to 102.5°C (data provided by doct. O. Raissle, LMI ENSC Clermont-Ferrand).

A 4h 900°C treatment was chosen for all samples (heating rate: 10°C/min). The calcination process has been conducted in air flux (Nabertherm™ 1 zone tubular furnace). The value of 900°C has been selected in order to investigate the ability of fluorine to stabilize HA with respect to TCP (beta or alpha form), as it is reported that this is the stability limit of HA form in many works (see the 1.3 section for details). An overview of thermal treatments adopted in the recent literature is given in table 4.2.1. Only works employing a synthesis procedure similar to ours are here considered.

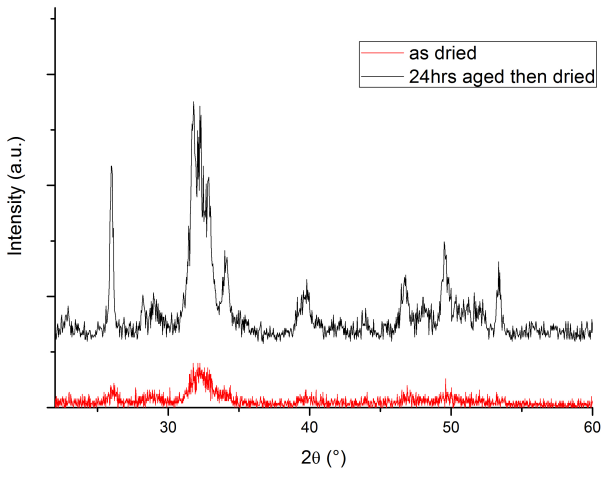

Figure 4.2.2: XRD patterns of as-dried sample of hydroxyapatite (red) and a previously 24h aged then dried sample (black)

Author	Ref	Year	Temperature (°C)	Time (h)
Basar et al.	[3]	2010	600, 900, 1100, 1300	0.5, 1
Eslami et al.	[23]	2009	1000	1
Harrison et al.	[37]	2004	900	1
Yao et al.	[102]	2009	-	-
Chinthaka Silva et al.	[12]	2008	-	-
Gross	[33]	2004	900	1
Pang et al.	[76]	2003	650	6
Kannan et al.	[48]	2006	900	2
Rodriguez-Lorenzo et al.	[83]	2003	900	2

Table 4.2.1: Brief overview over thermal treatments adopted in recent precipitation-based synthesis publications

4.3 F-doped HA powders

Many suitable F-containing compounds are reported in recent literature in order to employ them as doping agents to obtain F-doped hydroxylapatite nanoparticles (named FHA in the present work). As confirmed by the overview given in table 4.1.1, the most common Fluorine precursors are Sodium Fluoride (NaF) or Ammonium Fluoride (NH_4F). Both are comparable in terms of solubility and availability, as well as chemical behavior in the described above environment.

In the present work NH_4F was chosen as F-doping agent for its chemical affinity to the mentioned reactants, i.e. not to introduce further cation species in the synthesis solution; even if previous works reported that the presence of Na^+ does not result in the formation of Na phosphates, or in the presence of interstitial Na atoms in HA lattice, this event appears to be is less probable with the bigger NH_4^+ ion[1]

NH_4F was added to the PO_4^{3-}containing solution in stoichiometric amount, together with $(NH_4)H_2PO_4$, to obtain a F-doped series of HA nanopowders, with chemical formula $Ca_{10}(PO_4)_6(OH)_{2-x}F_x$ (with $0 \leq x \leq 2$). The pure hydroxyapatite and the pure fluorapatite samples are named respectively HA and FA, while samples with x=0.5, 1 and

[1]ionic radii: $r_{NH_4^+} = 1.47$Å, $r_{Na^+} = 1.02$Å

1.5 are named respectively 0.5FHA, 1FHA and 1.5FHA. This choice made the samples described in the present work similar but complementary to the ones reported by K. Gross, L. Rodriguez-Lorenzo and co-workers [33, 34, 35, 37].

Three different series of nanopowders were prepared, with different values of Ca/P ratio, in order to assess the ability of fluorine to stabilize the Apatite phase with respect to other Ca phosphates: a Ca/P=1.28, a Ca/P=1.50, and a Ca/P=$1.\bar{6}$ series (labelled Ca/P=1.67), with nominal relative of $\pm 0.01\%$ (for details about the Ca/P value in HA, see section 1.3). 5g of each sample were prepared as described above, detailed amounts of reactants are show in table 4.3.1.

As every mole of HA contains 10 mols of Ca, the *nominal x* value was calculated starting from the nominal molar amount of Ca and F in the synthesis solutions, with the simple relationship $x = \frac{mols\,of\,F}{mols\,of\,Ca} \times 10$, regardless of the phase composition of the samples. The uncertainty on the nominal *x* value is ± 0.001.

Sample name	**$Ca(NO_3)_2 \cdot 4H_2O$ (g)**	**$(NH_4)H_2PO_4$ (g)**	**NH_4F (g)**	**Ca (mol)**	**P (mol)**	**F (mol)**	**nominal Ca/P**	**nominal *x***
$HA_{1.67}$	11.7594	3.4359	0.0000	0.0498	0.0299	0	1.6671	0
$0.5FHA_{1.67}$	11.7683	3.4452	0.1045	0.0498	0.0299	0.0028	1.6639	0.5662
$1FHA_{1.67}$	11.7398	3.4365	0.1869	0.0497	0.0299	0.0050	1.6640	1.0151
$1.5FHA_{1.67}$	11.7218	3.4245	0.2763	0.0496	0.0298	0.0074	1.6673	1.5029
$FA_{1.67}$	11.7277	3.4320	0.3865	0.0497	0.0298	0.0104	1.6645	2.1013
$HA_{1.50}$	11.7509	3.8113	0.0000	0.0498	0.0331	0.0000	1.5018	0.0000
$0.5FHA_{1.50}$	11.7854	3.8685	0.0982	0.0499	0.0336	0.0027	1.4840	0.5313
$1FHA_{1.50}$	11.7516	3.8485	0.1839	0.0498	0.0335	0.0050	1.4874	0.9978
$1.5FHA_{1.50}$	11.7203	3.8076	0.2840	0.0496	0.0331	0.0077	1.4994	1.5450
$FA_{1.50}$	11.7198	3.8134	0.3770	0.0496	0.0332	0.0102	1.4970	2.0510
$HA_{1.28}$	11.5550	4.3900	0.0000	0.0489	0.0382	0.0000	1.2821	0.0000
$0.5FHA_{1.28}$	11.5456	4.3798	0.0936	0.0489	0.0381	0.0025	1.2841	0.5169
$1FHA_{1.28}$	11.5536	4.3823	0.1846	0.0489	0.0381	0.0050	1.2842	1.0187
$1.5FHA_{1.28}$	11.5497	4.3707	0.2856	0.0489	0.0380	0.0077	1.2872	1.5767
$FA_{1.28}$	11.5070	4.3820	0.3628	0.0487	0.0381	0.0098	1.2791	2.0103

Table 4.3.1: Synthesis details: F-doped Ca/P=1.28 series (down), Ca/P=1.50 series (middle) and Ca/P=$1.\bar{6}$ series (up)

4.4 Sr-F codoped HA powders

Author	Ref.	Year	synthesis method	notes
Stranick, Root	[91]	1991	-	immersion of HA in Sr^{2+} containing medium, observation of F^- uptake from monofluorophosphate
Yang et al.	[101]	2010	-	incorporation of several elements by calcium phosphate films in multi-well tissue culture plates
Hill et al.	[42]	2004	traditional reagent-melting glass fabrication	synthesis of Sr and F-doped bioglasses with Ca/P=1.67
Thuy et al.	[93]	2008	-	observation of human enamel remineralization in samples treated in F^- and Sr^{2+}+F^- containing solutions
Featherstone et al.	[26]	1983	precipitation, SrF_2 and NaF used as doping agents	studies on acid reactivity and chemical analysis of carbonated apatites
Badraoui et al.	[1]	2009	precipitation	many co-substitutions assessed
Michie et al.	[70]	2008	-	Atomic scale local density functional simulations and configurational averaging predicion of mixed Sr-F-doped apatites structure

Table 4.4.1: Review on Sr-F co-doping status of art

Details on the biological role of Sr in Sr-doped hydroxyapatites are reported in the fist part of this work.

The substitution of Sr^{2+} ion for Ca^{2+} is made possible by the high chemical affinity of the two cations. Sr substitution will be expressed by the *y* value in the chemical formula of hydroxyapatite, i.e. $Ca_{10-y}Sr_y(PO_4)_6(OH)_2$.

A huge X ray diffraction and Rietveld Refinement characterization of Sr-substituted apatites (included the synthesis of totally substituted apatite, named SrHA) is reported by Bigi et al. [7]. Synthesis procedure was similar to the one adopted in the present work, but no thermal treatment was performed after the drying step. Another important Rietveld Refinement characterization of Sr-substituted apatites has been made by Renaudin et al. [80].

Although Sr and F are very well-known doping agents for biomedical apatites, there seems to be a lack in literature concerning the synthesis of co-doped Sr-F apatite nanopowders. A resume of actual status of the art in this field is given by table 4.4.1.

The synthesis procedure for Sr-F codoped apatites is very similar to the one described above. Strontium nitrate ($Sr(NO_3)_2$, 99.995% trace metal basis, CAS number 10042-76-9) was added to the Ca^{2+} containing solution in stoichiometric amount to reach the desired value of *y*. A diagonal doping has been selected for this series: as the Sr content increases, the F content increases too, in order to establish the influence of both ions in stabilizing whether the apatite or the TCP (alpha or beta form) phase. Samples were labelled *y*Sr*x*F, where *y* and *x* are the content of Sr and F according to the formula: $Ca_{10-y}Sr_y(PO_4)_6(OH)_{2-x}F_x$. A further sample was prepared, fully substituted in F but poorly Sr-doped, in order to assess its solubilization properties as described later. The (Sr+Ca)/P molar ratio was set to $1.\bar{6}$ (labelled 1.67) for all the samples. Details on the Sr-F-codoped series are shown in table 4.4.2. We did not pursuit the total Sr substitution because a complete Sr-fluorapatite is not interesting from the biomedical point of view (50% atomic substitution is already a high doping).

Sample name	**$Ca(NO_3)_2{\cdot}4H_2O$ (g)**	**$Sr(NO_3)_2$ (g)**	**$(NH_4)H_2PO_4$ (g)**	**NH_4F (g)**	**Ca (mol)**	**Sr (mol)**	**P (mol)**	**F (mol)**	**nominal $\frac{Ca+Sr}{P}$**	**nominal y**	**nominal x**
05Sr05F	10.9251	0.5215	3.3567	0.0939	0.0462	0.0024	0.0291	0.0025	1.6698	0.5057	0.5201
1Sr1F	10.0893	1.0078	3.2736	0.1762	0.0427	0.0047	0.0284	0.0047	1.6686	1.0028	1.0018
2Sr1.5F	8.5776	1.9201	3.1304	0.2522	0.0363	0.0090	0.0272	0.0068	1.6681	1.9986	1.5000
5Sr2F	4.7536	4.2463	2.7704	0.3028	0.0201	0.0201	0.0241	0.0082	1.6689	4.9919	2.0340
05Sr2F	10.8715	0.5207	3.3437	0.3606	0.0460	0.0025	0.0291	0.0097	1.6684	0.5073	2.0075

Table 4.4.2: Synthesis details: the Sr-F codoped series

4.5 Aqueous solution fluorination

Although many authors suggest that F^- ion is supposed to easily enter in the HA lattice because of its smaller size in comparison with OH^-group[2], it seems that recently not so much work has been made in order to investigate the possibility to fluoridate hydroxyapatite powders through immersion in a F^- containing solution. Particularly, it's not definitely been cleared whether the fluorination involves just the surface or the bulk material.

Understanding the mechanism of aqueous solution fluorination of apatites could provide us a model for explaining the similar fluorination of enamel surface, which is known as effective prevention of tooth decay by caries and is extensively used in clinically practice. As reported by Tanaka and co-workers, this aspect has been left to dental therapists studies for many years, but recently it seemed necessary to face the phenomenon from a chemical point of view [92]. A surface-based approach was followed by Rodriguez-Lorenzo and Gross in 2004 [84], who concluded that fluorapatite-covered hydroxyapatite particles can be obtained starting from high specific surface powders, low pH and high F^- ion concentration. No fluorite (i.e. calcium fluoride, CaF_2) formation was observed in that work.

By the way, the F^- uptake by HA has been studied in the past, as for example by Lin, Raghavan and Fuerstenau in 1981, or Menzel and Amberg in 1971 ([59],[67]). The mechanism of F^- incorporation by HA has also been theoretically modeled by N. De Leeuw [54] and by Nelson and Higuchi in 1970 [74]. Among the many models proposed, we'd like to summarize the ones referred by Lin and co-workers and by the subsequent literature:

1. **OH^-/F^- exchange** on HA, based on observations by McCann (1952, ref. [64]) and Leach (1959), that found out that fluorapatite was formed when low concentration of F^- was employed. The model consists in a substitution of F^- ions for OH^- ions in the apatite lattice structure, as shown by reaction 4.2:

$$Ca_{10}(PO_4)_6(OH)_2 + 2F^- \rightleftharpoons Ca_{10}(PO_4)_6F_2 + 2OH^- \tag{4.2}$$

   According to this model, a basification of the aqueous medium should be observed.

[2]the real values depend on ionic environment, and there are discrepancies in literature, such as $r_{F^-} = 1.32$Å, $r_{OH^-} = 1.68$Å, reported by Rodriguez-Lorenzo et al. [85], or $r_{F^-} = 1.36$Å, and $r_{OH^-} = 1.40$ Å by Lin et al. [59].

When F^-concentration increases (Lin and co-workers report $\approx 100ppm$) a fluorite crystallization accompanies the partial HA lattice disintegration, as shown in reaction 4.3

$$Ca_{10}(PO_4)_6(OH)_2 + 20F^- \rightleftharpoons 10CaF_2 + 6PO_4^{3-} + 2OH^- \tag{4.3}$$

2. **Spinelli et al.** [90] proposed a mechanism involving the dissolution of the solid hydroxyapatite followed by precipitation of fluorapatite via recrystallization and removal of fluoride ions by adsorption and ion exchange.

3. **Ramsey and co-workers** [78] proposed a pH-varying model: at pH<4, a partial dissolution of HA occurs, followed by precipitation of fluorite, which is converted in FA after increasing the pH.

4. **Nelson and Higuchi**, in a theoretical model, suggested that CaF_2 forms initially at the hydroxyapatite/solution interface and that the solid boundary progresses, as shown by figure 4.5.1

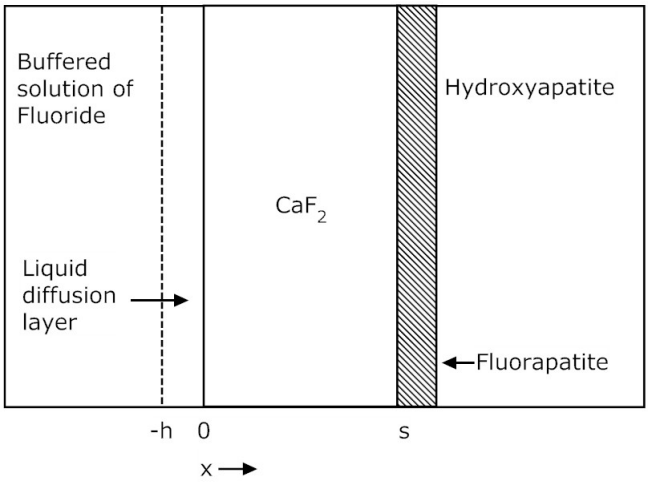

Figure 4.5.1: The formation of FA in a F^- buffered solution, after Nelson and Higuchi [74]

We can resume the above mentioned works in some simple considerations: the F^- uptake by HA depends on many parameters, such as temperature, pH, specific surface of the powder, presence of ions different from Ca^{2+}, PO_4^{3-}, F^-, and related counter-ions, and of course fluoride concentration.

Concerning the pH value, it's worth to say that in acid medium, dissolution of hydroxyapatite occurs more rapidly, and this provides a huge Fluorapatite formation according to the mechanisms 2 and 3. Moreover, a high value of pH means a greater availability of OH^- ions, which compete with the equilibrium stated by mechanism 1. On the other side, fluorite is more stable at low pH values, and fluorapatite formation is inhibited. The depth of fluorapatite coating which is formed after the fluorination depends on F^- availability (i.e. F^- concentration) and on time left to the reaction.

As we already declared, there's not a standard procedure in literature that provides a suitable method for an aqueous solution fluorination. Some report the need of using a supporting electrolyte to keep the F^- and Ca^{2+} diffusion rate constant, but the best concentration to achieve is not sure.

Aiming to simulate the real oral environment, we chose to set the experiment in a neutral pH. The pH of saliva is commonly not constant, and varies from a minimum of about 5, to a maximum close to 7.5. The variation of saliva pH versus time after sucrose rinse in a volunteer's mouth is called "Stephan Curve". The main risks for enamel demineralization seem to occur when pH falls below the 5.5 value. Common deionized water presents usually a pH which is about 7.3, and after addition of 0.5g of powdered sample in 50mL of water, this value remained the same in most of the cases. When necessary, a small amount of NH_4OH diluted solution (30% vol) was used for re-equilibration. After one hour of equilibration, 0.37 g of NH_4F was added to the mixture in order to obtain an hypothetical F/Ca molar ratio of 0.2 as in fluorapatite formula. The real value of F/Ca depends on the product phase composition (i.e. on the molar mass of the product). No supporting electrolyte was used. The present work refers to the procedure described by Hammari and co-workers [36]. Another important contribute is given by Geetha and Buvaneswari [30].

The system was placed in a closed container, maintained at 37 ± 0.5°C by means of a silicone oil controlled temperature bath. After 24h, powders were filtered, rinsed and dried according to the already described standard procedure. As summarized in table 4.5.1, the following samples were prepared:

- Starting from raw products (i.e. not yet calcined), samples with nominal Ca/P ratio equal to 1.50, 1.67
- Starting from already calcined products with Ca/P nominal ratio equal to 1.50, 1.67

Samples were labelled whether *A* (calcination after fluorination, first series) or *B* (calcina-

tion before fluorination, second one) and 1.28, 1.50, 1.67, respectively. Characterizations by XRD and Rietveld Refinement technique, together with ion-exchange chromatography have been performed.

sample name	**Ca/P nominal ratio**	**Calcination step performed:**	
		Before Fluorination	**After Fluorination**
A-1.50	1.50		x
A-1.67	1.67		x
B-1.50	1.50	x	
B-1.67	1.67	x	

Table 4.5.1: Aqueous solution fluorinationion samples

Chapter 5

Characterization details: materials and methods

General concepts about the characterization techniques employed in the present work are reported in chapter 2. Here follows a detailed description of the parameters adopted for each technique, just in order to make the reproducibility of this work easier.

5.1 X-ray diffraction

Two kinds of XRD measurements are reported in the present work.

Just for phase recognition, fast XRD measurements were performed in a short angle range (20-60°) with scanning step of 0.02°, 0.5 seconds per step by a D5000 $\theta - 2\theta$ geometry Siemens Bruker diffractometer.

For Rietveld refinement, data were collected on finely ground powders by an X'Pert Pro Philips diffractometer, with $\theta - \theta$ geometry, equipped with a solid detector X-Celerator, no monochromator, and using Cu K_α radiation ($K_{\alpha 1}$ =1.5405980 Å, $K_{\alpha 2}$ =1.5444260 Å). A PW3064 spinner was used, divergence slit was fixed to 0.5°, and no monochromator was required. The generator voltage and tube current were set respectively to 40kV and 30mA.

A 0.0167° scanning step in the 3°-120° range has been adopted; for the preliminary Ca/P=1.67 series a 5 seconds per step acquisition time has been selected. This resulted in good quality data, but in obvious increasing of total measurement time (about 8h). Following data were collected with a 2 s/step acquisition time (total time≈3h), and the final

quality was still sufficient to perform Rietveld Refinement.

5.2 Rietveld Refinement

Rietveld refinements were performed using the FullProf.2k Multi-Pattern software in the 2005 LLB/LCSIM 3.20 version by Juan Rodriguez-Carvajal[1]. More details on this software are shown in the related manual [82]. For the precious help the fitting procedure and the interpretation of the results, Dr. Guillaume Renaudin is gratefully acknowledged.

The first step after phase recognition in each sample was writing a control file, named *sample.pcr*, which contains the basic information about the phases present in the pattern. A sample of this file has been reported in Appendix.

5.2.1 Fitting procedure

Refinement was performed in several stages, the parameters obtained in each step being deferred in the following one, according to this sequence: first, the scale factors for each phase have been refined, then the general zero shift, lattice paramaters, profile parameters, preferred orientation, atomic positions, occupancy factors (when necessary) and isotropic displacement parameter (temperature depending, B_{iso}) for each atom type. Finally, the background has been corrected through linear interpolation of several selected background points (usually 15 to 30).

Lattice parameters, atomic positions and occupancy factors were taken from ISCD[2] references, as resumed by table 5.2.1.

Atomic positions of minor phases, other than hydroxylapatite, were usually not refined, because this resulted in an increasing of the fitting parameters number without a corresponding improvement of the fitting itself.

Fluorapatite and hydroxyapatite show the same structure, with 7 independent atom positions: two Ca, one P and four O. In Fluorapatite unit cell, F atoms replace O atoms in the O4 oxygen position. This position is half occupied, and this corresponds to a statistically disordered 4e position around the 2a (0,0,¼) site. F and O response to x-rays are quite

[1] For further details on the program, see also J. Rodriguez-Carvajal and T. Roisnel, EPDIC- 8, 23-26 May 2002, Mater. Sci. Forum, 2004, 123, 443

[2] FIZ Karlsruhe Inorganic Crystal Structure Database, CopyRight ©2005 by Fachinformationszentrum Karlsruhe, and the U.S. Secretary of Commerce on behalf of the United States. http://icsd.fiz-karlsruhe.de/

phase	chemical name	chemical formula	space group symbol and crystal system	independent atomic positions	reference authors
Hydroxylapatite	Pentacalcium Tris(phosphate(V)) Hydroxide	$Ca_{10}(PO_4)_6OH_2$	$P6_3/m$ hexagonal	7	Rodriguez-Lorenzo et al. [83]
Whitlockite ($\beta - \mathbf{TCP}$)	Tricalcium Bis(phosphate(V)) Beta	$\beta - Ca_3(PO_4)_2$	R3c trigonal	18	Yashima et al. [103]
$\alpha - \mathbf{TCP}$	Tricalcium Bis(phosphate(V)) Alpha, Ht	$\alpha - Ca_3(PO_4)_2$	$P2_1/a$ monoclinic	78	Mathew et al. [63]
Lime	Calcium Oxide	CaO	$Fm\bar{3}/m$ cubic	2	Ganguly et al. [29]
Portlandite	Calcium Hydroxide	$Ca(OH)_2$	$P\bar{3}m1$ trigonal	2	Desgranges et al. [17]
β**-Ca pyrophosphate (CPP)**	Dicalcium Diphosphate Beta	$\beta - Ca_2(P_2O_7)$	$P4_1$ tetragonal	22	Boudin et al. [8]

Table 5.2.1: ISCD references for Rietveld Refinement

similar, because of their electronic similarity (Z_F=9, Z_O=8). Thus, it's not always possible to assess if the O4 position contribute to the overall reflection is due either to a fluorine atom or to an oxygen one. Then, the starting fitting parameters for FA were the same of HA. For details about this, see section 2.1.

As confirmed by previous literature [80], no significant improvements are achieved in the fit when considering the contribution of the H atom in the hydroxil group, so this has been ignored. Fore the same reason, anisotropic line broadening, microabsorption effects and the use of the monoclinic ordered structural description for HA instead of the hexagonal one were not taken into account. The average crystallite size parallel to crystallographic axes was refined. The use of a resolution function extracted by patterns recorded on NIST[3]

[3]National Institute for Standards and Technology

Lanthanum Hexaboride powder (LaB_6 660 b, see figure 5.2.1) allowed to have a better peak profile modelling and decreased the total number of refined parameters.

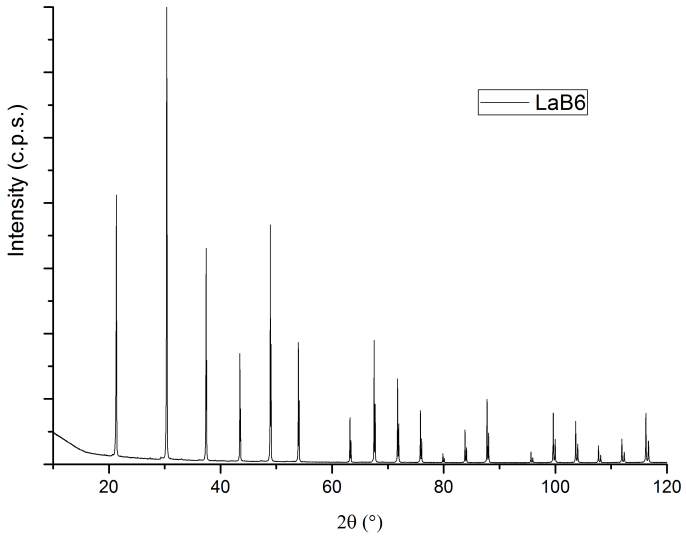

Figure 5.2.1: The LaB_6 standard for the Rietveld refinement resolution function

5.2.2 Mathematical hints

A Thomson-Cox-Hastings pseudo-Voigt function (TCH pseudo-Voigt, corresponding to number 7 in the Npr control variable) was used to fit the peak profile; here, Finger's treatment of the axial divergence is convoluted in the function. Eq. 5.1, taken from ref. [82], shows the classical pseudo-Voigt function:

$$\Omega(x) = pV(x) = \eta L'(x) + (1 - \eta)G'(x) \tag{5.1}$$

where η is comprised between 0 and 1, and represents the coefficient for a linear combination of a Lorentzian (L') and Gaussian function (G'), having the same Full Width at Half Maximum (FWHM), *H*. The peak profile is then described, other than by the x=θ variable, also by η and *H*: $pV(x) = pV(x, \eta, H)$. By the way, both the Lorentzian and the Gaussian functions can provide their own FWHM, named H_L and H_G, respectively, as shown in eq. 5.2 and 5.3.

$$H_L = [X + \xi D_{ST}(\alpha_D)]tan\theta + \frac{[Y + F(\alpha_Z)]}{cos\theta} \tag{5.2}$$

$$H_G^2 = [U + (1-\xi)^2 D_{ST}^2(\alpha_D)]tan^2\theta + Vtan\theta + W + \frac{I_G}{cos^2\theta} \tag{5.3}$$

In the resolution function provided by the user, V and W are fixed to zero, and the rest of parameters in the formula have a meaning in terms of strains (U, α_D, X) and size (Y, I_G, α_Z), while D_{ST} and F are functions whose expressions depend on the strain or size model used, and ξ is a mixing coefficient to mimic Lorentian contribution to strains.

The difference between the TCH pseudo-Voigt functions and the simple pseudo-Voigt consists in the calculation of the η parameter, which in the TCH-pseudo-Voigt is calculated starting from the two FWHM mentioned above; for a full and accurate mathematical description of the procedure, the reader should consult the FullProf software guide in ref. [82]. By the way, both the use of this kind of peak profile fitting function (or the simple TCH) and the use of a resolution function are required to gather microstructural information from the FullProf program. The microstructural file output by the software contains the analysis of the size and strain contribution to each reflection, i.e. it performs just a phenomenological treatment of line broadening in terms of coherent domain size and strains due to structural defects. However, since it exists a direct correlation between the coherent domain size and the grain size, the domain size data have been recorded and plotted against the F and/or Sr content of the samples. The coherent domain size is, actually, a more refined datum with respect to the grain size calculated through the Debye-Scherrer equation.

5.2.3 Agreement of the fitting

General agreement factors have been considered as indicated in the FullProf.2k manual. The Rietveld method minimizes the following function:

$$\chi^2 = \sum_{i=1}^{n} w_i \{y_{obs,i} - y_{calc,i}(\alpha)\}^2 \tag{5.4}$$

Where χ^2 depends on the difference between the observed intensity and the calculated intensity at the *i*-step (i.e. the 2θ value). α is the parameter vector, $\alpha = (\alpha_1, \alpha_2, \alpha_3, ...\alpha_p)$

and w_i is the weight factor for each *i*-step, depending on the reverse of the variance of the $y_{obs,i}$ value. The reduced chi-square takes into account the number of degrees of freedom, *n-p*:

$$\chi^2_v = \frac{\chi^2}{n-p} \tag{5.5}$$

The following factors (taken from ref. [82]) are considered when establishing the goodness of the fit. R_p and R_{wp} are respectively the profile factor and the weighted profile factor, as stated in eq. 5.6.

$$R_p = 100\frac{\sum_{i=1}^{n}|y_{obs,i}-y_{calc,i}|}{\sum_{i=1}^{n}y_i} \quad R_{wp} = 100\left[\frac{\sum_{i=1}^{n}w_i|y_{obs,i}-y_{calc,i}|^2}{\sum_{i=1}^{n}w_i y_i^2}\right]^{1/2} \tag{5.6}$$

Those factors represent the general according between the data (y_{obs}) and the fit (y_{calc}). But the maximum profile factor obtainable by the data is given by the expected profile factor, R_{exp}:

$$R_{exp} = 100\left[\frac{n-p}{\sum_i w_i y_i^2}\right]^{1/2} \tag{5.7}$$

So, the ratio between R_{wp} and R_{exp} is named "goodness of fit indicator", and the reduced chi-square is related to it by the relation:

$$\chi^2_v = \left[\frac{R_{wp}}{R_{exp}}\right]^2 = S^2 \tag{5.8}$$

In the present work, both the values of χ^2_v and cR_{exp} (i.e. the R_{exp} background-corrected value) for each fit are reported for completeness.

5.2.4 Vegard's law

It was 1921 when L. Vegard published his work named "Die Konstitution der Mischkristalle und die Raumffillung der Atome" [97]. More recently, Denton and Ashcroft [16] among other authors gave a more detailed description of this empirical law. The original Vegard's work has been stated for ceramics, although its main applications are found in metallurgy science.

When considering a compound with a general AB_xC_{1-x} chemical formula, a linear relationship exists between the *x* value and a general crystallographic parameter *d*. This linear relationship is commonly called "Vegard's law".

$$d = x \cdot d_{AB} + (1 - x) \cdot d_{AC} \tag{5.9}$$

If the *d* parameters of the AB and the AC compound are known, the *x* value can be easily calculated from the Rietveld refined d_{calc} parameter. In the present work, this has been achieved starting from the hydroxyapatite (*x=0*) and fluorapatite (*x=2*) *a* lattice parameters, as stated by equation 5.10.

$$x = 2 \times \frac{a_{calc} - a_{HA}}{a_{FA} - a_{HA}} \tag{5.10}$$

In the above equation, the multiplying factor takes into account that the maximum *x* value in the $Ca_{10}(PO_4)_6(OH)_{2-x}F_x$ formula can be 2.

As reported in the first part of this work, the F substitution for OH in the apatite lattice produces a more emphasized effect on the *a* lattice parameter than on the *c* one. Since the cell volume depends on the lattice parameters,[4] the 5.10 formula can be modified using the cell volume instead of *a*. In the next chapters, both the calculations will be shown, and differences in the final *x* value are discussed. It's worth to notice that the initial values of a_{HA} and a_{FA} are the ones obtained via Rietveld refinement of the $HA_{1.67}$ and $FA_{1.67}$ samples patterns, respectively (the same for *c* parameter, and thus the resulting cell volume). This is necessary because the real lattice parameters depend on the synthesis conditions, particularly on the heating temperature. As one can see by table 5.2.2, there can be a significant difference, especially on the determination of the fluorapatite *a* parameter, when considering different authors.

5.2.5 Crystallinity degree

The method suggested by Landi et al. [52] has been employed to calculate the crystallinity degree of the synthesized samples. The following formula has been used:

$$X_C \approxeq 1 - \frac{V_{112/300}}{I_{300}} \tag{5.11}$$

[4] $V = a^2c \times sin(60°)$

Reference	a [Å]		c [Å]	
	HA	**FA**	**HA**	**FA**
Web Mineral Database	9.418	9.367	6.875	6.884
Mindat Database	9.41*	9.3973	6.8782	6.88
Basar et al. [3]	9.417	-	6.879	-
Hughes et al.	9.417	9.3975	6.875	6.878
JCPDS (after Bianco et al. [6])	9.418	9.364	6.884	-

* approx. value

Table 5.2.2: The *a* and *c* lattice parameters values according to different authors

Where X_C is the crystallinity degree, $V_{112/300}$ is the intensity of the hollow between (112) and (300) reflections, which Landi and co-workers declare to completely disappear in non-crystalline samples. The agreement of the formula is given by the constance of a *K* value calculated as follows:

$$B_{002} \times \sqrt[3]{X_C} = K \tag{5.12}$$

in which B_{002} is the FWHM (°) of the (002) reflection peak. In the present work, this has been calculated through the Lorentzian fit provided by the FullProf.2k software. The *K* value reported by Landi and co-workers is 0.24 for samples with crystallinity degree below 10% (as-dried). In the present work, the degree of crystallinity is supposed be much higher because of the heat treatment performed on the samples. Thus, a new *K* value needs to be estimated.

Coherent domain size (CDS) is as well output by the software. Where not differently declared, the nominal error for this parameter is ±5nm.

5.3 High performance liquid ion-exchange chromatography

Here follows the description of the use of ion-exchange chromatography with the purpose of estimate the *x* value in the chemical formula $Ca_{10}(PO_4)_6(OH)_{2-x}F_x$. General description of the technique is given in section 2.2. Cécile Esparcieux from the ENSC of Clermont-Ferrand is gratefully acknowledged for the technical support.

While ion-exchange chromatography is a very well known technique in organic and inorganic liquid characterization, still not so much work on the use of this technique to investigate F content in HA lattice has been recorded in literature. A significant contribution comes from Zhu and co-workers [105], who studied the dissolution behavior of F-doped apatites in pure water at 25°C and 45°C with this instrument. Tredwin [94] used a similar characterization procedure to understand the influence of F doping in sol-gel derived hydroxyapatites blocks in contact with ultrapure water. Commonly, in a large part of literature (see for ex. ref. [44, 99, 83] and others), an F-selective electrode is used to dose fluorine amount in solid samples, after a complete or partial dissolution in acid medium as suggested in 1968 by Singer and Armstrong [88]. FT-IR is an interesting solution to evaluate the presence of F in the HA lattice, but it is not to be considered an easy quantitative analysis method, and it's generally supported by the F-selective electrode information. [83][84].

Usually, long time is required to have a sufficient ion release from the solid HA to evaluate it through ion-exchange chromatography, because of the product's weak solubility in neutral pH medium (from days to months). On the other side, partial dissolution of the product could be not stoichiometric, as discussed later in section 10.3. Moreover, HA, FA and intermediate FHA products can have different and unknown dissolution rates, depending not only by their chemical composition, but also by physical parameters such as specific surface or cristallinity. All of this can result in an erroneous estimation of F^- quantity compared to the PO_4^{3-} one, and thus in a significant error in the following described *x* value calculation. This is the reason why the sample needed to be always completely dissolved before being analyzed in ion chromatography. Fluoridated hydroxyapatite is supposed to dissolve with the reaction:

$$Ca_{10}(PO_4)_6(OH)_{2-x}F_x \rightarrow 10Ca^{2+} + 6PO_4^{3-} + (2-x)OH^- + xF^-$$

.

5.3.1 Technical aspects and problems

A Metrohm^{TM} 792 Basic IC instrument was used for the HPLC measurements. It was equipped with a Metrosep^{TM} Anion Dual 1 spherical shape column in hydroxyethyl-methacrylate, quaterniar ammonium groups grafted ($-R_3N^+$), code 6.1006.020, size 3x150mm. The working pH range of this column is from a minimum of 2 to a maximum of 12.

Being an anionic column, only PO_4^{3-} and F^- ions were detected, while it was not possible to calculate the amount of Ca^{2+} and Sr^{2+}. Thus, the Ca/P or (Ca+Sr)/P molar ratio was calculated from Rietveld refinement's XRD information about the molar composition of the samples.

Instrument measure range goes from 0 to 1000 $\mu S/cm$, with a nominal resolution of 0.56 $\mu S/cm$ and a maximum absolute error of $\pm 10\,\mu S/cm$ (i.e. a typical 1% relative error on measured value).

A thermostatized double steel ring detector was used, AC, 1KHz, with a working voltage of approx 1V. Cell volume is 1.5 μL and working temperature is 40$\pm$2.5°C. Since direct specific conductivity was used, no chemical suppression is necessary. Detection limits depend on the baseline status, but peaks below the 1ppm have been observed. A working flux of 0.5 mL/min has been selected, and final measurement time was found to be at least 45 mins[5].

Ultrapure water (R=18MΩ) was used throughout all the samples preparation. Eluent was prepared with 5mmol phtalic acid and buffered with 4% vol. acetonitrile. Overnight ultrasonic agitation was necessary to achieve complete dissolution of solid phtalic acid.

Sample preparation had to face the following technical problems: first of all, a strong mineral acid was required to dissolve the product in a short period of time. Then, the acid solution injected in the column must not produce chemical reactions with the eluent. For all of this, the use of a strong mineral acid, HNO_3, which led to very low pH values, was needed[6]. However, nitric acid concentration should be carefully calculated not to reach the saturation limit of the column with NO_3^- anions.

[5]This time depends on ions chemical nature and on flux speed, and it's required to completely empty the injection cell.

[6]the use of weak acids (phtalic), or acid digestion high temperature vessels did not provide good results, i.e. the digestion time was not decreased, and in many cases complete dissolution did not occur.

The pH of the dissolving solution had not to be below the lower working limit of the column (i.e. not lower than 2), thus both a dilution and a weak neutralization were needed to reach a pH slightly over 2. Neutralization had to be realized with special cares not to give chemical reactions with the solubilized species or with the eluent, nor to produce an uncontrolled increase of the pH and exceed the upper working limit of the column (i.e. over 12). Such an increase resulted when employing too concentrated or strong bases, while on the other hand a too diluted or weak basis led to a high dilution of the sample to finally reach the desired working pH.

But product dilution must be taken into account too: few levels of product (i.e. HA powders) concentration resulted in a too weak signal of the F^- peak in the chromatogram, but on the contrary, complete solubilization of HA depends on its concentration too[7]. For this reason, it was not possible to prepare very concentrated solution without using a stronger acid, and this conflicted with the first requests.

5.3.2 Sample preparation

Since no standard procedure has been reported in literature for sample preparation, after some trials and errors we stated the following method, based on compromises due to the requests specified in the previous section.

- 0.1 g of product powders (a 5 weights statistic has been used) are dissolved in a 5 mL 2M HNO_3 water solution. This corresponds to a strongly acid environment, pH≈0.14.
- The slurry is left in a silicone oil controlled temperature bath at 45°C for approx. 2h, until a totally clear solution is revealed. No stirring.
- 0.6 mL of this solution are diluted in 5 mL of eluent. The pH of this solution was approx. 1, the real value depending on the product's characteristics.
- The basification is made with the use of a diluted ammonia water solution (10% vol.), drop-by-drop added under strong magnetic stirring, until the pH reaches a value over 2. The required amount of ammonia water depends on the initial value of pH. A typical amount is 0.15 mL to reach a pH≈2.30.

[7]Saturation limit depends on environmental conditions: for our experience, a 0.1g of product in 5mL of 2M nitric acid was found to be a good compromise.

- Samples are filtered through a 0.2 μm diameter Teflon filter.

During the basic solution addition there could be an excessive local pH increase (over 5.4), which actually led to the formation of an unwanted white precipitate in the first trials. This precipitate has been purposely synthesized in higher quantity, filtered and characterized via XRD, and resulted to be ammonium nitrate (NH_4NO_3) mainly in the phase IV, called "nitrammite" (JCPDS file 8-0452), and partially in orthorhombic form (JCPDS file 43-1431) as shown by figure 5.3.1.

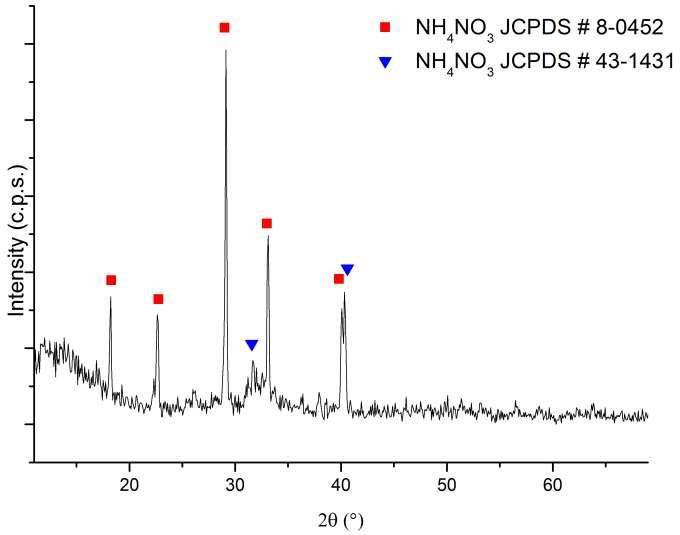

Figure 5.3.1: X-ray diffraction pattern of the product resulting from the acid digested samples basification with NH_4OH

Although the presence of this nitrate should not influence the exact measurement of PO_4^{3-} and F^- in the chromatogram, its formation is prevented by the strong agitation and the drop-by-drop adding of ammonia water.

Eluent was chosen as dilution medium because the presence of acetonitrile as buffer helped to tune the pH value without uncontrolled variations. Moreover, this avoided the formation of the system negative peak in the chromatogram.

The bath temperature was set to 45°C to increase dissolution rate, as reported by Zhu and co-workers. Since nitric acid is known to produce volume-expanding gases when

heated, higher temperatures have not been tested in the present procedure, not to damage the closed-vessel system.

5.3.3 Instrument calibration

Calibration baselines for the detected anions were obtained using NH_4F and $(NH_4)H_2PO_4$ as fluoride and phosphate precursors, respectively. Operating with nitric acid led to the detecting of a NO_3^- peak in every chromatogram. A "base" solution was prepared, containing the 0.6 mL of 2M nitric acid, with no products inside. This allowed to locate the NO_3^- peak position.

F^- content in the analyzed solutions was calculated to be below 10 ppm, depending on F-doping in HA powders, while PO_4^{3-} content was approximately 120 ppm. Thus, a total of 6 calibration solutions were realized starting from 0.6 mL of 2M nitric acid in 5 mL of eluent: 3 for fluoride anion, whose concentration were set to 2, 5, 10 ppm and 3 for phosphate anion with 70, 120, 150 ppm concentration; a peak-height calibration was chosen instead of the peak-area one, in order to minimize the errors due to a non-linear baseline.

Indeed, at the working conditions, the F^- peak appears very close to the cation release system peak, and the baseline is affected by the previous fluctuation. A slight error in the peak baseline determination could result in a bigger error when considering the area calibration than when considering just the height-weighted one.

Since the exact position of each peak depends on weak fluctuations of pH value from sample to sample, the peak baseline was set independently for every chromatogram, and no standard baseline limits are fixed. To take into account possible errors due to peak position, baseline determination, instrument precision, etc., some repeatability tests have been made (see after), and a standard relative error of 5% on the final x value has been determined.

Figure 5.3.2 shows the chromatograms of the F^--containing and PO_4^{3-}-containing standards for the instrument calibration.

As a matter of fact, the F^- retention peak appears at about 280 seconds (i.e. 4.6 minutes), F^- being a very small and weakly charged anion. PO_4^{3-} peak appears at about 430 seconds (7.1 min). Since the "base" solution allows to set the NO_3^- peak at about 625 seconds (10.40 min), there should be an evolution of PO_4^{3-} ions: in fact, bigger and more charged ions are normally released later by the column, thus they usually show the spe-

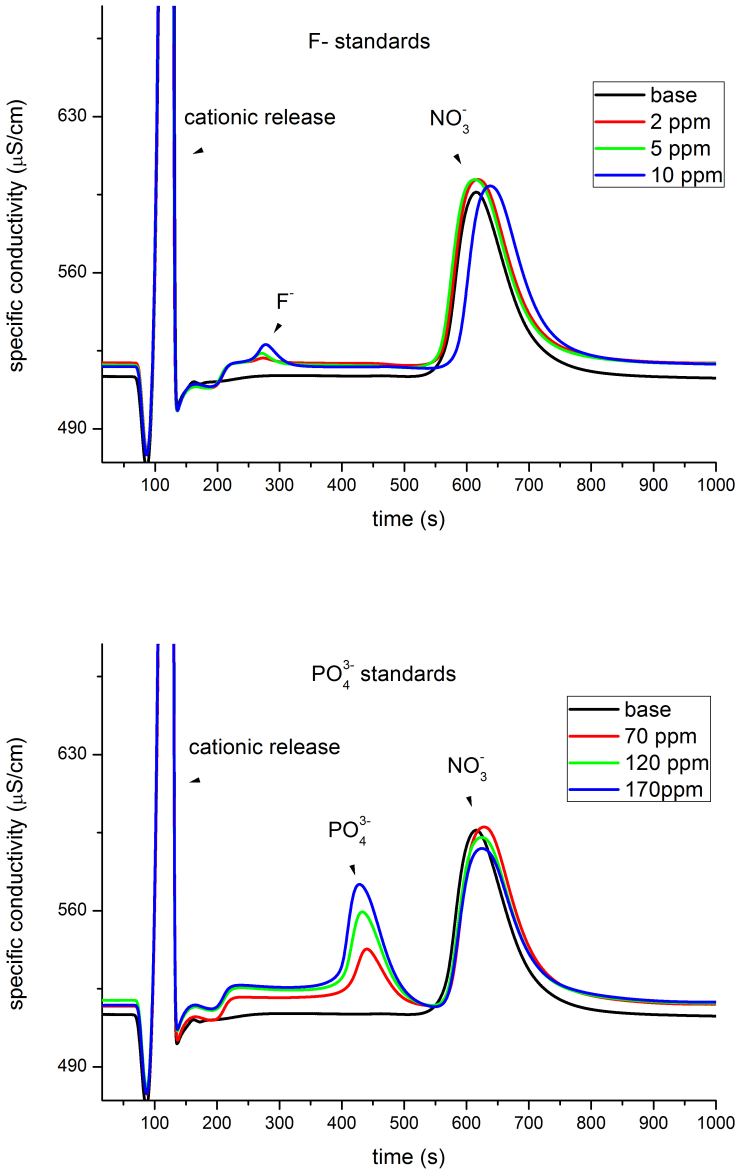

Figure 5.3.2: F^- (up) and PO_4^{3-} (down) standards for IC instrument calibration

cific conductivity increase peak at longer time values. On the contrary, NO_3^- is surely both smaller and less charged than PO_4^{3-}. But at very low pH values, phosphate equilibrium passes through several forms, as demonstrated by Beukenkamp and co-workers [5]. Hy-

drogenphosphates could have an improved ionic mobility due to a lower charge. Even if it's not possible to state the exact form of phosphate, the present direct method can definitely give a reasonable dosage of this ion amount in the solutions.

Nominal values of F^- and PO_4^{3-} amounts in the standard solutions have been recalculated to fit the best interpolation, as showed in eq. 5.13, in which W is the matter amount (PPM), R is the specific conductivity signal, and K_i are fitting paramaters. The Metrosep^{TM} software provides a simple relation, with $K_2 = 0$, whose details are shown in table 5.3.1.

$$W(R) = K_2R^2 + K_1R + K_0 \tag{5.13}$$

F^-					
calibration level	**peak height** $[\mu S/cm]$	**peak area** $[(\mu S/cm)^2]$	**ion concentration [ppm]**	**correlation factor***	**RDS**
1	1.945	59.83	2.0311	**0.999764**	**4.900%**
2	4.458	134.6	5.0224		
3	8.284	280.5	9.9581		

PO_4^{3-}					
calibration level	**peak height** $[\mu S/cm]$	**peak area** $[(\mu S/cm)^2]$	**ion concentration [ppm]**	**correlation factor***	**RDS**
1	22.61	1468	69.827	**0.996557**	**6.103%**
2	38.65	2490	123.84		
3	49.23	3443	171.73		

*referred to peak height curve

Table 5.3.1: Calibration curves for F^- and PO_4^{3-}

5.3.4 Estimation of the *x* value in the $\mathbf{Ca_{10}(PO_4)_6(OH)_{2-x}F_x}$

As stated before, fluoridated hydroxyapatite is supposed to dissolve according to the following reaction:

$$Ca_{10}(PO_4)_6(OH)_{2-x}F_x \rightarrow 10Ca^{2+} + 6PO_4^{3-} + (2-x)OH^- + xF^- \tag{5.14}$$

Through ion-exchange chromatography, it's possible to calculate the mass concentration both of PO_4^{3-} and F^- ions in the analyzed solution, in parts per million (ppm). The medium density has been considered as the water one (a very negligible error is introduce in the following calculations), so the conversion from mass concentration to molar one becomes simpler[8].

Every mole of hydroxyapatite, when dissolved, provides 6 moles of PO_4^{3-} and x moles of F^-. Throughout the dosage of the phosphate groups, one can calculate the amount of apatite moles in the analyzed aliquot. Then, the simple relation $x = \frac{moles\ of\ F}{moles\ of\ FHA} = \frac{moles\ of\ F^-}{6 \times moles\ of\ PO_4^{3-}}$ was employed to find *x*.

When phases other than apatite are present in the product, the true molar concentration of apatite phase is calculated from Rietveld refinement mass composition, and introduced in the previous equation. In fact, Fluoride is supposed not to be hosted in crystal lattices different from the apatite one, such as α- or β-TCP, but those products provide a non negligible amount of PO_4^{3-} in the analyzed solution (see reaction 5.15): thus, if the above uncorrected equation is simply used, an underestimation of the *x* value could result. That's why the previous relation has been corrected.

$$Ca_3(PO_4)_2 \rightarrow 3Ca^{2+} + 2PO_4^{3-} \tag{5.15}$$

To estimate a mean relative error, which as a matter of fact resulted to be more incident when weak F^- signals are reported then with high ones, repeatability tests have been performed and a final RDS=5% error on the *x* value has been considered. Results of these tests are shown in figure 5.3.3.

[8]By definition, 1ppm=1part/10^6parts. E.g. 1ppm=1g/10^6g=1mg/1kg=1mg/L when density=1000g/L (water). Thus, molar concentration is given by the relation $[C]_{molar}$=$[C]_{mass,\ ppm}$/1000*M, where M is the molar weight of the ion (expressed in g/mol).

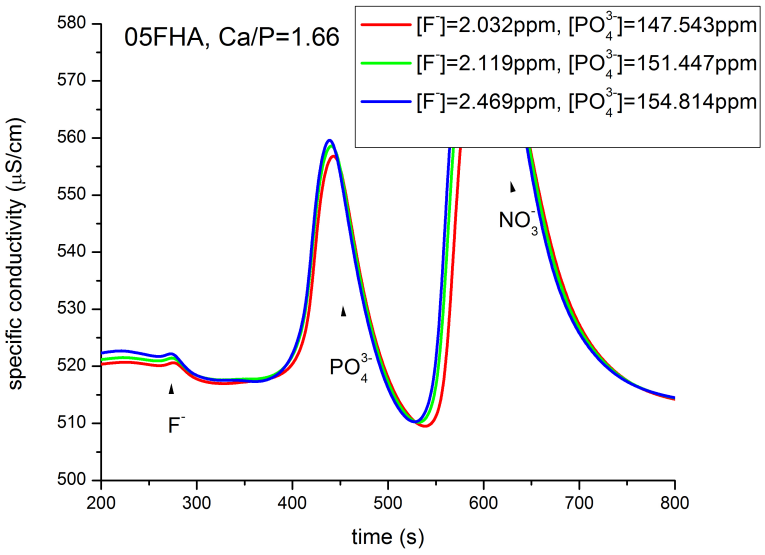

Figure 5.3.3: Repeatability tests on ion chromatography

5.3.5 Phosphate and fluoride release in acid medium studies: experimental set-up

To assess the influence of F and Sr doping of the release of anions in acid conditions, dissolution studies have been performed. A 0.1 g amount of product is dissolved according to the standard procedure in 5 mL of 2M nitric acid. After a period of 10, 40 and 80 minutes, a 0.6 mL aliquot of solution has been carefully collected[9], diluted in 5 mL of eluent solution, and slightly basified through ammonia water as reported before. Phosphate and fluoride content of the solutions are recorded and reported against the solid product immersion time. Different samples were realized for every time interval, not to influence with dilution effects both the real content of the solution, and the dissolution rate of the product. The last point on the further reported diagrams refers to the complete dissolution, which was reached in different time intervals according to the product's composition, and it was conventionally set to 150 mins in the graphics (see chapter 10).

[9]This aliquot has been taken from the upper part of the solution not to collect undissolved solid particles. It was taken into account that in absence of stirring a non-homogeneous concentration could result in the medium. However, the aliquot of solution is enough to minimize this error, and if the standard procedure is adopted, this systematic error becomes negligible.

The dissolution behavior of hydroxy- and fluorapatite in strong acid media is not fully described in literature. Moreover, we are fully aware that this kind of acid environment is not at all common in the biological applications in which hydroxyapatite and fluorapatite are normally employed. Anyway, this procedure allowed us to have a general view all over the synthesized products dissolution behavior in a short period of time, although more detailed and long-immersion period tests should be performed. But apatites are employed not just in biomedical applications; indeed, a huge work has been recently made to use hydroxyapatite as ion chromatography column material. Thus, as a structural characterization is needed, it seemed necessary to understand the reactions occurring on this material even in very strong acid medium, through accelerated tests as described above.

Samples with Ca/P=1.67 and x=0, 1 and 2 (i.e. $HA_{1.67}$, $1FHA_{1.67}$ and $FA_{1.67}$) have been studied through the above described technique. Finally, the 05Sr2F sample has been characterized in order to assess the influence of a slight content of Sr in the lattice on the dissolution properties. The specific surface of each sample has been recorded as stated in the following section. Those samples showed a controllable dissolution rate, i.e. they came to complete dissolution in about 150 minutes, while other samples, particularly those with a high TCP content, are much more soluble and the anionic concentration monitoring resulted to be difficult. We underline that no stirring is applied during the immersion period. Even if during the aliquot uptaking the container is weakly shaken, we estimated that such an agitation can be negligible with those samples which show a quite low dissolution rate.

5.4 BET Surface Area measurements

A Quantachrome Autosorb-1^{TM} instrument was used for the specific area measurements of the powdered samples (see figure 5.4.1). A general description of this technique is given in section 2.3.

The instrument is equipped with two heated degassers and one cold-trap (not used). A 6 mm diameter cell was used for all measurements. The complete degas of each sample was performed overnight (typically, from 15 to 17 hours) at 120°C immediately before every measure. The weight of analyzed powders was accurately evaluated through an average over 8 measured values. Nitrogen was used both as adsorbate gas and as analysis one. The bath temperature of liquid N_2 is 77.30 K (-195.85°C) and the divergence from the ideality was estimated to be $6.58 \times 10^{-5}\%$. Molecular section was set to 16.2 $Å^2/molec$ as

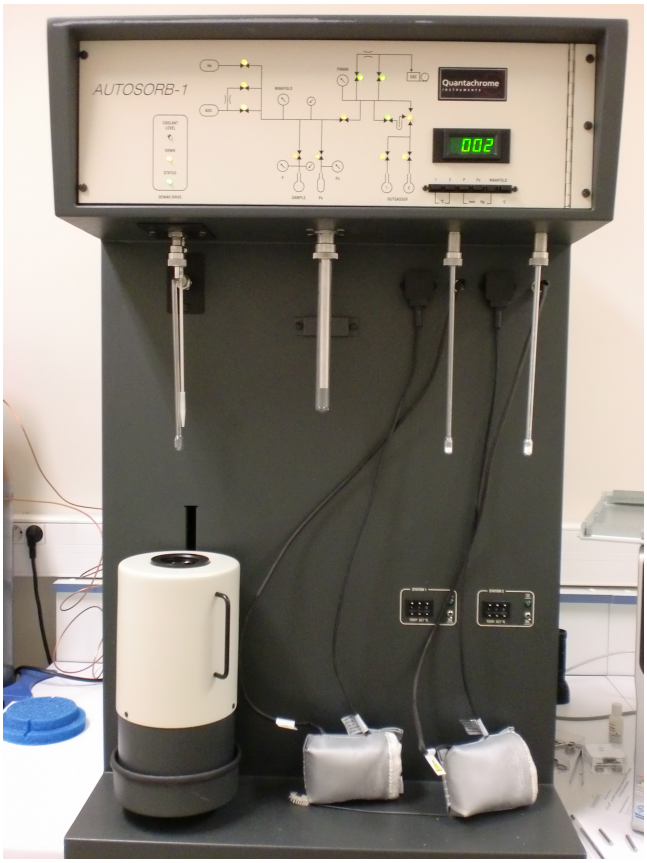

Figure 5.4.1: The Autosorb-1 Quantachrome instrument used for the BET specific surface analysis.

indicated by the literature (see section 2.3).

Through the observation of the adsorption/desorption isotherms of the pure hydroxyapatite sample before and after calcination, one can observe that the 900°C heating eliminates all the accidental porosity, thus a faster 7-point adsorption method was adopted to calculate the specific surface area of all the samples. Results of these measurements are reported in figure 5.4.2.

For all the labelled samples, the linear correlation factor for the adsorption 7-point BET plots, i.e. the BET function vs P/P_0, has been noted and resulted to be always acceptable, being very close to the unity. In all the following tables, it will be reported as "R^2". See figure 5.4.3 for reference.

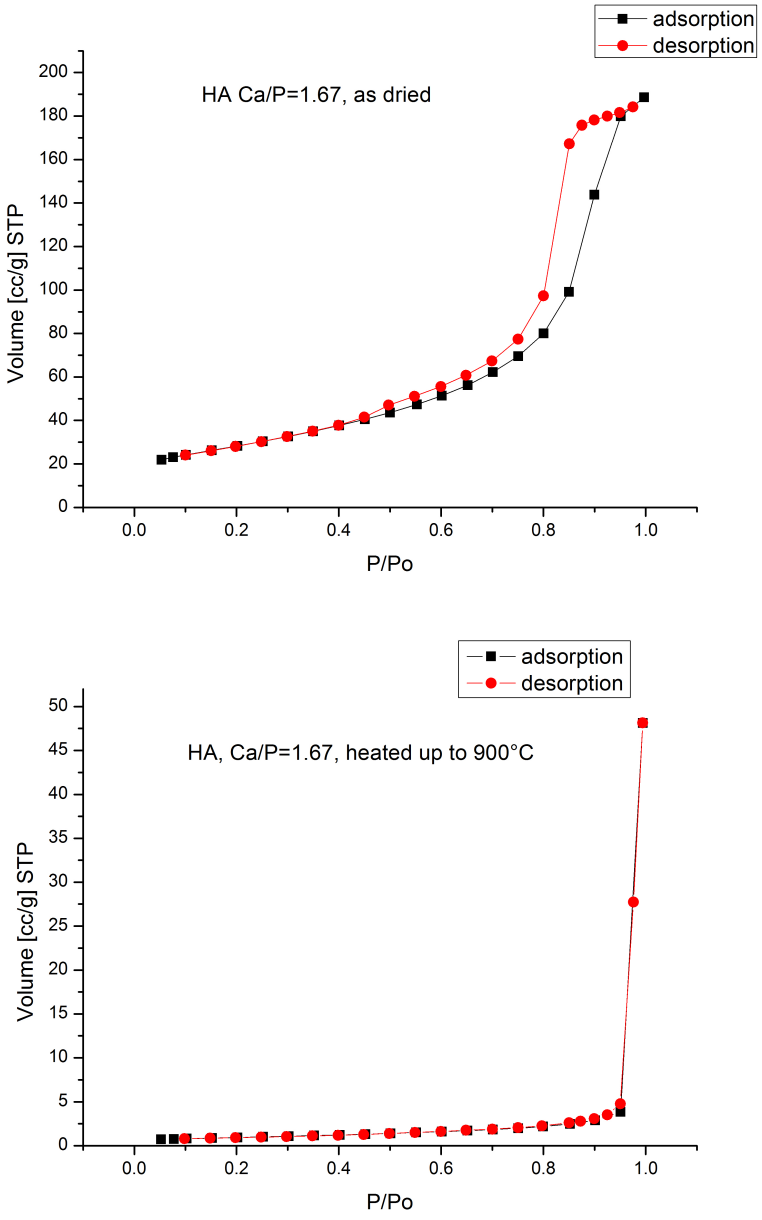

Figure 5.4.2: BET isotherms of as-dried and calcined HA powdered samples

5.5 Weight loss upon calcination

Bianco and co-workers [6] and other authors suggest that the introduction of an F^- ion in the hydroxyapatite lattice can result in higher thermal stability, i.e. the decomposition

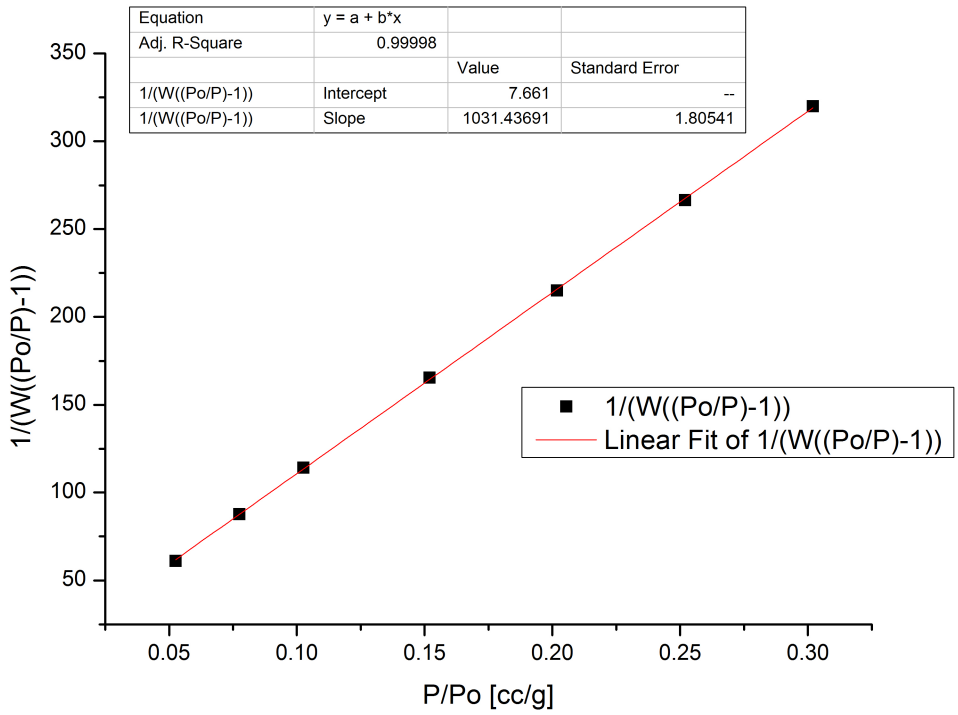

Figure 5.4.3: BET plot for the HA Ca/P=1.67 powders

temperature is shifted over 1300°C. Sintering abilities and grain growth of F-doped hydroxyapatite have been also studied by Rodriguez-Lorenzo and Gross in more than one work [85, 33, 35].

A quick evaluation of the thermal stability of our samples has been attempted in order to verify if the improvement of it through the incorporation of fluoride. No sintering studies have been performed, but an accurate determination of the product's weight before and after calcination at T=900°C, and the simple relation

$$wl\% = \frac{m_{b.c.} - m_{a.c.}}{m_{b.c.}}$$

has been used to calculate the percentage weight loss, which has been plotted against the F content in the product. In the formula, *wl* stands for weight loss, and $m_{b.c.}$ and $m_{a.c.}$ for the sample's mass before and after calcination, respectively. An overestimation of 10% of the related error has been applied.

Part III

Results and discussion

Chapter 6

Ca/P=1.67 FHA set

The reader should be aware that from now on, the term “apatite” is used to refer to any kind of apatite structure, even if containing F atoms, Sr atoms, or both. Different set of samples are named “FHA$_n$” or “Ca/P=n FHA powders”, indifferently.

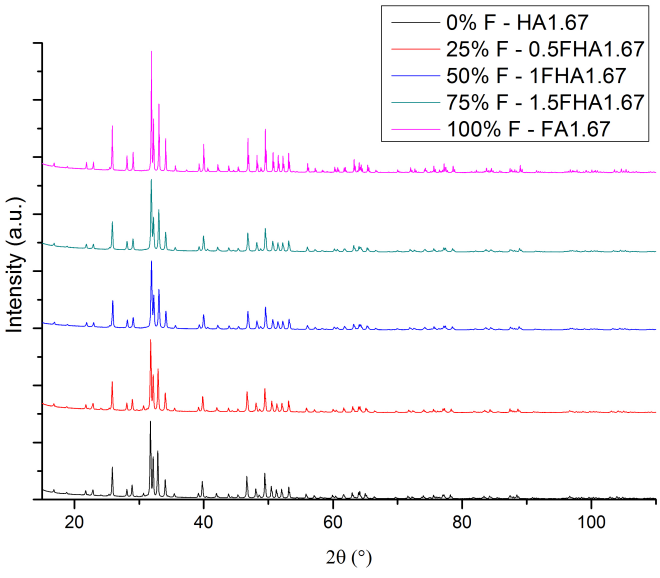

Figure 6.0.1: XRD patterns of the Ca/P=1.67 FHA set

6.1 XRD characterization and Rietveld Refinement

The first series to be characterized was the one with nominal Ca/P molar ratio equal to 1.67. The resulting XRD patterns are shown in figure 6.0.1. As explained before, hydroxyapatite and fluorapatite share the same unit cell, with slight differences related to lattice parameters. Reflection peaks of the two phases are then set at very similar 2θ positions, and very accurate data are required to seize the difference between the two of them. In the cited figure, the atomic substitution percentage is labelled on the legend.

Rietveld refinement has been performed as reported in the 5.2 section. An example of the final results, in the case of the $HA_{1.67}$ sample, is reported in figure 6.1.1. As one can see, a good fit is achieved after the refinement of all the parameters cited above. This quality has been reached with all the samples data set. The 6.1.1 table shows the values of the χ^2 and background-corrected expected conventional R factor registered for every sample.

Sample label	$\mathbf{cR}_{exp}$	$\boldsymbol{\chi^2}$
$\mathbf{HA}_{1.67}$	3.02	6.55
$\mathbf{0.5FHA}_{1.67}$	2.72	6.22
$\mathbf{1FHA}_{1.67}$	2.74	4.78
$\mathbf{1.5FHA}_{1.67}$	2.62	3.99
$\mathbf{FA}_{1.67}$	2.58	16.5

Table 6.1.1: Agreement factors of the $FHA_{1.67}$set

The whole set of XRD patterns reports the characteristic peaks of hydroxyapatite (JCPDS file #09-0432), shifting to the ones of fluorapatite (JCPDS file #15-0876) as the F content increases. This shift is the first evidence that a phase transformation occurs when F^- ions are introduced in the HA lattice; the displacement of the (211) main reflection peak position when considering the nominal F content in the product is reported in figure 6.1.2 (instrumental zero-shift has been previously subtracted after being accurately calculated through the Rietveld refinement technique).

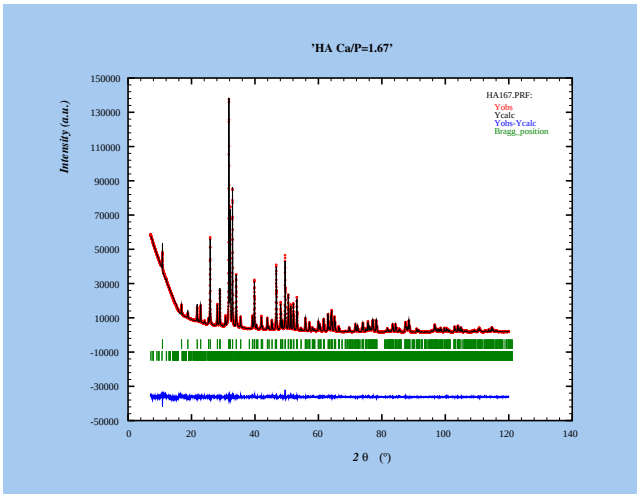

Figure 6.1.1: The FullProf.2k resulting plot after Rietveld refinement of the $HA_{1.67}$ sample and the agreement factors of the $FHA_{1.67}$ Rietveld fitting set

Sample label	Fluoride content, nominal (x)	(211) 2θ refined peak position [°]	Reference (JCPDS)
$HA_{1.67}$	**0**	31.776	31.772
0.5$FHA_{1.67}$	**0.5668**	31.822	
1$FHA_{1.67}$	**1.01508**	31.85	
1.5$FHA_{1.67}$	**1.50293**	31.886	
$FA_{1.67}$	**2**	31.913	31.937

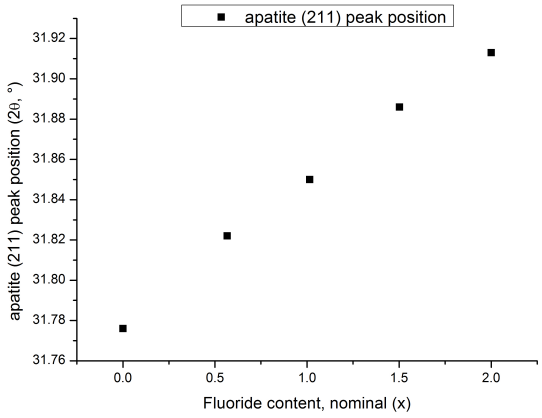

Figure 6.1.2: Apatite (211) reflection peak position VS F content in the product

6.2 Secondary phases

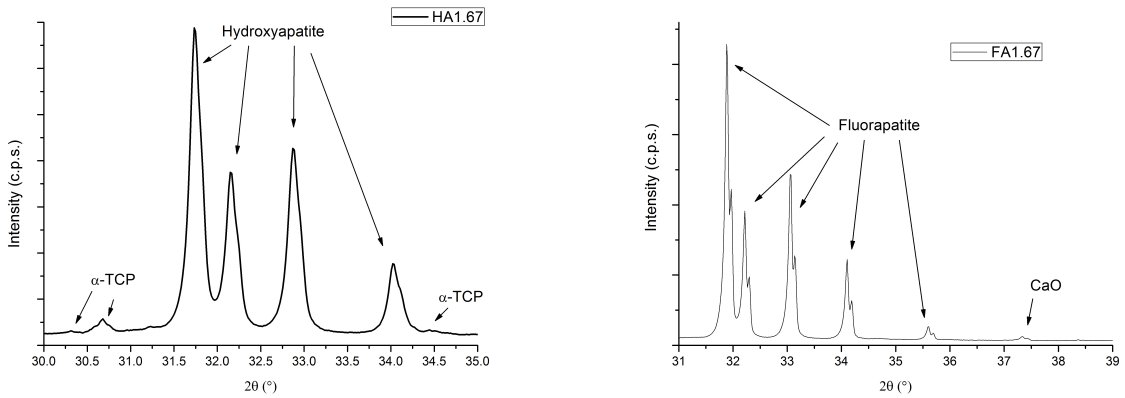

Figure 6.2.1: Zoomed XRD patterns for HA (left) and FA (right) powders containing minor amounts of α-TCP and CaO, respectively

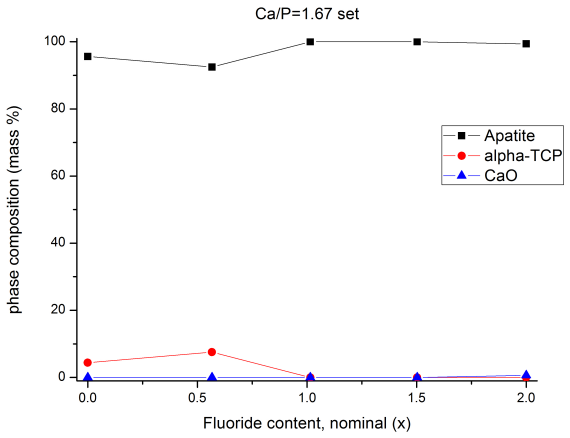

Figure 6.2.2: Phase composition vs fluorine content of the Ca/P=1.67 set

Although the nominal Ca/P ratio was chosen to obtain a final product constituted of pure apatite phase (whether hydroxyapatite or fluorapatite), a slight amount of secondary phase has been detected in some samples; more precisely in the first two samples of the set (i.e. $HA_{1.67}$ and $0.5FHA_{1.67}$) a little amount of $\alpha-$TCP (JCPDS file #29-0359) has been

found[1], while in the fluorapatite sample ($FA_{1.67}$) the presence of lime has been recorded (JCPDS #37-1497). α-TCP exhibits monoclinic crystal system, $P2_1/a$ space group, with the following lattice parameters: *a*=12.89, *b*=27.28, *c*=15.22 Å, $\alpha = \gamma = 90°$, β=126.2°. This phase stability temperature is normally above 1125°C, thus the formation at T=900°C is not common; this presence is probably due to the high pH values reached in the ageing step, as reported by Li and co-workers, who used a similar precipitation process to obtain biphasic α/β-TCP [58]. They suggest that the amorphous Ca phosphate in the aged synthesis solution can evolute in α-TCP when pH value is close to 12, even with a 800°C calcination.

CaO has a simple cubic $Fm\bar{3}m$ unit cell, with *a*=*b*=*c*=4.81Åand $\alpha = \beta = \gamma$=90°. Lime is sometimes found in the Ca phosphate powders as impurity. For a discussion about this phase presence in the $FA_{1.67}$ sample, see next session.

Only the main peaks of these phases are easily recognizable, corresponding to the (034) reflection at 2θ=30.7° for the α-TCP and to the (200) reflection at 2θ=37.4° for the CaO. The zoomed XRD patterns for $HA_{1.67}$ and $FA_{1.67}$ show in details these peaks (figure 6.2.1). The evolution of phase composition of the final product when considering the increasing of F content in the synthesis solution is shown in figure 6.2.2. $1FHA_{1.67}$ and $1.5FHA_{1.67}$ samples seem to be composed only by fluoridated hydroxyapatite. Maximum recorded uncertainty is 0.3 %.

6.3 Estimation of the Ca/P molar ratio

The presence of phases other than apatite must of course influence the final Ca/P ratio: hence from the mass fraction of the powders given by the Rietveld refinement, the molar composition of the samples has been calculated. Then, the Ca/P ratio has been recalculated according to this simple relation: $R = (\sum_i y_i \times n_{Ca})/(\sum_i y_i \times n_P)$, in which R represents the Ca/P molar ratio of the product, y_i is the molar fraction of the *i* phase, n_{Ca} and n_P are the number of Ca and P atoms in the chemical formula of the *i* phase, respectively. Because the conversion from the mass fraction to the molar fraction requires the molar weight of each phase, it's worth to notice that this latter depends on the Fluorine content according to the following relation: $MW_{xFHA} = MW_{HA} - xMW_{OH} + xMW_F$. Since

[1] this corresponds to a mass percentage of 4.38 and 7.53% for $HA_{1.67}$ and $0.5FHA_{1.67}$ samples, respectively

the molecular weight of the fluorine (18.99840 amu) is slightly higher than the hydroxil group one (15.99994+1.00794=17.00788 amu), the final weight of the apatite increases with the increasing of the fluorine content, and this has been taken into account when calculating the apatite molar fraction of each product, supposing that the x value should not be significantly different from the nominal one, and that the fluorine would not be hosted in phases different from the apatite. The detailed Ca/P values are reported in table 6.3.1.

Sample label	Fluoride content, nominal (x)	Secondary phase	secondary phase mass fraction (%)	apatite molar fraction	Estimated Ca/P molar ratio
HA$_{1.67}$	0	a-TCP	4.38	0.871	**1.6588**
0.5FHA$_{1.67}$	0.5668	a-TCP	7.53	0.791	**1.6531**
1FHA$_{1.67}$	1.01508	-	0	1	**1.6667**
1.5FHA$_{1.67}$	1.50293	-	0	1	**1.6667**
FA$_{1.67}$	2	Lime	0.64	0.896	**1.7246**

Table 6.3.1: Estimated Ca/P ratios for the FHA$_{1.67}$ set

As one can see, the final Ca/P values are quite consistent with the ones necessary to obtain hydroxyapatite as final product. An eventual reagent loss is always possible when considering the synthesis procedure, but still the values can be considered very close to the desired ones. Moreover, as showed in the first part of this work, hydroxyapatite can crystallize in several Ca-deficient forms. It's worth to notice that from a 50% atomic substitution (1FHA$_{1.67}$), the TCP phase is no more stable, and only fluoro-hydroxyapatite appears. The presence of CaO in the FA$_{1.67}$ sample can be referred to the ion substitution as explained in section 4.5. When the complete F substitution is achieved, a larger number of OH^- groups is released in the solution, thus the formation of $Ca(OH)_2$ is promoted still in the slurry, and this is transformed in CaO when heated up to 900°C[2]. The Ca atoms necessary for this phase formation can be reasonably taken from the apatite, and so a Ca-deficient apatite is supposed to form again. If this is true, the final Ca/P ratio should get close to the nominal 1.67, and not to the calculated 1.72. A more precise Ca and P-dosage technique should be used to assess the goodness of this hypothesis (e.g. ICP-AES). It was

[2]825°C is reported as the $Ca(OH)_2 \rightarrow CaO$ calcination temperature.

not possible to confirm this conclusion with the Rietveld refinement technique, because the refinement of the Ca atoms occupancy factors in the apatite lattice did not lead the fitting to convergence.

6.4 Lattice parameters and refined structure

Sample label	a [Å]	c [Å]	cell volume [Å^3]
HA$_{1.67}$	9.41954	6.88067	528.714
0.5FHA$_{1.67}$	9.40322	6.88211	526.994
1FHA$_{1.67}$	9.39288	6.88554	526.097
1.5FHA$_{1.67}$	9.38071	6.88439	524.647
FA$_{1.67}$	9.37141	6.88445	523.620

Table 6.4.1: The apatite phase refined parameters of the FHA$_{1.67}$ samples set

Table 6.4.1 shows the apatite phase refined parameters. For both *a* and *c*, the maximum absolute error is 3×10^{-5}Å, and for the cell volume, it's 4×10^{-3}Å. The cell volume results automatically from the software output, and it's calculated by the formula: $V = a^2 c \times sin(60°)$. Figure 6.4.1 shows the dependence of the *a* parameter and *c* parameter on the nominal F content in the product, expressed as *x*. As one can see, there's a clear linear trend for the *a* parameter and for the cell volume too to decrease as the F content increases, in perfect accord with the Vegard's law; but no linear correlation exists between *c* and *x* . The correlation factors of the linear fit of the calculated *a* data and cell volume data are respectively 0.99272 and 0.99372. This suggests that both linear correlations are good enough, and both can be afterwards used for the determination of the *x* value as explained in section 5.2.4.

The explanation of this phenomenon lies in the hexagonal structure represented in figure 6.4.2. The OH group is set in the O4 4e site, with x=y=0, and z value varying from 0.197 (HA$_{1.67}$sample) to 0.227 (FA$_{1.67}$ sample)[3]. When an ionic radius contraction is considered, i.e. when F^- replaces the OH^- group, one could suppose that a simple *c* axis contraction results. But as the lower part of figure 6.4.2 shows, the Ca1 sites are aligned along the *c* axis, so such a contraction is not possible. On the other hand, no hurdle is put up for an *a* axis contraction, because enough space is left to the PO_4 groups to slide along this axis towards the Ca2 site. The above introduced results match perfectly this description.

[3]Approximated values. However, FullProf.2k software indicates a maximum uncertainty of 6×10^{-6}.

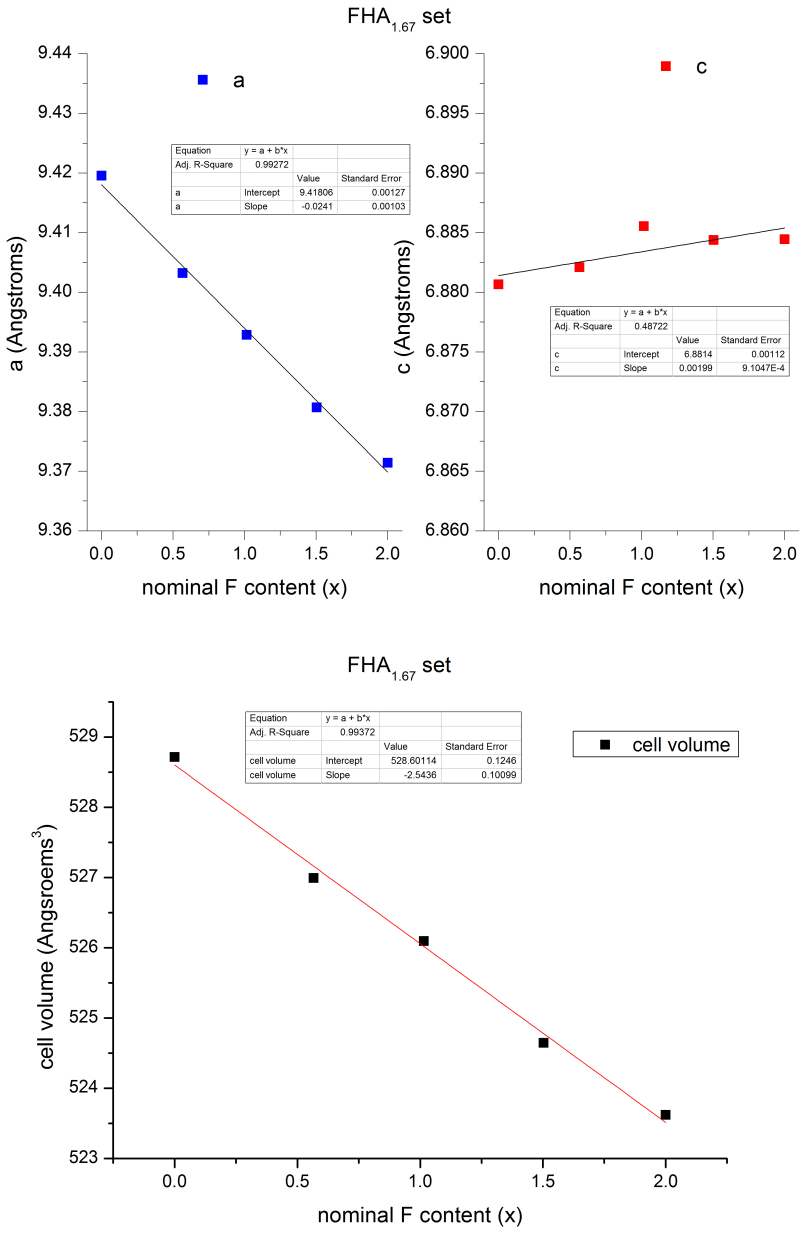

Figure 6.4.1: The *a*, *c*, (up) and cell volume (down) refined parameters of the $FHA_{1.67}$ set vs fluorine nominal content of the sample

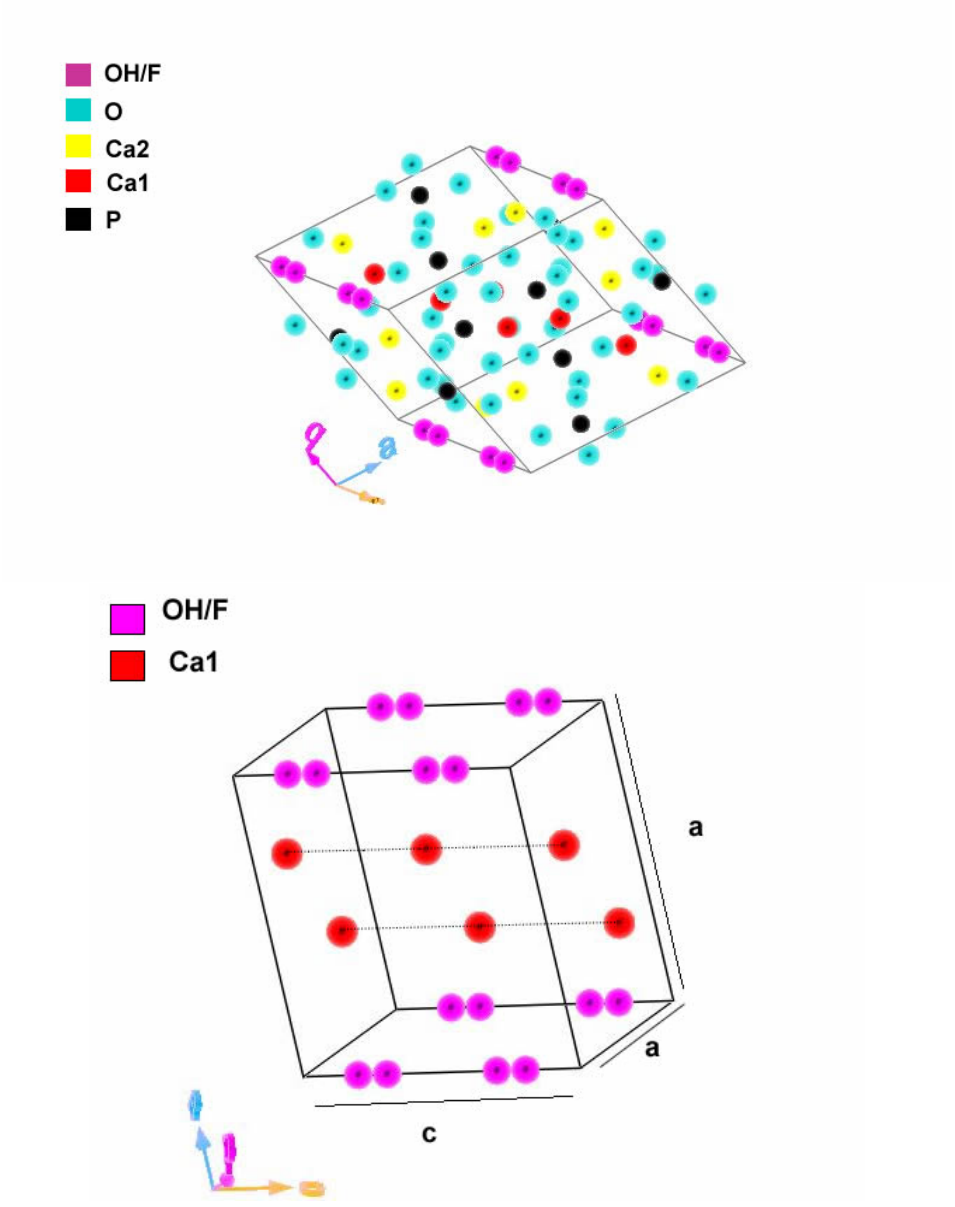

Figure 6.4.2: Apatite unit cell structure, provided by FpStudio ver-1.0. UP: the complete unit cell structure, DOWN: simplified structure showing only Ca1 and O4 sites

6.5 Determination of the *x* value

The *x* value in the $Ca_{10}(PO_4)_6(OH)_{2-x}F_x$ formula has been determined according to the two different methods stated in chapter 2: linear regression from the Vegard's law and

ion-exchange chromatography.

As stated before, the linear regression can be performed using the *a* parameter or the cell volume parameter. In both cases, the starting values are the refined ones (see section 5.2.4 for details).

Ion-exchange chromatograms of the Ca/P=1.67 series dissolved products are reported in figure 6.5.1, with detailed F^- and PO_4^{3-} calculated amounts given in the inset table.

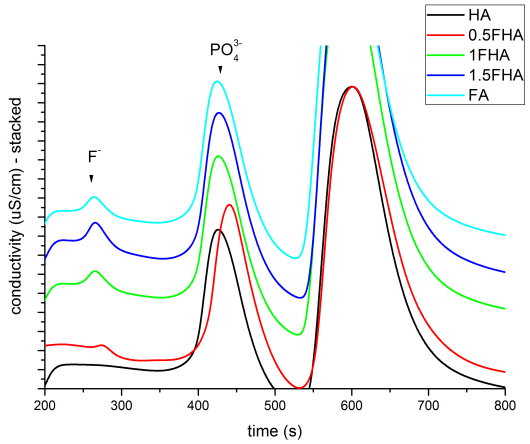

Sample label	F (ppm)	PO_4^{3-} (ppm)
HA$_{1.67}$	0	139.087
0.5FHA$_{1.67}$	2.207	151.268
1FHA$_{1.67}$	5.163	139.764
1.5FHA$_{1.67}$	7.156	143.243
FA$_{1.67}$	8.475	123.182

Figure 6.5.1: Chromatograms of the FHA$_{1.67}$ set

The three calculated *x* values are summarized in figure 6.5.2and the inset table. Error bars are to be referred to the ion chromatography determined values[4], while errors in the Rietveld refinement determination both on the *a* and on the cell volume parameter were too small to be plotted. It's worth to notice that a general good agreement between the nominal *x* values and the determined ones is observed, obtained whether through the first or the second method. The shift from perfect linearity does not show a systematic trend,

[4] 5% of the total value, see section 5.3.4

i.e. it seems that not over- or underestimation is given by both the methods. The first and last point obtained with the Vegard's law linear regression are obviously set to 0 and 2. The $FA_{1.67}$ *x* value is a little higher than the maximum allowed, i.e. 2, but it is consistent with the relative error. The most important mismatch between the values obtained from the two methods is given by sample $0.5FHA_{1.67}$ and this could be most likely explainable by the difficulty to achieve good data from the ion chromatography when low F^- content is registered. The present results confirm the works published by Bianco and co-workers [6], Rodriguez-Lorenzo [85]and others.

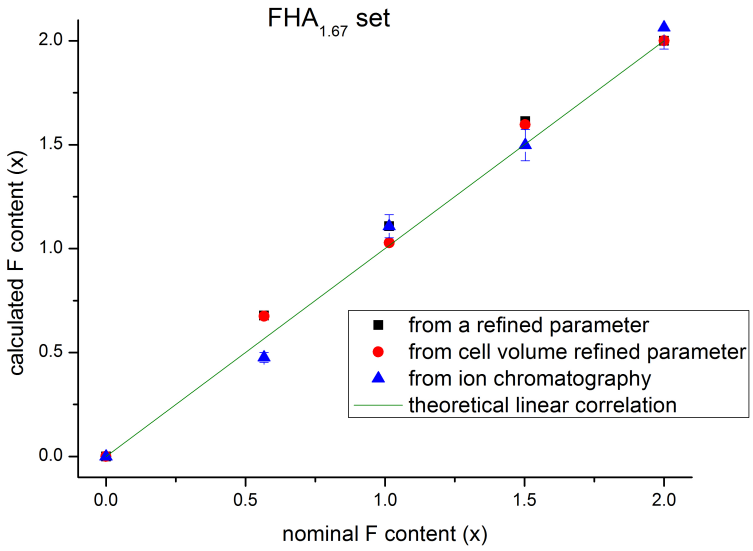

Sample label	nominal *x*	*x* from Vegard's law, *a* parameter	*x* from Vegard's law, *cell volume* parameter	*x* from ion chromatography
$HA_{1.67}$	0	0	0	0
$0.5FHA_{1.67}$	0.56680	0.67816	0.67530	0.47613
$1FHA_{1.67}$	1.01508	1.10783	1.02748	1.10788
$1.5FHA_{1.67}$	1.50293	1.61355	1.59678	1.49824
$FA_{1.67}$	2	2	2	2.06337

Figure 6.5.2: The *x* value in the FHA formula calculated through Vegard's linear regression of *a* lattice parameter, cell volume, or through ion-exchange chromatography, $FHA_{1.67}$ set

6.6 Coherent domain size, surface area, weight loss upon calcination

The FullProf.2k software provides important microstructural parameters, such as the mean coherent domain size of the sample, as reported in section 5.2. This parameter has been correlated to the specific surface area calculated by the BET method, and results are shown in figure 6.6.1 and in the inset table. For the domain size, the absolute error is $\pm$5nm, while for the specific surface area it is ± 0.1 m^2/g.

Fluorine is known for increasing the mean crystallite size in F-doped hydroxyapatite samples. However, the coherent domain size did not augment significantly in our samples when considering higher F-doping, but on the contrary a slight non-linear decrease is shown, except for the almost-pure Fluorapatite sample, which reports a mean coherent size much larger than the other ones. This means that the microstucture is deeply different from other samples, probably due to the role of F; as reported and documented by Gross and Rodriguez-Lorenzo [33], in the densification during solid state sintering at least two mechanisms are involved, i.e. the lattice and the grain boundary diffusion. We can refer the same mechanisms in the grain growth, the lattice diffusion being the slowest mechanism. The anions positioned in the outer part of the hexagonal lattice of the apatite are mainly F^- or OH^-, and the energy required for migration is greater in the case of OH^-; by the way, $OH\cdots F$ weak interactions can be the cause of a decrease of the mobility of both the species, and so a decrease in the overall diffusion. Our interpretation is that the presence of *only* F^- ions led to a simple augmentation of the overall diffusion, and thus a general increase in the coherent domain size after calcination, i.e. in the grain size[5]. This increase is found only in the fluorapatite-containing sample, while the others FHA samples suffer from the $OH\cdots F$ interaction.

In the same work, Gross and Rodriguez-Lorenzo found out that a higher SSA is recorded in the most containing fluorine samples, as result of the difficulty of the apatite lattice to host both OH and F atoms, that leads to a preferential growth in the c-axis direction. But the overall value of the SSA depends also from the milling procedure. Although a general correlation exists in non-porous materials between the grain size and the SSA, our data show that a general SSA decrease is recorded in the samples with the higher content of

[5] i.e. Fluorapatite has a lower activation energy barrier for grain growth than hydroxyapatite, as reported by Gross and Rodriguez-Lorenzo

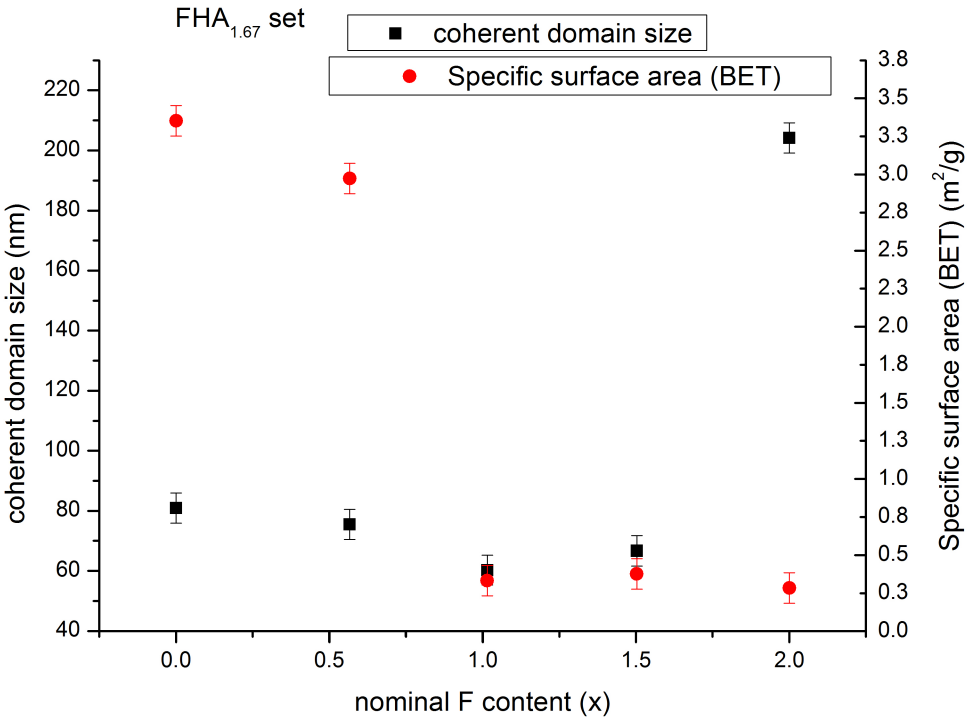

Sample label	Coherent domain size [nm]	Specific surface area [m^2/g]
HA$_{1.67}$	81	3.352
0.5FHA$_{1.67}$	76	2.974
1FHA$_{1.67}$	60	0.3328
1.5FHA$_{1.67}$	67	0.3767
FA$_{1.67}$	204	0.2838

Figure 6.6.1: Coherent domain size and specific surface area of the Ca/P=1.67 set

fluorine; but no obvious dependence is revealed between SSA and grain size. However, the low SSA values do not allow us to recognize a significant trend in these data. What it's worth to say is that a general compact structure is found, and no important porosity origins from the synthesis method. Gross and Bhadang [35] proved that the mechanical properties of sintered blends of hydroxyapatite/fluorapatite have a general improvements

as the F content increase. Particularly, the *fracture toughness* parameter shows an important increase in the case of high fluorine content. When considering manual grinding, it could happen that this resistance to fracture leads to the formation of bigger particles. Because, in non-porous samples (i.e. when SSA values are generally low), the particle size play a very important role in determining the final SSA, one could infer that 1FHA$_{1.67}$, 1.5FHA$_{1.67}$ and FA$_{1.67}$ samples particles are slightly bigger than the others. More precisely, the FA$_{1.67}$ sample behaves differently, because in Gross and Bhadang work, pure FA shows a *decrease* of K_{IC}.

Since the reducing of the cell volume causes also an higher thermal stability (see the first part of this work for details), relative weight loss before and after the 900°C heating has been plotted against the nominal F content in the product. This value includes the weight loss caused to the residual solvent evaporating and the eventual presence of nitrates from the synthesis method. Figure 6.6.2 shows a general decrease of the relative weight loss when considering the increase of the F content, with the exception of the weakest F-doping (FHA$_{1.67}$). The red line is added as guide for the eye. Further TGA/DTA analysis should be performed to confirm this trend.

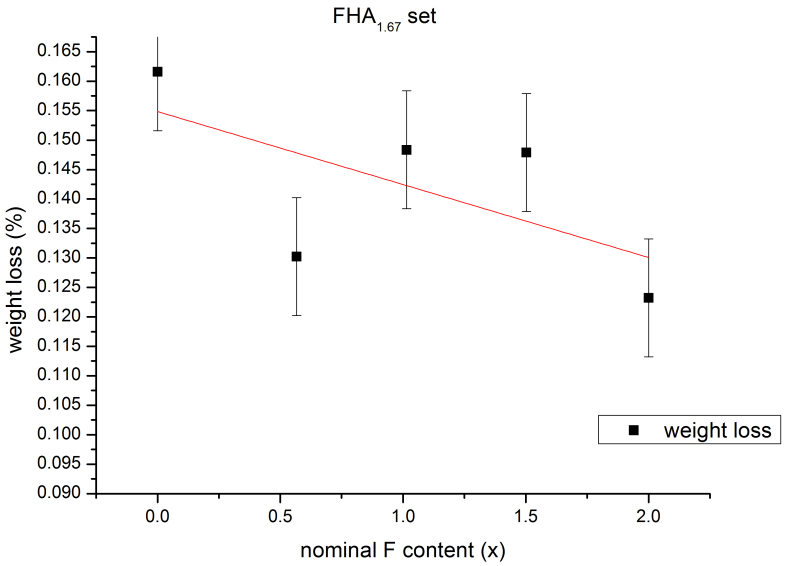

Figure 6.6.2: Relative weight loss after calcination, FHA$_{1.67}$ set

6.7 Crystallinity degree

The crystallinity degree has been calculated through the method introduced in section 5.2.5 and results are resumed in table 6.7.1. The high crystallinity degree of the samples is confirmed, as expected. The *K* value is quite constant and found to be close to 0.09 when the crystallinity degree is about 90%. The F incorporation seems not to interest the X_C parameter, at least until the fluorapatite is reached. The last sample, in fact, shows a much higher crystallinity degree, approx. 95%. This confirms that fluorapatite's microstructural behavior is quite different from the previous samples. Indeed the CDS data agree with this thesis. The increase of crystallinity degree by addition of F in HA lattice is known in literature (LeGeros et al. [57]). For the fluorapatite sample, the *K* value is much lower, and this is consistent with the data collected by Landi et al. [52], in which 10% crystalline apatites reported a *K* value close to 0.24. We can thus state that the *K* value decreases when X_C increases, and the goodness of the data is provided by the fact that K is similar for samples with similar X_C (e.g. $K \approx 0.09$ when $X_C \approx 90\%$).

Sample label	X_C **(%)**	***K* (a.u.)**
HA$_{1.67}$	90.4099	0.08644
0.5FHA$_{1.67}$	89.8180	0.09310
1FHA$_{1.67}$	88.6942	0.09454
1.5FHA$_{1.67}$	89.9024	0.09004
FA$_{1.67}$	95.2933	0.04467

Table 6.7.1: Crystallinity degree of the FHA$_{1.67}$ set

Chapter 7

Ca/P=1.50 FHA set

7.1 XRD characterization and Rietveld Refinement

The results of XRD characterization of the F-doped products synthesized with a nominal Ca/P molar ratio equal to 1.50 is visible in figure 7.1.1. All the XRD patterns show both apatite and β-Tricalcium Phosphate (labelled β-*TCP*, JCPDS file #09-0169) reflection peaks. The term "Biphasic Calcium Phosphate" or BCP will be also used in the following paragraphs to indicate this material.

As one can see, the increasing of F content in the synthesis solution provides a stabilization of the apatite phase. The apatite phase in the non-doped sample ($HA_{1.50}$) is of course hydroxyapatite, but as a small content of fluorine is introduced, it is converted in fluorine-rich apatite. This means that there's not a gradual shift from the HA reflection peaks to the FA ones as shown for the Ca/P=1.67 set (see section 6.1), but an increased presence of a product with high values of *x* appears as the fluorine content increases. Rietveld refinement has been performed as declared above, and agreement factors are reported in table 7.1.1. For this reason the further results will be shown with the starting F/Ca molar value on the x-axis instead of the above mentioned *x*. In the present samples set, the relative errors are practically the same referred before.

Sample label	cR$_{exp}$	χ^2
HA$_{1.50}$	5.27	3.63
0.5FHA$_{1.50}$	5.40	2.77
1FHA$_{1.50}$	5.32	2.74
1.5FHA$_{1.50}$	5.51	3.82
FA$_{1.50}$	5.29	4.09

Table 7.1.1: Agreement factors of the FHA$_{1.50}$ Rietveld refinement set

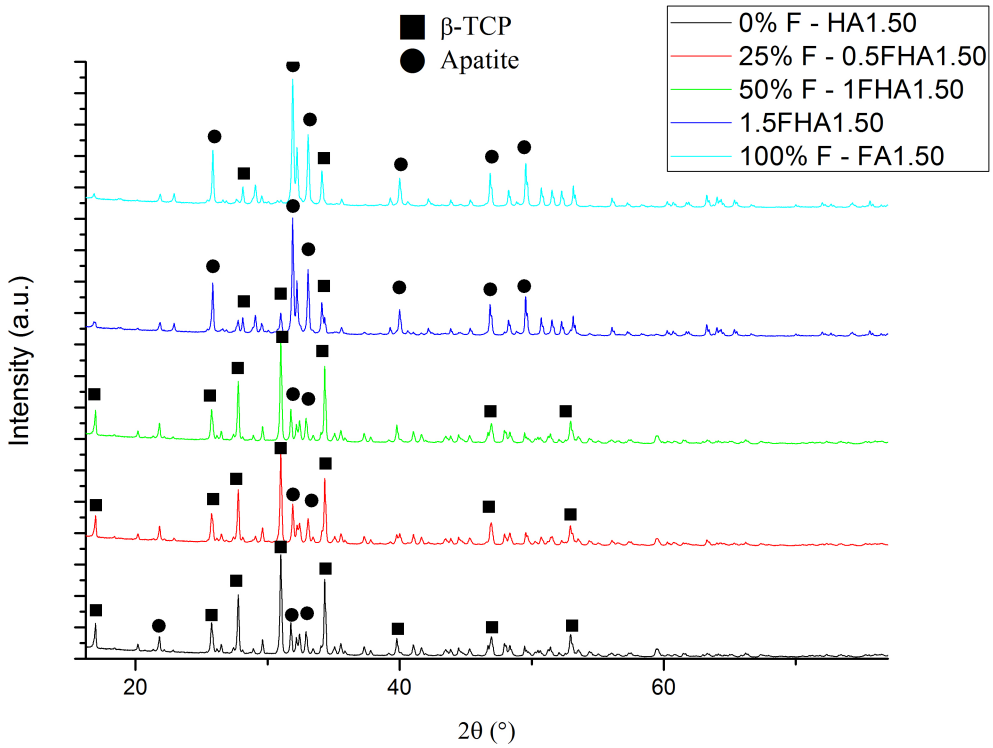

Figure 7.1.1: XRD pattern of the Ca/P=1.50 FHA set

7.2 Phase composition and estimation of real Ca/P molar ratio

The synthesis method provided not only the formation of β-TCP, even if the Ca/P nominal molar ratio was very close to 1.50, but also apatite phase. The increase of apatite (both hydroxy- or fluoroapatite) in the product, having a Ca/P value equal to 1.67, is balanced by the formation of a third phase with Ca/P ratio less than 1.50 to keep unvaried the overall value. This phase is the calcium pyrophosphate in β form, i.e. β-$Ca_2(P_2O_7)$, also called Dicalcium Diphosphate (JCPDS file #33-0297 or 81-2257, ISCD #73712), whose Ca/P ratio is equal to 1. This phase exhibits tetragonal crystal system, space group $P4_1$, with *a*=6.68, *c*=24.14 Å, $\alpha = \beta = \gamma = 90°$. The main peaks are zoomed in figure 7.2.1.

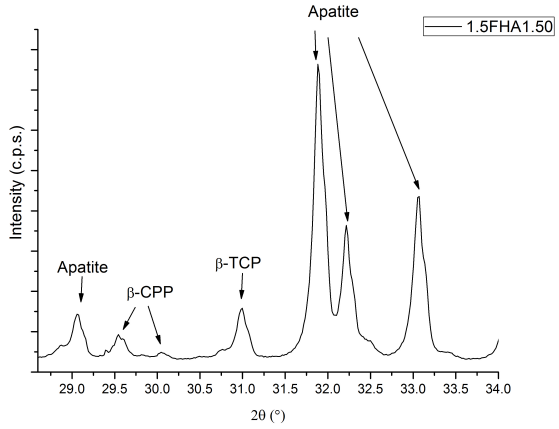

Figure 7.2.1: Zoomed XRD pattern of the $1.5FHA_{1.50}$ sample showing the main peaks of the β-$Ca_2(P_2O_7)$ phase

β-TCP shows a trigonal crystal system, space group R3c, with *a*=10.49, *c*=37.38, $\alpha = \beta = 90°$,$\gamma = 120°$.

The phase composition plotted against the fluorine content (as F/Ca molar ratio) is reported in figure 7.2.2. Table 7.2.1 reports the details of Ca/P estimation after phase composition data provided by the Rietveld refinement output. The phase composition data need to be considered with an absolute error of ± 0.5 mass%.

As one can see, the final Ca/P value of every sample is very close to the nominal one as reported in table 4.3.1, section 4.3, with a maximum mismatch of 0.049 (in the case of

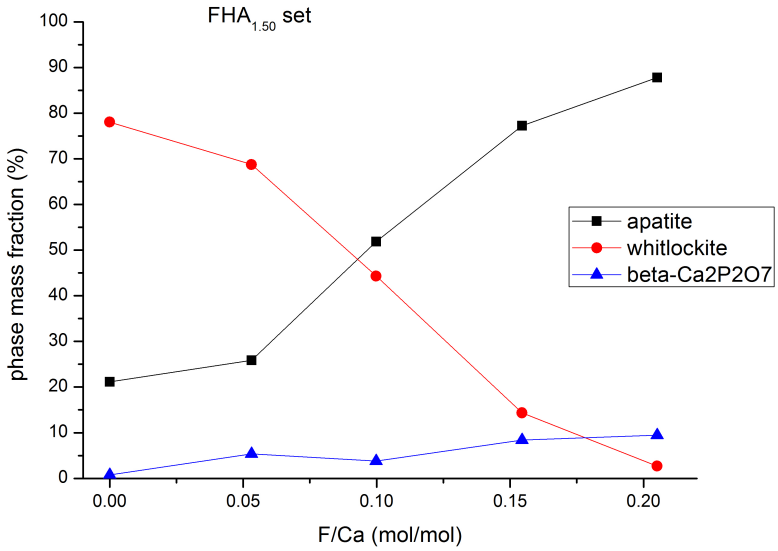

Figure 7.2.2: Phase composition of the $FHA_{1.50}$ set

		apatite		β-TCP		β-$Ca_2(P_2O_7)$		
Sample label	**F/Ca (mol/-mol)**	**mass (%)**	**molar fraction***	**mass (%)**	**molar fraction***	**mass (%)**	**molar fraction***	**calculated Ca/P**
HA$_{1.50}$	0	21.16	0.0764	78.06	0.9125	0.78	0.0111	1.51585
0.5FHA$_{1.50}$	0.0531	25.88	0.0959	68.76	0.8255	5.36	0.0785	1.43553
1FHA$_{1.50}$	0.0998	51.85	0.2463	44.34	0.6823	3.8	0.0714	1.49896
1.5FHA$_{1.50}$	0.1545	77.23	0.4920	14.37	0.2965	8.4	0.2116	1.45056
FA$_{1.50}$	0.2051	87.81	0.6549	2.70	0.0652	9.49	0.2798	1.44608

*normalized to 1

Table 7.2.1: Ca/P calculated value for $FHA_{1.50}$ set after Rietveld refinement phase composition data

0.5FHA$_{1.50}$ sample) which can be fully ascribed to the synthesis uncertainty. The presence of the $\beta-Ca_2(P_2O_7)$ should not astonish, because its deposition, especially in the dihydrate form (CPPD), in hydroxyapatite-based tissues is known to be the cause of arthritic diseases in humans (see chapter 13 of ref. [51]). The initial amount of hydroxyapatite, instead, is to

be referred to the wet-environment synthesis method. It's worth to notice that no α-TCP is found in the samples, thus when Ca/P ratio are close to 1.50, the β form is more stable, because the heating temperature is not higher than 900°C.

The conversion of β-TCP in fluoro/hydroxyapatite is well known in literature, and reported e.g. by Zhu and co-workers [106]. In fact, since the Fluoride ion cannot be hosted in lattices other than apatite, the system tends to stabilize this phase instead of the TCP. The obtaining of the bi-calcium phosphates (BCP), i.e. hydroxy/fluorapatite and β-TCP, whose biomedical application is very well known, can thus be achieved by tuning the F/Ca ratio. A further investigation of possible thermal and/or chemical treatments to remove the β-CPP should be performed.

7.3 Lattice parameters and refined structure

All the present phases structure lattice parameters have been refined and are reported in table 7.3.1. Maximum error for this kind of data is the same resulting from the previous $FHA_{1.67}$ set refinement. No significant trend is observed in the cell volume variation vs fluorine content for the TCP and CPP phases, confirming that no fluoride anion cannot be hosted in those lattices. Figure 7.3.1 shows instead the variation of the cell volume when considering an increasing of the F/Ca molar ratio. This plot confirms that the apatite form which is stabilized by the fluorine doping is particularly F-enriched, because the cell volume values are close to the ones of $1.5FHA_{1.67}$ or to the $FA_{1.67}$ samples introduced above.

7.4 Determination of the *x* value

Once known from the Rietveld refinement the molar content of apatite in the products, it was possible to estimate through ion chromatography the real value of the *x* in the FHA formula. In fact, Fluorine is supposed to be hosted only in the apatite lattice, and not in the other phases one, then the F content in the chromatography analyzed solution should be ascribed only to a smaller part of the phosphates. This is confirmed by the trend shown in figure 7.4.1, plotted by means of the data shown in the inset table. A full agreement with the structural analysis is shown, i.e. instead of a linear augmentation of the *x* content

	Apatite			β-TCP			β-$Ca_2(P_2O_7)$		
Sample label	**a** [Å]	**c** [Å]	**cell volume** [Å^3]	**a** [Å]	**c** [Å]	**cell volume** [Å^3]	**a** [Å]	**c** [Å]	**cell volume** [Å^3]
HA$_{1.50}$	9.41819	6.88105	528.592	10.43516	37.39812	3526.781	6.62997	24.09216	1059.008
0.5FHA$_{1.50}$	9.36983	6.88333	523.351	10.43326	37.40569	3526.212	6.68585	24.1466	1079.367
1FHA$_{1.50}$	9.37039	6.88417	523.477	10.43236	37.42769	3527.679	6.68587	24.15297	1079.657
1.5FHA$_{1.50}$	9.37077	6.88405	523.51	10.43445	37.39862	3526.353	6.68862	24.15211	1080.508
FA$_{1.50}$	9.37107	6.8837	523.518	10.44146	37.39595	3530.838	6.69006	24.15067	1080.91

Table 7.3.1: Refined structural parameters of apatite, β-TCP, and β-CPP in the FHA$_{1.50}$ set

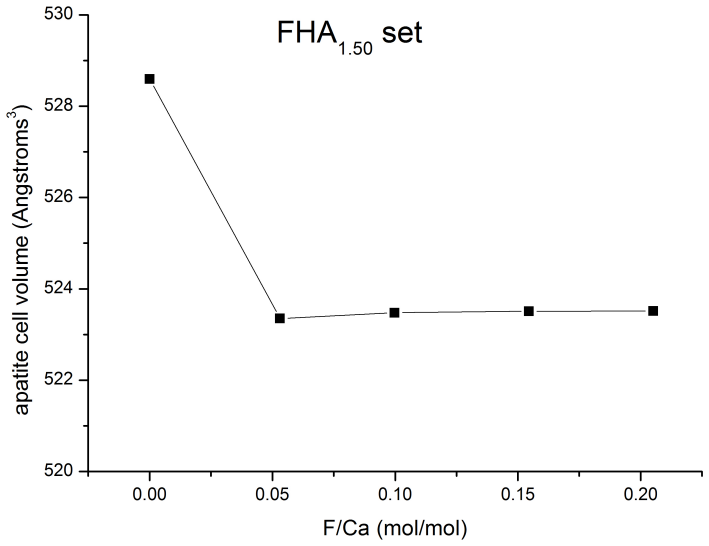

Figure 7.3.1: Apatite cell volume vs F content in the FHA$_{1.50}$ set

as reported for the previous set of samples, a particularly F-rich fluoroxyapatite is formed starting from a low F content in the synthesis solution, and thus the cell volume results to be close to the one of fluorapatite.

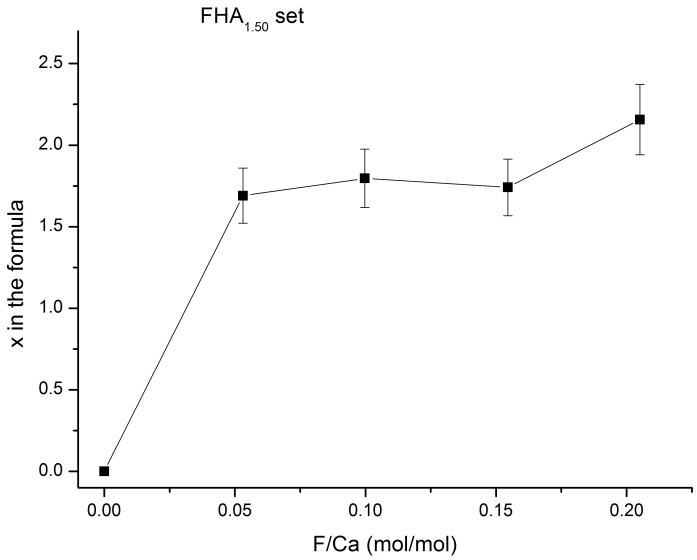

Sample label	F/Ca (mol/mol)	F^- (ppm)	PO_4^{3-} (ppm)	*x*
HA$_{1.50}$	0	0	147.093	0
0.5FHA$_{1.50}$	0.0531	2.112	155.227	1.6899
1FHA$_{1.50}$	0.0998	3.659	123.376	1.7965
1.5FHA$_{1.50}$	0.1545	6.132	141.982	1.7411
FA$_{1.50}$	0.2051	8.321	136.038	2.1566*

*conventionally set to 2

Figure 7.4.1: Estimation of the *x* value in the $FHA_{1.50}$ set

7.5 Coherent domain size, surface area, weight loss upon calcination

As reported in the previous chapter, coherent domain size has been recorded as index of the grain size of the sample. The same absolute error declared above should be considered. Figure 7.5.1 shows the trend of these data, and details are shown in the inset table.

The specific surface area trend seems to confirm the general conclusion stated above (see section 6.6), about the role of F in the $FHA_{1.67}$ set. When considering the coherent domain size, it's worth to say that this is calculated mainly on the β-TCP reflection in the

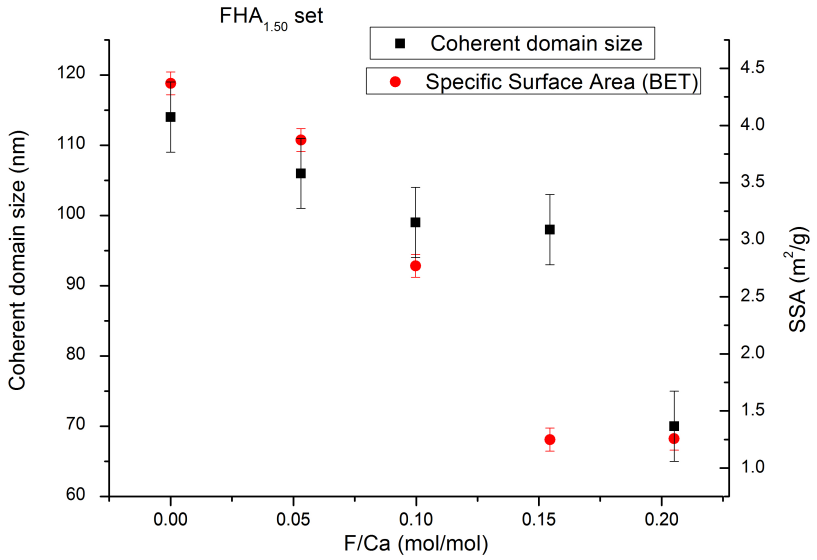

Sample label	F/Ca (mol/mol)	SSA (m^2/g)	CDS (nm)
HA$_{1.50}$	0	4.369	114
0.5FHA$_{1.50}$	0.05313	3.872	106
1FHA$_{1.50}$	0.09978	2.77	99
1.5FHA$_{1.50}$	0.1545	1.249	98
FA$_{1.50}$	0.2051	1.257	70

Figure 7.5.1: Specific Surface Area (BET method) and coherent domain size vs F content in the FHA$_{1.50}$ set

first two samples of the set, and on the apatite reflection in the last three samples, being the apatite more present in those cases. The general trend is similar to the one introduced before, but here the high value for x=2 (i.e. fluorapatite) is missing. This is probably due to the fact that crystals are not formed just by apatite, thus no pure fluorapatite crystals can be obtained in the product. As stated before, in fact, the increment in the grain size is obtained just by the fluorapatite sample, when even F-rich samples show a slight decrease in this value.

When weight loss upon calcination is calculated, the double contribution of apatite and other phosphates should be taken into account. Figure 7.5.2 shows the results of the relative

weight loss vs the F content in the synthesis. A general decreasing trend is observable, although the weakest F-doping produces here an augmentation of the weight loss instead of a decrease as shown in the previous case (see always section 6.6 for comparison).

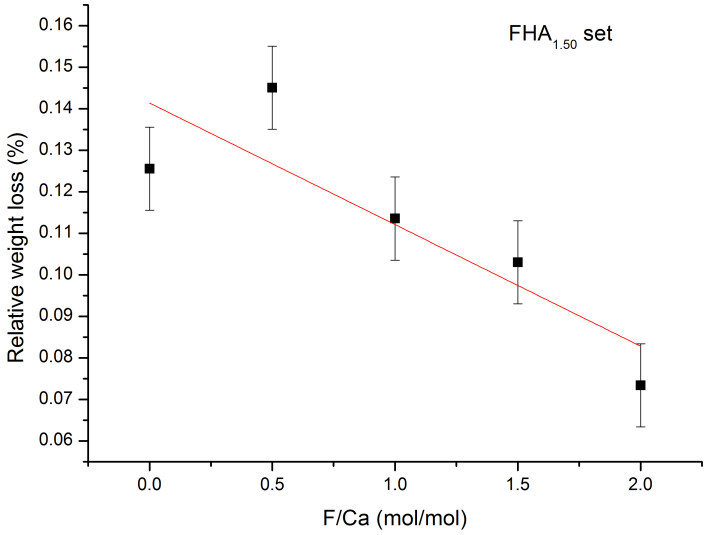

Figure 7.5.2: Relative weight loss after calcination, $FHA_{1.50}$ set

7.6 Crystallinity degree

Because of the presence of β-TCP peaks between the (300) and (112) reflections, the method described in section 5.2.5 is not suitable for high β-TCP containing samples. However, X_C for the $1.5FHA_{1.50}$ and $FA_{1.50}$ was found to be very high, i.e. 90.413% and 90.129%, respectively. The corresponding K values are 0.0789 and 0.0723, and these agree with the previous observations.

Chapter 8

Ca/P=1.28 FHA set

The Ca/P=1.28 series has been characterized only through X-ray diffraction, aiming to verify the capacity of Fluorine to stabilize the apatite phase even with low values of the Ca/P ratio, which normally stabilizes phases other than apatite. Particularly, for such a ratio, Brushite or Monetite ($CaHPO_4 \cdot nH_2O$), and calcium pyrophosphate ($Ca_2P_2O_7$), together with Octacalcium Phosphate ($Ca_3H_2(PO_4)_6 \cdot nH_2O$) are expected. However, the aqueous solution synthesis procedure leads to the production of the more stable β-TCP (JCPDS file #09-0169), as shown in figure 8.0.1.

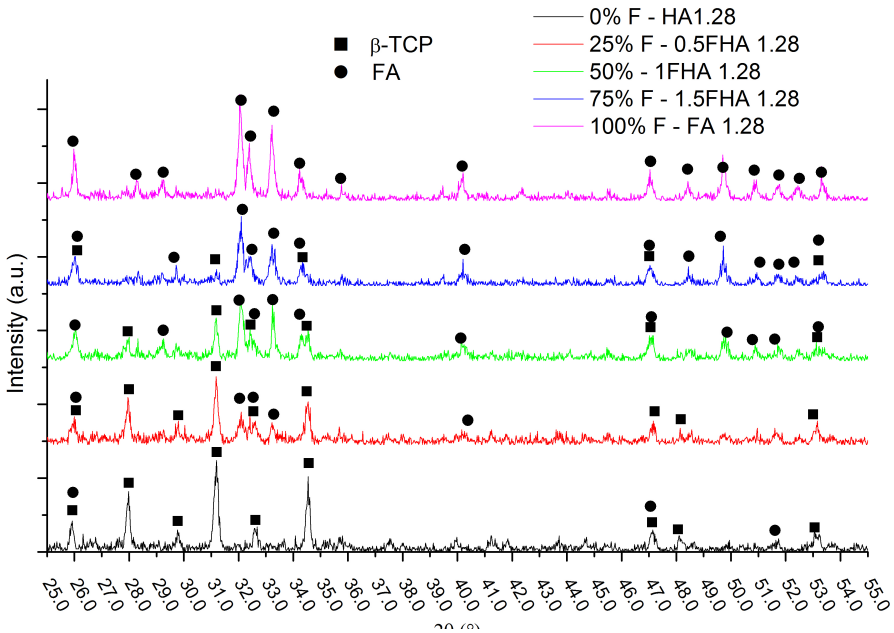

Figure 8.0.1: The Ca/P=1.28 series XRD patterns

When huge F-doping is introduced, fluorapatite phase becomes more stable, in spite of the low Ca/P ratio and relatively high calcination temperature. This was already verified in the Ca/P=1.50 samples set, and similar conclusion about the final phase composition and crystal structure can be drawn.

The apparent non-correlation between the nominal Ca/P ratio and the resulting products Ca/P ratio could be explained in two different ways: either a loss of phosphates from the starting solutions occurs, until the 1.50 or 1.67 Ca/P ratio is achieved, or the formation of Ca-deficient β-TCP and fluorapatite results from the synthesis. Because of the weak interest in such a material for biomedical applications, XRD data for this set have been collected just for phase recognition, thus no Rietveld refinement has been performed to confirm one of those hypothesis, but further analysis should be made.

Chapter 9

Sr-F codoped nanopowders

The synthesis of apatite codoped both with Sr^{2+} cations and F^{-} anions is described in section 4.4. The most important feature to be investigated is the phase composition. In fact, Sr is known to stabilize the β-TCP phase [80], where F, as demonstrated above, has got a positive influence on the hydroxy/fluoro-apatite stabilization. The "diagonal" codoping was employed to investigate both the ions role. In the following figures, the *x*-axis will report both the Sr and F content, following the labelling of the samples: *y*Sr*x*F, where *y* and *x* represent the nominal Sr and F atomic substitution in the $Ca_{10-y}Sr_y(PO_4)_6(OH)_{2-x}F_x$ formula. When not differently declared, the following data show the same relative errors of the ones appeared in chapter 6.

9.1 XRD and Rietveld refinement

Figure 9.1.1 displays the XRD patterns of the codoped apatites samples. The evolution of the main peaks of apatite and β-TCP are labelled, as introduced above. Here, the shift of hydroxyapatite characteristic peaks is generated by two different causes: the incorporation of Sr atoms and of F atoms. The first being bigger than the Ca substituted atoms, tend to increase the lattice parameters, and so the cell volume. This effect is exactly the opposite of the F atom's one. So, the main apatite reflection peak does not show a linear shift as the codoping increases, as in the previous case of $FHA_{1.67}$ set. Apart from the diagonal codoping set is shown the XRD pattern of the 05Sr2F sample.

Rietveld refinement provided the best results in terms of χ^2 for this data set, with respect to the other sets. However, this is due to the relatively high values of the cR_{exp} of

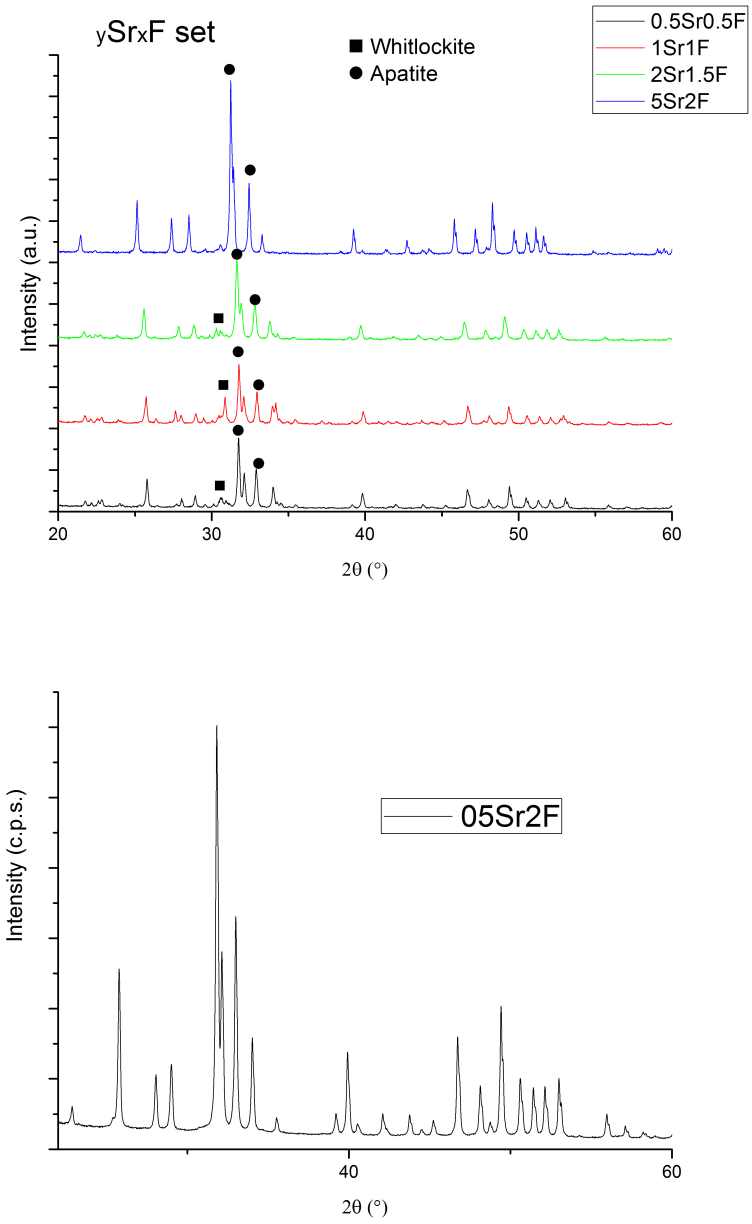

Figure 9.1.1: Sr-F codoped apatites set XRD patterns

those samples fittings. This is caused by a weak refinement of secondary phases structural parameters, such in α-TCP, (see next section), which provided much more refining variables without a corresponding improvement of the fitting. Details about this aspects are

shown in table 9.1.1. In all the fittings, the occupancy factors of Ca1 and Ca2 apatite sites have been refined in order to investigate a preferential substitution of Sr for Ca in the first or second site. The isotropic temperature factor (B_{iso}) has been forced to be equal for both the Ca and Sr atoms. Typical values are around 0,6/0,7.

Sample label	**cR**$_{exp}$	χ^2
0.5Sr0.5F	17.98	1.19
1Sr1F	18.06	1.25
2Sr1.5F	19.38	1.31
5Sr2F	19.47	1.40
0.5Sr2F	4.51	3.52

Table 9.1.1: Agreement factors of the Sr-F codoped samples Rietveld refinement set

9.2 Phase composition

Although the synthesis conditions corresponded to apatite as only present phase, α-TCP and β-TCP phases are detected in this samples set. The variation of phase composition is respresented in figure 9.2.1, while the inset table shows the plot details. In the graphic, the mass phase composition is projected on the XZ and the YZ walls in order to appreciate the trend against the F and Sr nominal content variation.

With respect to the previous FHA$_{1.67}$ set, it's worth to notice that a slight Sr doping leads to a high formation of TCP, both in α or β form (see also chapter 6). Let's compare for instance the composition of 0.5FHA$_{1.67}$ and 0.5Sr0.5F: these two samples share the same nominal F content, and the only difference is given by the 5% atomic Sr for Ca substitution. In the first sample, no β-TCP is found and the α-TCP presence is less than the half with respect to the 0.5Sr0.5F sample. When the F content increases, apatite is stabilized as reported before for the Ca/P=1.50 data sets. The 0.5Sr2F sample resulted to be composed only by apatite phase. Sr is supposed to enter easily in both the TCP lattices, forming a Ca,Sr:TCP product with general formula $Ca_{3-z}Sr_z(PO_4)_2$ as stated by Renaudin and co-workers [80]. This stabilization is due to the higher number of energetic-

preferred sites available in the β-TCP form: in fact, Sr shows a preference to enter in the β-TCP or α-TCP lattices, when these phases are present, as will be discussed later. Thus, the TCP phases stabilization (in α or β form) is a logical consequence.

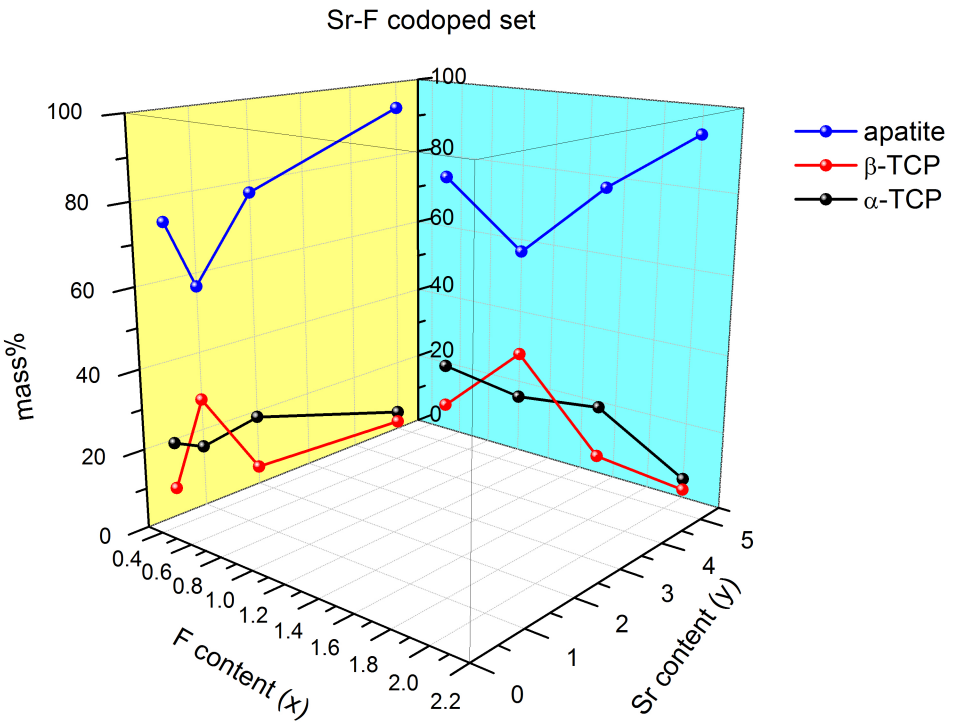

Sample label	nominal F content (x)	nominal Sr content (y)	mass fraction (%)		
			apatite	β-TCP	α-TCP
0.5Sr0.5F	0.5	0.5	73.93	7.14	18.94
1Sr1F	1	1	56.69	27.81	15.5
2Sr1.5F	1.5	2	77.13	4.54	18.33
5Sr2F	2	5	92.97	2.07	4.95
0.5Sr2F	2	0.5	100	0	0

Figure 9.2.1: Phase composition of the Sr-F codoped set against both Sr and F content

9.3 Estimation of the real (Ca+Sr)/P ratio

Sample label	Ca+Sr/P
0.5Sr0.5F	1.64304669
1Sr1F	1.591152859
2Sr1.5F	1.626020359
5Sr2F	1.653991253

Table 9.3.1: (Ca+Sr)/P Rietveld refinement calculated ratios of the Sr-F codoped set

The calculation of the real (Ca+Sr)/P molar ratio moving from the Rietveld refinement data has been performed with the same method shown in section 6.3, with the only hypothesis that (Ca+Sr)/P ratios of both TCP forms were 1.50, and $1.\bar{6}$ for the apatite phase. This is of course true independently of the real Sr substitution for Ca in every lattice. Since the atomic weight of Sr is 87,62 amu, more than twice the value of Ca atomic weight (40,08 amu), every phase molar weight changes when considering the Sr doping. E.g. a Ca:TCP molar mass is 310.18 g/mol, but when a Ca,Sr:TCP is formed with a chemical composition $Ca_2Sr(PO_4)_2$, it has a molar mass of 357.72 g/mol. This has been taken into account when converting the sample mass composition in molar composition, and then when using this value to calculate the final (Ca+Sr)/P ratio. Results of this calculation are reported in table 9.3.1. As one can see, the formation of TCP resulted to decrease the final (Sr+Ca)/P value with respect to the synthesis one. Renaudin et al. [80] hypothesize the formation of an amorphous quantity of Ca,SrO, not detected by XRD data. This is supposed to happen also in our samples set, and the greatest amount of this Ca,SrO amorphous phase, supposing a Sr for Ca substitution proportional to the nominal *y*, is detected in the 1Sr1F sample. This corresponds to a 1.046 mass% and a 0.07 molar fraction.

9.4 Lattice parameters and refined structure

The variation of α and β-TCP unit cell volume plotted against the nominal Sr content in the sample are shown in figure 9.4.1, while details about the samples phases lattice parameters are given in table 9.4.1.

Sample label	**Sr/Ca (mol/-mol)**	**F/Ca (mol/-mol)**	**Apatite**			**β-TCP**			**α-TCP**			
			a [Å]	**c** [Å]	**unit cell volume** [Å^3]	**a** [Å]	**c** [Å]	**unit cell volume** [Å^3]	**a** [Å]	**b**[Å]	**c** [Å]	**unit cell volume** [Å^3]
HA$_{1.67}$*	0	0	9.42180	6.88130	529.020	10.4352	37.4029	3527.260	12.8870	27.2800	15.2190	4317.530
0.5Sr0.5F	0.05057	0.05203	9.41582	6.89750	529.588	10.4554	37.4905	3549.251	12.9072	27.4620	15.2592	4350.142
1Sr1F	0.10028	0.10019	9.40277	6.91188	529.223	10.4785	37.5366	3569.310	12.9459	27.5405	15.2868	4379.114
2Sr1.5F	0.19986	0.15000	9.44121	6.95107	536.584	10.5274	37.8203	3629.952	13.021	27.6900	15.3435	4437.191
5Sr2F	0.49919	0.20340	9.54779	7.07433	558.521	10.4784	38.1869	3631.047	12.9566	27.6243	15.4344	4405.937

*taken from the FHA$_{1.67}$ samples set

Table 9.4.1: Structural parameters of all phases in Sr-F codoped samples

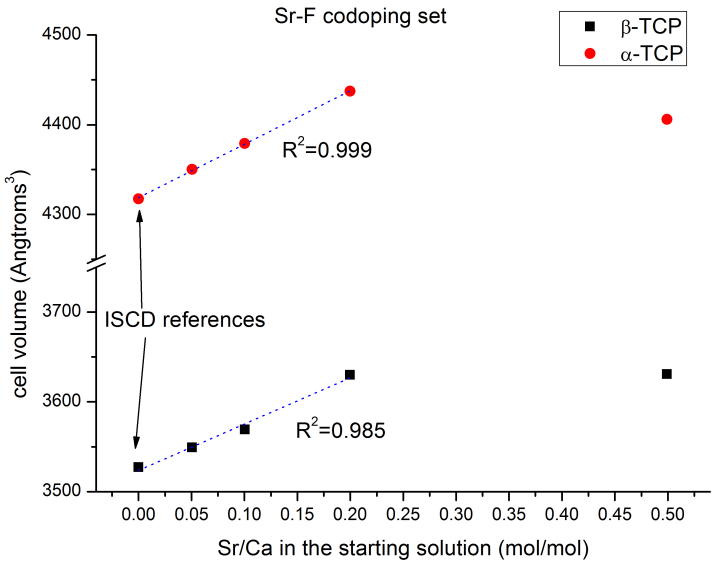

Figure 9.4.1: Variation of TCP unit cell volume vs Sr content (nominal) in the Sr-F codoped set

The first point of this plot, corresponding to *y*=0, is taken from the ISCD references of pure β-TCP and pure α-TCP. The first 4 points of the plot show a quite good alignment, producing a R^2 value of 0.999 and 0.985 for α and β-TCP samples, respectively. This means that increasing the Sr^{2+} content in the synthesis solution, produces a linear increase of the z value in the $Ca_{3-z}Sr_z(PO_4)_2$, and a linear increase in the observed unit cell volume, in agreement with the Vegard's law. The volume variation is due to an increase in all the lattice parameters of the TCP structure, both in α and β form. The maximum percentage increase in the single lattice parameters, expressed as $(d_{max} - d_{min})/d_{max}$ for both the TCP forms, is resumed in table 9.4.2.

As one can see, Sr provides an increase along all the directions in both the TCP forms, with a preferential increase along the c parameter in β-TCP and an almost indifferent increase in the *a, b,* and *c* lattice parameters in the α-TCP phase. The most Sr doped sample corresponds to the most F doped one: 5Sr2F. With respect to the 2Sr1.5 sample, the β-TCP unit cell volume seems to be almost unvaried, and the α-TCP cell volume results to be slightly smaller. This could mean that when apatite phase is much more stable (92.97 mass% in the 5Sr2F sample, 77.13mass% in the 2Sr1.5F sample), Strontium tends to enter

Phase	Δ**a/a**$_{max}$ **(%)**	Δ**b/b**$_{max}$**(%)**	Δ**c/c**$_{max}$**(%)**
$\alpha - TCP$	1.03	1.48	1.40
$\beta - TCP$	0.87	/	2.07

Table 9.4.2: Maximum percentage increase of lattice parameters in the $\alpha$and β-TCP structures caused by Sr introduction

more in the apatite lattice, and less in the two TCP ones. This is confirmed by the evolution of apatite volume with respect to the Sr nominal content, shown in figure 9.4.2, where the corresponding nominal F content is reported in brackets (as $mols_F/mols_{Ca}$). The first point of the plot, corresponding to a pure hydroxyapatite (i.e. 0Sr0F) is taken from the $HA_{1.67}$ sample.

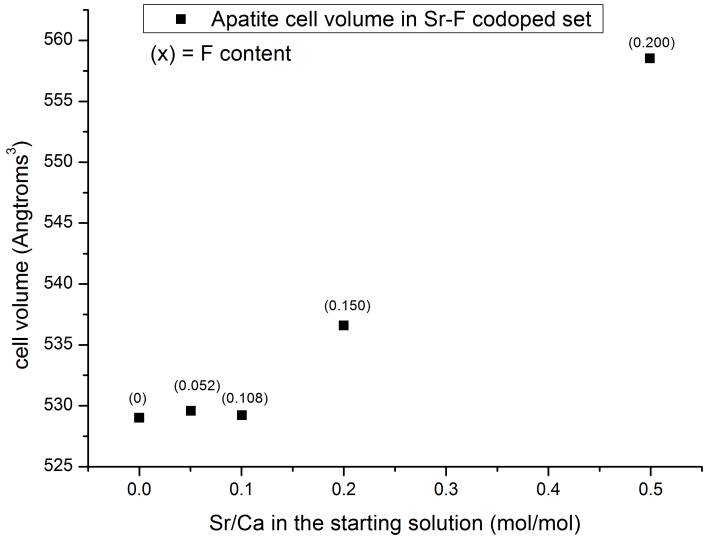

Figure 9.4.2: Apatite cell volume vs Sr nominal content, Sr-F codoped set

Remembering that Sr tends to increase the cell volume and that F tends to decrease it, it's worth to notice that the apatite cell volume shows a little decrease in the case of 1Sr1F sample, where the apatite mass fraction is less than 57%. This confirms that Sr substitutes Ca preferentially in the two TCP phases than in the apatite one, but when apatite

phase becomes more stable (again, 5Sr2F) the great apatite's unit cell volume augmentation suggests that a high quantity of Sr is finally entered in the apatite lattice. Let's consider the influence that Sr has on the single lattice parameters: as reported before, the *a* parameter is decreased linearly with a F for OH substitution, but the *c* parameter remains almost unvaried.

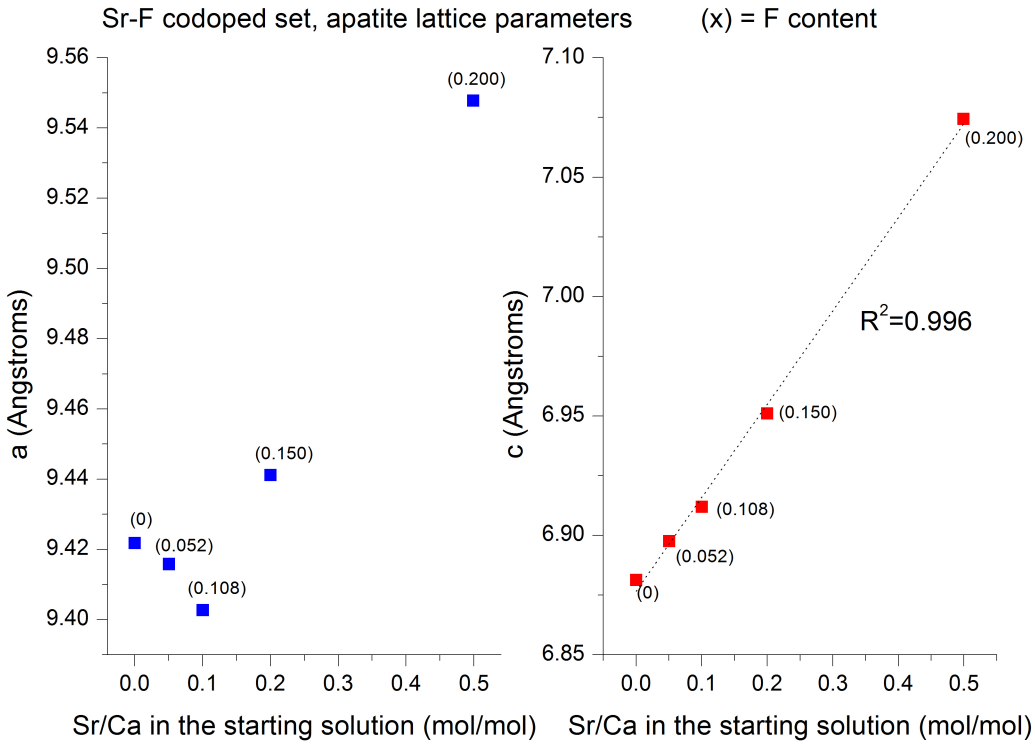

Figure 9.4.3: Apatite lattice parameter vs nominal Sr content, Sr-F codoped set

In figure 9.4.3 both *a* and *c* vs the nominal Sr content are plotted, with the corresponding fluorine content indicated in brackets. For the first three samples, i.e. for low values of Sr content, the *a* parameter shows a little decrease due to the increasing F content. But starting from the 2Sr1.5F sample, a huge increase is produced. The *c* parameters trend shows a perfect linearity with the increasing of the Sr content (correlation factor is 0.996). This confirms that the F for OH substitution does not influence the *c* value that much as the Sr for Ca one. The same plot suggests also that a preferential substitution in the Ca2 site is possible, especially in the case of weak Sr-doping, as will be discussed later.

9.5 Site preference for Sr substitution in HA lattice

As reported by Michie and co-workers [70], the Ca1 is a 4f site, 9-fold coordinated by the phosphate group oxygen ions (i.e. O1, O2 and O3 positions), with six shorter Ca-O distances and three longer Ca-O distances. The Ca2 is a 6h site 7-fold coordinated, with six Ca-O bonds from phosphate group oxygen atoms and one Ca-OH (or Ca-F) bond with the anion located in c-axis channels. In the same work, many interpretations are reported for the assessment of the real preferential site for Sr substitution of Ca. Not all the interpretations lead to the same conclusion.

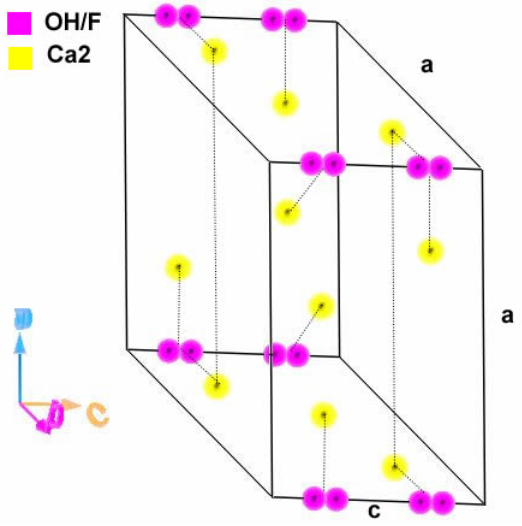

Figure 9.5.1: The simplified apatite unit cell, where only Ca2 and O4 sites are marked

Ca2 site selectivity for low Sr-doped hydroxyapatite samples has been proved by Bigi et al. (see ref.[7], but only when Sr atomic substitution is higher than 10%) and Renaudin et al. [80]. To understand this preference, let's consider the simplified apatite unit cell represented in figure 9.5.1, in which only the Ca2 sites are shown (yellow) together with the O4 sites (pink). The O4 4e sites can be occupied either by an OH group or by a single F atom. To make the comprehension of the structure easier, phosphate groups and Ca1 sites have been omitted, but figure 6.4.2 in section 6.4 should be compare for completeness.

The description is made clearer too by the observation of figure 9.5.2, taken by ref. [80], which shows the Calcium environments of Ca1 and Ca2 sites in the hydroxyapatite structure.

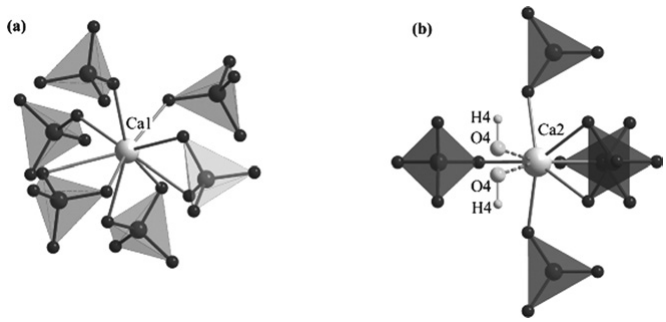

Figure 9.5.2: The Ca1 (a) and Ca2 (b) environments as described by Renaudin et al. [80]

Renaudin and co-workers, in fact, suppose that the Ca2 site allows the bigger Sr cation, at low substitution levels, because of the possibility to displace the hydroxil groups along the z direction, producing a moderate influence on the lattice parameters. This is facilitated also by the 7-fold coordination. This substitution provokes an increase in both the *a* and *c* parameters, but the first three samples of the codoped set show a non linear trend in the *a* parameter because of the contemporary presence of F in the lattice. But since the *c* axis is not significantly affected by the F insertion, this parameter increases linearly with the Sr doping. This increase is given by the sliding of the OH groups (or F atoms) just along the *z* direction, i.e. along the *c* axis, outwards; this lateral slide is probably due to the contemporary interaction of every O4 site with at least two Ca2 sites. The OH group or the F atom are then forced to slide towards the *outer* part of the unit cell, leading to a general *c* axis increase. In the $FHA_{1.67}$ set, the *z* refined position of the O4 site, shows a general increase (even if not perfectly linear) when inserting F atoms. This means a slide of the O4 centers towards the *inner* side of the cell[1]. But the *c* parameter was not shortened by this *inwards* slide because of the presence of the 3 by 3 aligned Ca1 sites along the same axis, whose approach of one to the other is restrained by the electrostatic interaction, as we already said in section 6.4. In this case, no obstacle is put against a *stretch* of the *c* parameter, and in fact the *z* refined position of the O4 site of the Sr-F codoped samples set does not record the same increase, especially in the 1Sr1F sample (where z=0.225, while the corresponding $1FHA_{1.67}$ reports z=0.227). In conclusion, because the F doping, as mentioned before, produces an *increase* of this factor, this observed light *decrease* should be fully attributed to the outward slide caused by the Sr substitution.

[1]The higher the *z* atomic position value is, the more the atom is distant from the corner of the unit cell

9.6 Cation sites occupancy factors refinement

The site occupancy factor refinement confirms the previous description. The nominal Ca1 and Ca2 occupancy factors (OF) for hydroxyapatite are respectively $0.\bar{3}$ and 0.5. Sr1 and Ca1 occupancy factors were forced to be complementary, i.e. $O.F._{Ca1} + O.F._{Sr1} = 0.\bar{3}$, and for the same reason the sum of Sr2 and Ca2 sites occupancy factors has been forced to be 0.5. Table 9.6.1 resumes the refined values for both sites. The reported values are approximated, and a ± 0.00005 error should be considered. The "normalized O.F." represents the relative occupancy of Sr atoms for Ca in every site, i.e. it's a factor going from 0 to 1, expressing the Sr substitution for Ca in site 1 or 2, calculated by the expression: $O.F_{Sr\ i}/(O.F._{Ca\ i} + O.F._{Sr\ i})$, where $i = 1$ or 2. In the same way, an "overall O.F." takes into account the total substitution of Sr for Ca in both the sites: $(O.F_{Sr1} + O.F._{Sr2})/(O.F._{Ca1} + O.F._{Sr1} + O.F._{Ca2} + O.F._{Sr2})$. The overall O.F. provides an estimation of the *y* value in the Sr:FHA chemical formula, by the simple multiplication per 10.

Sample label	Ca1 O.F.	Sr1 O.F.	normalized Sr1 O.F.	Ca2 O.F.	Sr2 O.F.	normalized Sr2 O.F.	overall Sr O.F.
0.5Sr0.5F	0.3311	0.00223	0.00669	0.48243	0.01757	0.03514	0.0238
1Sr1F	0.33008	0.00325	0.00975	0.46622	0.03378	0.06756	0.0444
2Sr1.5F	0.30979	0.02354	0.07062	0.39346	0.10654	0.21308	0.1561
5Sr2F	0.22773	0.10560	0.31680	0.21502	0.28498	0.56996	0.4687

Table 9.6.1: Occupancy factors for Ca1, Ca2 and corresponding Sr1 and Sr2 cation sites in the apatite unit cell

The dotted green line in figure 9.6.1 represents the theoretical Sr O.F. in the double hypothesis that:

1. Sr is hosted in the apatite lattice in the amount indicated by the nominal *y* value.
2. Sr occupies indifferently both the Ca1 and the Ca2 sites.

But figure 9.6.1 shows that the 6h site (i.e. Ca2) is constantly more occupied by Sr atoms than the 4f site (i.e. Ca1), which remains Ca-full for the first two samples of the set.

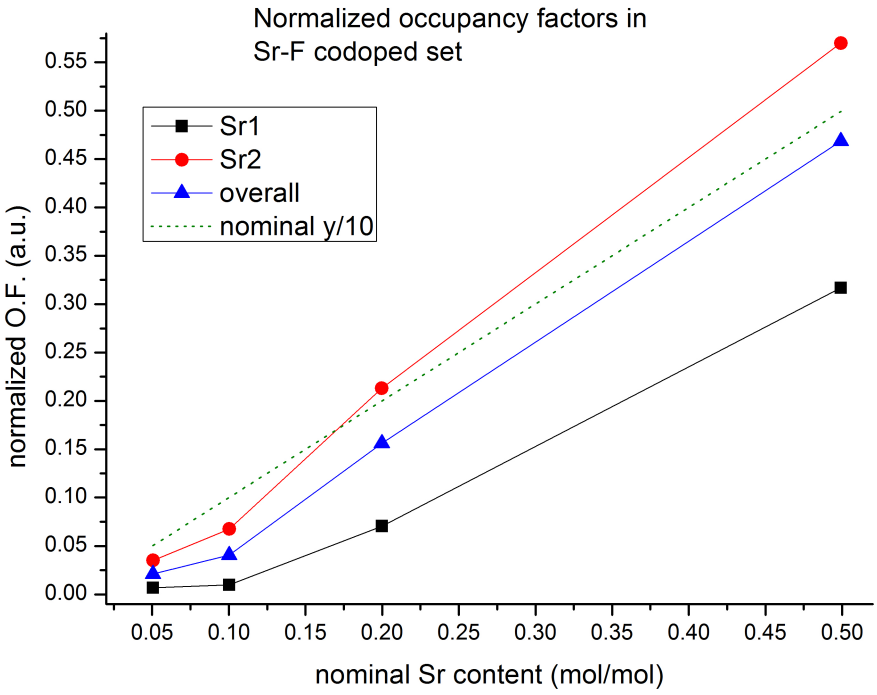

Figure 9.6.1: Normalized Sr1, Sr2, and overall Sr O.F. dependence on Sr nominal content in the Sr-F codoped samples

When a huge doping is reached (5Sr2F), Sr atoms are hosted in both sites, but still with a 6h preference. In fact, in the case of 2Sr1.5F and 5Sr2F, the normalized O.F. of Sr2 are respectively ∼0.21 and ∼0.57, both higher than those provided by a theoretical homogeneous substitution, i.e. 0.2 and 0.5. For the 0.5Sr0.5F and 1Sr1F samples, the opposite happens, i.e. normalized Sr2 O.F. are lower than theoretical homogeneous substitution. On the contrary, Sr1 O.F. is always lower than the corresponding theoretical one. The overall normalized O.F. being an average of both the single O.F., reveals that the nominal y value, i.e. the dotted green line, is never reached. In fact, if the y value was respected, the overall O.F. should increment as follows: 0.05, 0.1, 0.2, 0.5. Here and in table 9.6.1 we can see that only the latter two samples of the set approach these values, thus it's necessary to increment the Sr content in the synthesis solution to come close to the nominal y.

This result is in good agreement with the above described lattice parameters and phase composition analysis. The Sr, in fact, is hosted largely in the α and β-TCP phases, and

it's forced to enter massively in the apatite lattice only when this phase is highly stabilized (almost 93% in mass, corresponding to the 5Sr2F sample), because the other phases do not provide enough sites to host the Sr atoms. The availability of Ca1 sites for Sr substitution at high levels of Sr in the product leads to an increase of the Sr content in the apatite, and explains the "jump" in the *a* parameter values registered in the 9.4 section. It explains also the non-increase of the two TCP unit cell volume when considering the 5Sr2F sample: the available Ca-replaceable sites in those phases have been "saturated" and other sites are needed.

But since not all the nominal Sr atoms enter in the apatite lattice, especially in the first two samples of the set, one can wonder where the remaining Sr content is hosted. There can be two hypothesis:

1. The Sr enters preferentially in the two TCP lattices, forming Sr-rich TCP. That is to say that in the two TCP lattices Sr reaches more than the nominal z value. E.g., for the y=1 sample (1Sr1F) the synthesis solution contains 1 Sr cation every 10 cations. Thus, the TCP nominal formula, (wether α or β form) should be $Ca_{2.6}^{-}Sr_{0.3}^{-}(PO_4)_2$, i.e. with nominal z=$0.\bar{3}$. But if a Sr substitution is done in more than the nominal z value, one could find a TCP phase with z values higher than $0.\bar{3}$.

2. The Sr forms an XRD-undetectable Ca,SrO phase, as hypothesized in section 9.3.

As reported before, the unit cell volume of both α and β-TCP phases are quite well aligned according to the Vegard's law (see figure 9.4.1). This means that the Sr substitution increases linearly with the Sr content in the synthesis solution. If the first hypothesis would be verified, a more than linear increment of the cell volume should be recorded when increasing the nominal Sr content. It could happen also that the TCP increases linearly its cell volume, but with linear slope higher than the Vegard's one. If, for instance, for an increment of y a (say) double increment of z is recorded, the linear dependence is still verified but the true z is higher than the nominal one. This situation is not so likely[2], and moreover, to verify this, one could either verify the slope of the Vegard's dependence or verify the overall O.F. of Sr in both the TCP lattices. Unfortunately, no data are available about the structural parameters of the fully-substituted $\alpha-$ or $\beta - Sr_3(PO_4)_2$ minerals, so the application of Vegard's law is not suitable. We remember also that real cell parameters

[2]That is, if a linear dependence is observed, it's very likely attributed to the real Vegard's law

values depend (weakly) on the heating treatment and on the eventual presence of impurities in the starting products, thus we'd need data on a product synthesized with the same conditions. But since 4 points in the cell volume vs nominal content plot are well aligned, one can quite surely infer that Vegard's law is respected.

On the other hand, the two α and β-TCP phases show respectively 18 and 5 independent cation positions, and the refinement of each site O.F. resulted in a non-convergence of the fitting.

Thus, the second hypothesis is more likely; moreover, this hypothesis can explain also the discrepancy of the nominal (Ca+Sr)/P content with respect to the nominal one, as showed in section 9.3. This means that as long as TCP phase is stable, Sr substitution is performed preferentially in this phase (particularly, as in ref. [80], in the Ca4 β-TCP site) and in Ca2 apatite sites. When those sites are occupied, it becomes energetically preferable to occupy the Ca1 apatite sites too.

9.7 Determination of the *x* value and definition of the Sr:FHA chemical formula

As described in the previous chapters, the *x* value in the $Ca_{10-y}Sr_y(PO_4)_6(OH)_{2-x}F_x$ formula has been evaluated by ion chromatography. Like in the $FHA_{1.50}$ samples set, the molar composition of the Sr-F codoped samples was necessary to calculate the amount of phosphate in the analyzed solution that could be attributed to the apatite phase. We repeat that fluorine is supposed to be hosed only in the apatite lattice. Results of this analysis are reported in figure 9.7.1 and in the inset table.

As already observed in the $FHA_{1.50}$ set, when apatite is less present, like in 1Sr1F sample, the phase which is formed contains high quantities of fluorine, i.e. it's an almost-fluorapatite phase. This contributes to explain the neat decrease of the apatite cell volume in the case of the just mentioned sample with respect to the others of the set.

Taking into account the y values calculated from the overall normalized Sr occupancy factor, as shown in the previous section, one can obtain an estimation of the synthesized product's apatite fraction chemical formula, as reported in table 9.7.1.

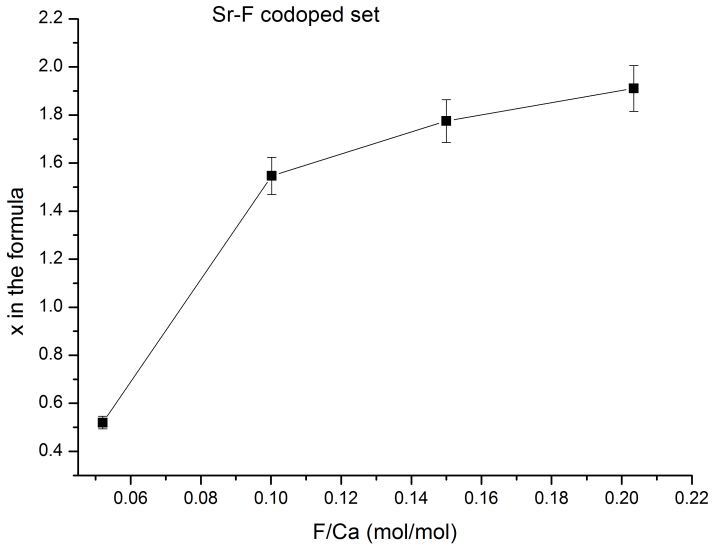

Sample label	F/Ca (mol/mol)	F^- (ppm)	PO_4^{3-} (ppm)	*x*
0.5Sr0.5F	0.05203	2.089	140.367	0.52003
1Sr1F	0.10018	3.810	135.102	1.54641
2Sr1.5F	0.15000	5.821	130.088	1.77481
5Sr2F	0.20340	6.502	110.490	1.91012
0.5Sr2F	0.20076	11.020	166.980	1.97944

Figure 9.7.1: The *x* value in the Sr:FHA formula estimated through ion chromatography

Sample label	Chemical formula of the apatite fraction
0.5Sr0.5F	$Ca_{9.76}Sr_{0.24}(PO_4)_6(OH)_{1.48}F_{0.52}$
1Sr1F	$Ca_{9.56}Sr_{0.44}(PO_4)_6(OH)_{0.45}F_{1.55}$
2Sr1.5F	$Ca_{8.44}Sr_{1.56}(PO_4)_6(OH)_{0.23}F_{1.77}$
5Sr2F	$Ca_{5.31}Sr_{4.69}(PO_4)_6(OH)_{0.09}F_{1.91}$

Table 9.7.1: Chemical composition of Sr:FHA samples

9.8 The 0.5Sr2F sample

As showed in the first part of this chapter, this sample is formed by pure apatite phase, thus, the (Ca+Sr)/P nominal value is respected. The ion chromatography analysis report an *x* value of 1.979444, i.e., considering the uncertainty of the technique, the sample is constituted of fluorapatite. Concerning the Sr substitution, it's worth to notice that a preferential accommodation in the 6h site is still shown, but the refinement of the 4f site led to the value of a normalized O.F. for Ca1 of 0.003. Details of the calculations are shown in table 9.8.1.

Sample label	Ca1 O.F.	Sr1 O.F.	normalized Sr1 O.F.	Ca2 O.F.	Sr2 O.F.	normalized Sr2 O.F.	overall Sr O.F.
0.5Sr0.5F	0.33233	0.00100	0.00300	0.47117	0.02883	0.05766	0.03580

Table 9.8.1: Occupancy factors for Ca1, Ca2 and corresponding Sr1 and Sr2 cation sites in the apatite unit cell, 0.5Sr2F sample

As one can see, the overall Sr O.F. is much higher than the corresponding 0.5Sr0.5F sample. This confirms that when apatite is well-stabilized, Sr is forced to be hosted in the apatite lattice in higher quantity. The *y* calculated from the overall Sr O.F. is 0.358, i.e. a bit smaller than the nominal 0.507. Thus, as observed before, a little part of the nominal Sr should have formed an XRD-undetectable Ca,SrO amorphous phase. The final 0.5Sr2F sample formula is $Ca_{9.64}Sr_{0.36}(PO_4)_6(OH)_{0.02}F_{1.98}$.

The refined lattice parameters for this phase are: *a*=9.39029 Å, *c*=6.9018 Å, with a resulting cell volume of 527.049 Å^3. Since this product can be considered a fluorapatite, its cell volume has been compared to the one of the other previously introduced fluorapatites, i.e. the $FA_{1.67}$ and the 5Sr2F samples. The cell volume has been plotted against the calculated *y* in the formula, and results are shown in figure 9.8.1.

The good agreement with the linear fitting ($R^2 = 0.99915$), although only three data points are plotted, suggests that the linear dependence is confirmed, and thus that the *y* values calculated from the overall normalized refined O.F. of Sr are acceptable.

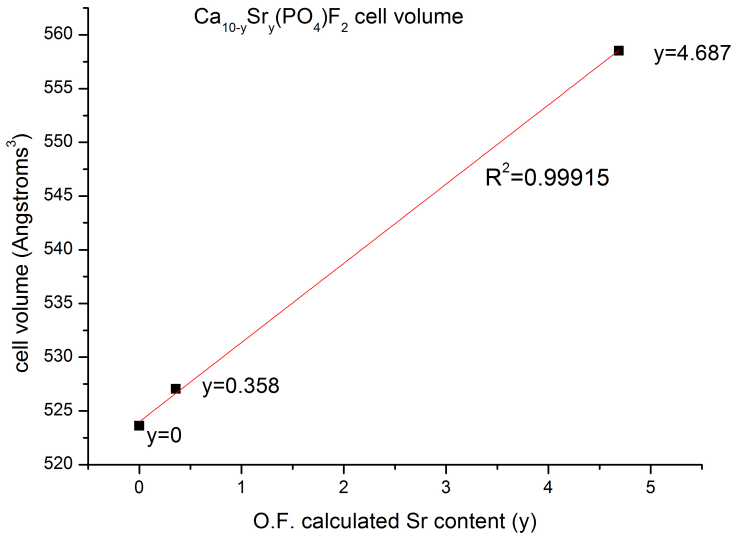

Figure 9.8.1: Cell volume of Sr-doped fluorapatites vs Sr content

9.9 Coherent domain size, surface area, weight loss upon calcination

The data on coherent domain size (CDS) and specific surface area (SSA) are collected in table 9.9.1. The same errors stated in chapter 6 are considered.

Sample label	SSA (m^2/g)	CDS (nm)
0.5Sr0.5F	3.074	83
1Sr1F	4.387	86
2Sr1.5F	5.481	57
5Sr2F	3.383	107
0.5Sr2F	6.258	72

Table 9.9.1: Specific Surface Area (BET method) and coherent domain size in the Sr-F codoped apatites set

By comparison with the $FHA_{1.67}$ set, one can see that the general trend of decreasing

the coherent domain size when the F content in the product increases is confirmed, but no obvious dependence is revealed. The 5Sr2F sample, being formed by mere fluorapatite, shows the same "jump" in the CDS value recorded with the corresponding $FA_{1.67}$ sample. However, the 0.5Sr2F sample behaves differently from this trend. The SSA does not show a significant trend no more, but in general one can observe that the registered values are slightly higher than the ones recorded for the $FHA_{1.67}$ set. Those values are actually resulting from many variables in the synthesis, such as Sr and F content, phase composition, and milling procedure. They will be useful for the evaluation of the dissolution studies in the next chapters.

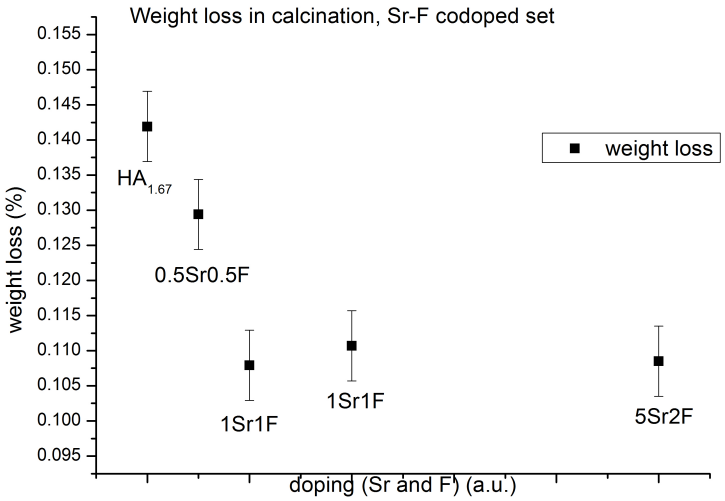

Figure 9.9.1: Relative weight loss after calcination, Sr-F codoped set

Concerning the percentage weight loss before and after the calcination, reproduced in figure 9.9.1, we can confirm the general trend of decrease with increasing the F content, and no particular influence seems to be given by the Sr-doping. Again, the 0.5Sr2F sample behaves very differently from the previous, i.e. it shows a high weight loss ($0.17 \pm 0.5\%$, not reported), even higher than the simple hydroxyapatite-containing sample ($HA_{1.67}$). As already declared, further TGA/DTA analysis should be performed.

9.10 Crystallinity degree

The crystallinity degrees calculated as described in section 5.2.5 for the Sr-F codoped powders are reported in table 9.10.1. In the analysis of values it must be taken into account that the presence of β-TCP can influence the real value of $V_{112/300}$ in the 5.11 equation.

Sample label	X_C**(%)**	***K*** **(a.u.)**
0.5Sr0.5F	87.9142	0.09196
1Sr1F	75.8974	0.08346
2Sr1.5F	80.6966	0.09971
5Sr2F	85.6434	0.07616
0.5Sr2F	89.2808	0.09821

Table 9.10.1: Crystallinity degree of the Sr-F codoped set

As one can see, X_C values are generally lower than the corresponding $FHA_{1.67}$ set. This is most likely due to the presence of the Sr atoms, as already reported by LeGeros and co-workers [57]. In fact, the lowest value is reached when the Sr influence is more important, i.e. in the 1Sr1F sample, in which we've already reported that the content of β-TCP is the highest of the set. For comparison, let's consider the difference between the $FA_{1.67}$ sample crystallinity degree (95%) and the corresponding value of 0.5Sr2F sample (89%). Although the two samples are composed by almost-pure fluorapatite, the decreasing in X_C is important and seems to be attributable only at the Sr presence. The 0.5Sr0.5F, on the other hand, is composed mainly by apatite phase, but the crystallinity degree is slightly lower than the 0.5Sr2F one. This confirms that a fluorine incorporation increases the X_C value, as we already observed.

Chapter 10

Phosphate and fluoride release in acid medium

As described in the 5.3.5 section, the influence of F and Sr doping in the apatite dissolution properties have been investigated here via ion chromatography. At determined time intervals, quotes of 2M nitric acid solution in which 0.1±0.0001 g of product was immersed have been collected, and the corresponding chromatograms have been recorded with the general procedure explained in the 5.3 section. An example of the PO_4^{3-} and F^- peaks variation with respect to the immersion time in the acid medium is represented in figure 10.0.1, in the case of $1FHA_{1.67}$ sample.

Ion-release studies resulted to be impossible to obtain on the β-TCP-containing samples, which showed a high solubility rate, caused by the weak resistance of this phase to very acid environments; the complete dissolution of those samples came in less than 30 and sometimes 15 minutes (depending on the β-TCP content), thus the time intervals should be shortened, but this would have introduced important errors in the measures, most of all caused in the uptaking step by the unwanted mixing of the suspension. High α-TCP content in the products led to similar troubles.

Thus, the selected products for anions release studies are the following 4: $HA_{1.67}$ (as reference), $1FHA_{1.67}$ and $FA_{1.67}$ to investigate the role of F^- and 0.5Sr2F to investigate the influence of a weak Sr doping in a fluorapatite sample. The results of this analysis are resumed in figure 10.0.2. The last points of each plot are taken from the complete dissolution of the sample, which has been previously performed for the *x* determination, and conventionally set to 150 minutes. Error bars in the plots represent an overestimated

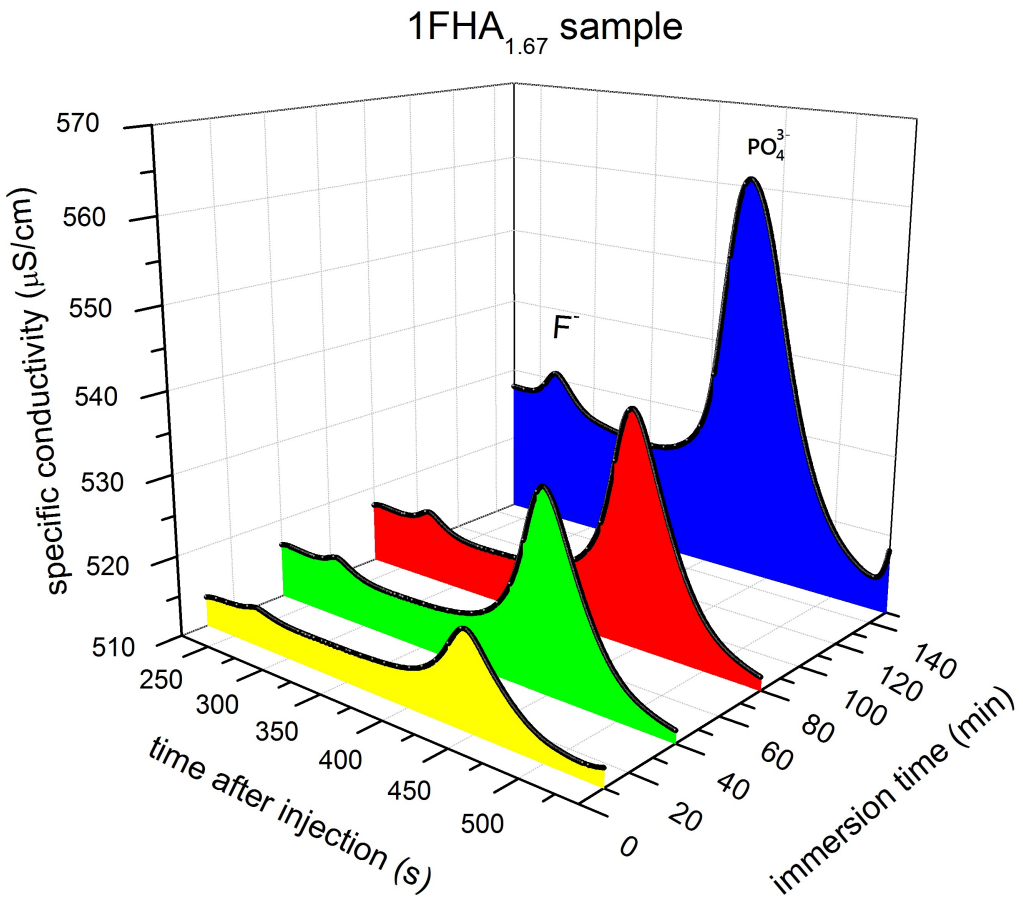

Figure 10.0.1: PO_4^{3-} and F^- peaks height in chromatogram vs immersion time, $1FHA_{1.67}$ sample

relative error of 5% for the ion amount, while the uncertainty on the immersion time is approximately ± 1 min (not shown).

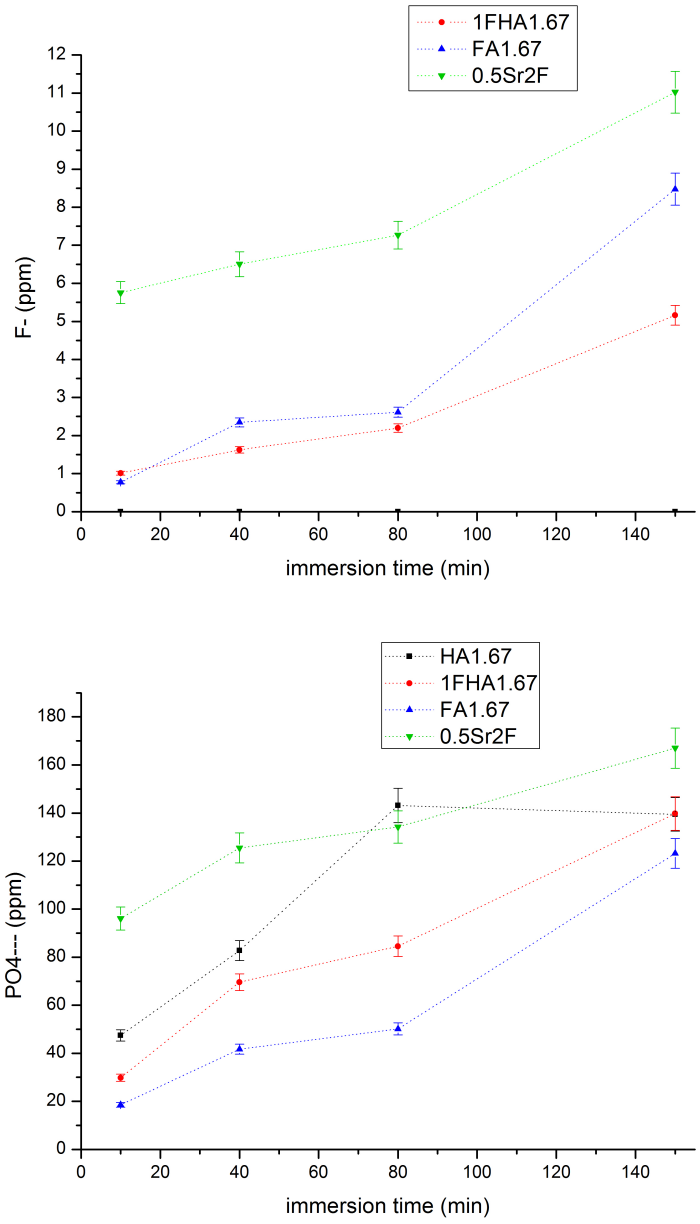

Sample label	SSA (m^2/g)	CDS (nm)
$\mathbf{HA}_{1.67}$	3.352	81
$\mathbf{1FHA}_{1.67}$	0.333	60
$\mathbf{FA}_{1.67}$	0.284	204
0.5Sr2F	6.258	72

Figure 10.0.2: The F^- (up) and PO_4^{3-} (down) release in the acid medium for various samples

10.1 Considerations on the Specific Surface Area

The release of anions, especially of the phosphate one, is a good indication on the material's dissolution rate in the above mentioned conditions. However, one must remember that the specific surface areas of those products are slightly different; for the comfort of the reader, we have reported again the SSA calculated by the BET method in the table inside figure 10.0.2. The coherent domain size is reported too: in fact, the dissolution rate of the material is influenced also by the overall availability of grain boundaries: the more the grain size is reduced, the more the dissolution is accelerated. It's worth to notice also that the PO_4^{3-} amount in the injected solution, in the case of the $HA_{1.67}$ sample, is attributable also to the slight amount of α-TCP.

Because SSA and CDS are different for every sample, no absolute conclusion on the dissolution rate of the samples as a function of F-doping can be drawn. Luckily, even if the *relative* differences of SSA from sample to sample are considerable, the *absolute* variations are not very marked, and most of all, every sample shows very low values of SSA. Anyway, no control on the SSA could be made.

The constant-mass approach has been chosen to assess the effective release of phosphate in the solution starting from the same amount of material, as could happen when an apatite particulate is immersed in the biological medium. Unfortunately, it was not possible to keep the SSA/(solution volume) ratio constant because of the *relatively* high difference among the samples. I.e., from the 0.5Sr2F sample and the $FA_{1.67}$ sample the *absolute* SSA variation is 5.974 m^2/g, but *relatively*, the variation is very high. E.g., the $SSA_{FA_{1.67}}$/(solution volume) is 0.0568 (m^2/g)/mL and the $SSA_{0.5Sr2F}$/(solution volume) is 1.2516 (m^2/g)/mL, that is 22 times higher. Thus, to keep this ratio constant, one should whether increase the $FA_{1.67}$ initial amount of 22 times, or decrease of 22 times the initial amount of 0.5Sr2F, but this would mean to have either a saturation of the solution or a too weak signal in the chromatogram. One could object that the initial 0.1 g amount provides a different molar concentration in every sample, because of their different molar mass. However, the difference in molar mass of those samples is so small that this discrepancy is fully included in the uncertainty of the method.

10.2 Data interpretation according to the dissolution mechanism suggested by S. V. Dorozhkin

First of all, one can observe a general decrease of the phosphate ion release, i.e. of the overall dissolution of the product when the F content increases. Particularly, the hydroxyapatite sample ($HA_{1.67}$) reaches the complete dissolution after about 80 minutes of immersion. All of this confirms the results found by Zhu and co-workers [105] in neutral pH conditions. Because the specific surface area is decreasing, in order, from the $HA_{1.67}$, to the $1FHA_{1.67}$ and $FA_{1.67}$ samples, the influence of this latter parameter on the data cannot be separated from the contribute of the fluoride ion. However, one can observe that SSA values of $1FHA_{1.67}$ and $FA_{1.67}$ samples are quite similar, thus their influence on the PO_4^{3-} release can be most likely neglected. The 0.5Sr2F shows that a low content increase of Sr in the synthesis of fluorapatite provides a quite higher increase of phosphate release rate. This result, obtained again with different pH conditions, is confirmed by Pan and co-workers [75], and by Christoffersen and co-workers [13] in the case of hydroxyapatites. In the 0.5Sr2F sample, anyway, the SSA contribution is more important.

Many works about the apatite dissolution mechanisms description have been published by S. V. Dorozhkin [18, 19]. After reviewing many proposed dissolution models, Dorozhkin suggests a "general dissolution mechanism" [20]. According to him, at least three *levels of investigation* should be considered: milli and micro-levels take into account the grain and the particle dissolution mechanisms as a function of many parameters (shape, sites of preferential attacks, etc...). The nanolevel of investigation describes the dissolution mechanism of the crystal lattice according to the unit cell properties. In the present work, exerting no control on particle size and shape, we focused on the nanolevel features, and the further description is founded on the cited publications.

Briefly, according to Dorozhkin's model, since the X^- anions in the apatite lattice (i.e., OH^- or F^-) are located in hexagonal channels parallel to the *c* axis, in the outer part of the apatite unit cell, these are easily subjected to substitution and generally more removable than other ions. The process of dissolution starts here, then the inner Calcium or Strontium cations located in specific "kink sites" are detached by the anions provided by the acid solution, and finally they diffuse along the surface before entering in the solution. Afterwards, the phosphate-remaining lattice begins to dissolve.

As we will discuss later, another mechanism reviewed by Dorozhkin predicts that the dissolution is initiated by a proton attack (in acidic conditions) of the weakly-bonded phosphate in the edges and corners of the unit cell.

It seems clear than both the initial detachment of the X^- anions and the weakly-bonded phosphate groups attack are restrained by a decrease of apatite lattice parameters, because those anions are closer to the cation sites, and their removal is disturbed by the electrostatic interaction. Since the F substitution for OH, as fully demonstrated, provokes indeed a decrees of the *a* parameter, the overall dissolution rate should be decreasing, in order, when considering the $HA_{1.67}$, $1FHA_{1.67}$ and $FA_{1.67}$ samples. The trend showed in the figure 10.0.2 plots agrees quite well with these observations, being aware, as already declared, that the decreasing of the SSA value is playing the same role. Let's take into account the very limited SSA variation from the $1FHA_{1.67}$ and the $FA_{1.67}$, and observe the clear difference in the PO_4^{3-} release trend vs immersion time. Since this difference is very similar to the one observed between the PO_4^{3-} release by the $1FHA_{1.67}$ and the $FA_{1.67}$ sample, one could infer that the SSA contribution on the acceleration of the dissolution rate in these strongly acid conditions is quite restrained, or at least more restrained than in neutral conditions[1].

In the same way, a slight Sr content produces an increase of the lattice parameters, especially the *c* one, which remains normally almost unvaried by the insertion of F (e.g. $c_{0.5Sr2F} = 6.90$Å, $c_{FA_{1.67}} = 6.88$Å). Thus, the opposite conclusions can be drawn when Sr is inserted in the apatite lattice: an acceleration of the dissolution results. Here, anyway, the relatively much higher SSA cannot be neglected.

The Fluoride release is finally influenced both by the dissolution rate of the product, and by the real F-content of the product. For this reason, the initial F-release by the $1FHA_{1.67}$ sample is higher than the one by $FA_{1.67}$ sample, even if the F-content of the first is lower than the second.

10.3 Stoichiometry considerations

Dissolution models for the apatites can be split into two categories. Some predict a stoichiometric/homogeneous dissolution, i.e. the Ca^{2+}/PO_4^{3-}, and eventually F^-/Ca^{2+} and

[1] Because the dissolution rate is already accelerated by the very low pH.

F^-/PO_4^{3-} molar ratios are constant (and equal to the stoichiometric ones) when considering the dissolution time. If this is the case, a simple leaching of the product followed by the standard ion chromatography characterization could be sufficient to calculate the real value of the *x* in the FHA formula: in fact, the *x* value is simply calculated by the F^-/PO_4^{3-} ratio. In figure 10.3.1 the evolutions of the *x* value in the FHA formula vs immersion time in acid medium for the $1FHA_{1.67}$, $FA_{1.67}$ and 0.5Sr2F samples are plotted.

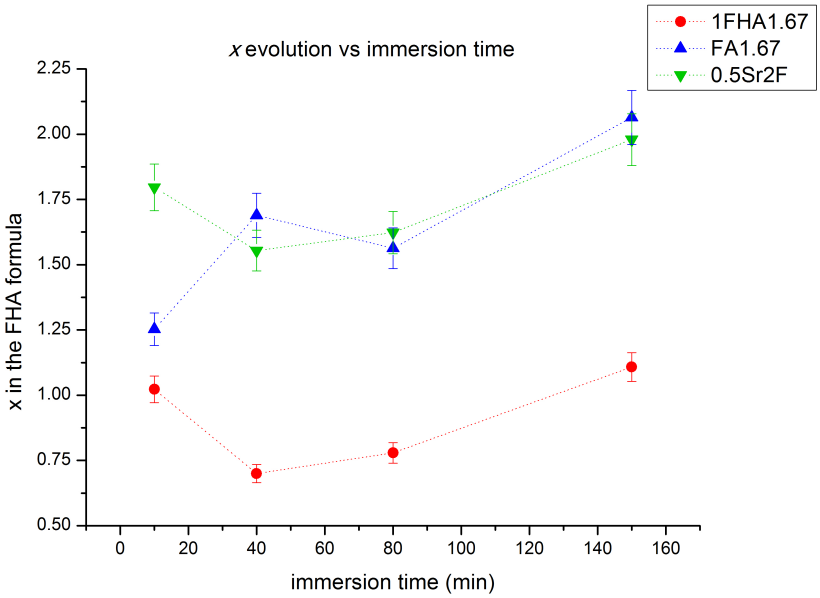

Figure 10.3.1: Evolution of the *x* value in the FHA formula vs immersion time in acid medium

These general considerations can be stated: in general, the dissolution is not stoichiometric, and the real *x* value is reached only when complete dissolution is achieved, thus it was not possible to calculate it by a simple leaching. The F^-/PO_4^{3-} ratio is never higher than the nominal one, in contrast with the observations, reported by Zhu and co-workers [105] in neutral pH conditions. If the above described model is correct, an initial outcoming of F^- anions should precede the release of phosphate groups, thus the *x* values should be initially higher than expected. It's likely that to appreciate this initial outcoming and the resulting over-nominal increase of the calculated *x*, measurements at reduced immersion time intervals should be performed (e.g. at *t*=1 min).

The dissolution behavior in strong acid media is not yet completely clear. Dorozhkin

himself [20], suggests also a preferential crystal edges and corners attack by the protons. Since edges and corners of apatite consist mainly of phosphate, the beginning of the dissolution could be explained by the proton attack of these weakly bounded groups (reported also by Zhu and co-workers), as mentioned in the previous section. This could explain the generally higher PO_4^{3-} content with respect to the F^- content observed in the data.

Anyway, the F^-/PO_4^{3-} ratio do not show an homogeneous variation when considering the three samples. Particularly, for the $1FHA_{1.67}$ and 0.5Sr2F samples the initial *x* value is very high, close to the nominal one, then a slight decrease occurs, and finally the nominal value is reached. We'll call this a "U" trend. The first point of the $FA_{1.67}$ plot disagrees with the other samples general trend, but it's worth to notice that for very small peaks of F^-, the peak-height calculation of the anion amount could generate most likely an underestimation of the real F content and so, error bars higher than the above declared $\pm 5\%$ relative error need to be considered[2]. If this "U" trend would be confirmed by more detailed measurements, the following conclusions could be drawn: initially, the *c* axis channel is definitely etched and F^- anions are released. This should be observed, as declared before, only for immersion times less then 10 mins. Then, the edge and corner mechanism begins to operate and phosphate groups are massively released. Finally, at the end of dissolution, the F^-/PO_4^{3-} ratio is forced to reach the nominal value. In the above introduced data, we're probably observing just the final part of this trend. The same trend should be recorded for the $HA_{1.67}$ when considering the OH^-/PO_4^{3-} ratio, but the pH-meter used in the present work was not suitable for a quantitative measurement of the real OH^- concentration. After this, as already declared above, it must be taken into account the milli and micro-aspects of the dissolution mechanism, which can still modify the anions release process.

Further characterizations in neutral pH environments should then be performed to understand the behavior of F-doped apatites in a saliva-like medium.

[2]For the reader's interest, we declare that if a small underestimation of 0.225 ppm of the F content is made in the case of the $FA_{1.67}$ sample, a huge difference in the 10-minutes calculated *x* would result, and the final *x* value would jump from the reported 1.25 to 1.62, and this would quite agree with the general trend.

Chapter 11

Aqueous solution fluorination

For the experimental details about the procedure adopted to convert hydroxyapatite powders in fluorapatite by means of an aqueous solution fluorination[1], see section 4.5. The fluorinated samples were characterized with the XRD/Rietveld refinement technique. The ion chromatography technique revealed to be more difficult to apply because of the low solubility of those products, the cause of which is object of investigations.

11.1 Samples with Ca/P=1.67 nominal ratio

As described before, two samples with nominal Ca/P molar ratio equal to 1.67 have been fluorinated: the first (named B-1.67) moves from powders which were previously calcined at 900°C for 4h, and just a 102.5°C drying has been performed over it. In the second case, A-1.67, a 900°C calcination followed the aqueous solution fluorination. This latter sample is very similar to the one reported by Geetha and Buvaneswari [30], who used a round flask to dissolve a stoichiometric amount of NH_4HF_2 in 50 mL of water, allowed the solution to stand for 1 day, then after filtration the product was dried and heated up to 900°C for 1h. Surprisingly, they found out a very small value of the *a* parameter, i.e. 9.344 Å. This value is much smaller than the one calculated by the refinement of the $FA_{1.67}$ sample, and has no references in literature. Moreover, the authors declare that no complete fluorination has been achieved.

[1] Both the terms "fluoridation" and "fluorination" are acceptable and known in literature, but this latter is much more diffused. In the present work, both will be used, with a clear preference for the second one

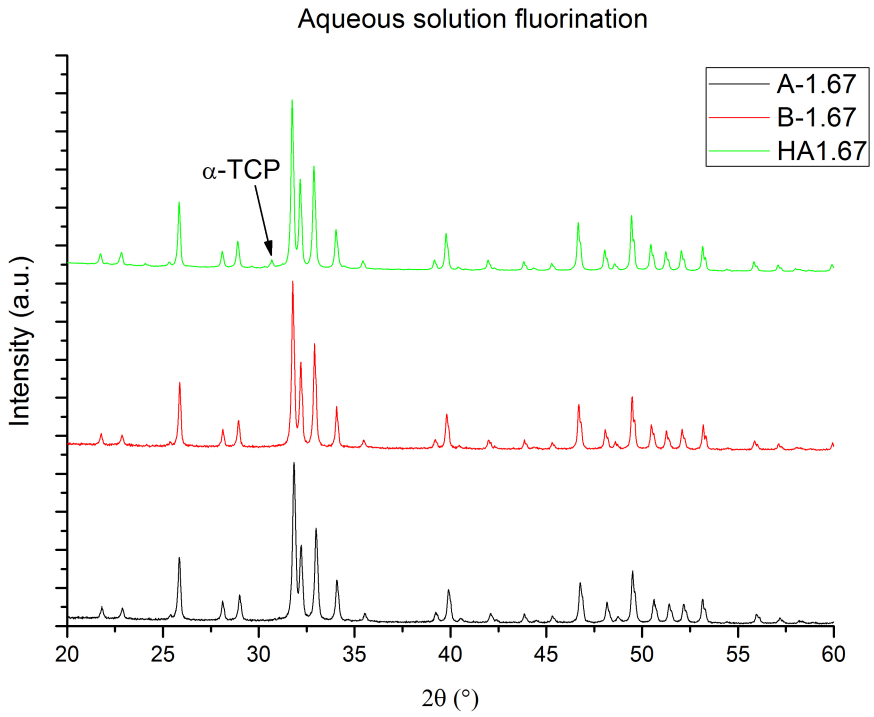

Sample label	a (Å)
$HA_{1.67}$	9.4195
A-1.67	9.3934
B-1.67	9.4197

Figure 11.1.1: XRD patterns of aqueous solution-fluorinated samples with nominal Ca/P=1.67

The XRD analysis of those samples are shown in figure 11.1.1. The first result to stress is that the α-TCP content found in the $HA_{1.67}$ sample is completely disappeared after the water fluorination treatment, in both samples. Thus, pure apatite phase is obtained. In both samples, a slight decrease of the coherent domain size has been observed, since CDS is about 60 nm for both A and B-1.67 samples, when it was about 80 nm for $HA_{1.67}$.

The B-1.67 sample refinement reveals that the *a* lattice parameter, as reported in the figure 11.1.1 inset table, is very very similar to the one of pure hydroxyapatite ($HA_{1.67}$) i.e. no fluorination of the sample has been obtained, nor even in a surface layer (as predicted,

for example, by N. de Leeuw [54]). This contrasts with the results published by Tanaka et al. [92] and by Rodriguez-Lorenzo and Gross [84]. This discrepancy is most likely due to the lower pH used by the latter authors, and by the higher F^- concentrations used by the first author. Particularly, Tanaka and co-workers show that F^- uptaking by HA starts from high concentration values of fluoride precursor (e.g. 0.02 M). In the present work, a stoichiometric F/HA ratio has been used to try to obtain pure fluorapatite. Moreover, we decided not to use support electrolyte, in order to mimic an oral environment, differently from Rodriguez-Lorenzo and Gross, after McCann [64]. Muller and co-workers [72] found that the penetration depth of F^- ions is very limited, much more than previous literature reported values, and they still operated with pH conditions lower than the ones of this work.

Although no complete dissolution was obtained, the ion chromatography analysis of an aliquot of acid medium in which the B-1.67 sample was immersed, confirmed this hypothesis because no F^- has been detected in it, even after long immersion times. This experimental set-up tried to imitate the oral environment to understand the possibility of a F-enriched layer to be formed over an hydroxyapatite product, for an enamel-like application. According to our results, more efforts should be made to improve the fluorination mechanism. When similar experiments are performed over enamel samples, a better F^- penetration seems to occur [96].

In the A-1.67 sample, probably more energy has been left to the fluoride ion to diffuse during the calcination process which follows the fluorination, so it can reach the bulk of the material to form fluorinated-hydroxyapatite. We must remember that the pre-calcination product is an almost-amorphous Ca phosphate, and thus the F^- ion enters in the apatite lattice when the calcination is performed. It seems also that a fluorapatite layer is not formed on the surface of the hydroxyapatite grains, otherwise one should find two distinct phases on the XRD patterns (HA and FA), or, in the case of low-resolution measurements, at least a broadening of the peaks should be noticed. According to the *a* value, the product obtained should have the chemical formula $Ca_{10}(PO_4)_6(OH)_{0.91}F_{1.09}$. Unfortunately, no ion chromatography data could have been collected to confirm this value, but as we demonstrated before for the $FHA_{1.67}$ set, the Vegard's law linear regression is a quite reliable technique to assess the *x* value in the formula. As published by Geetha and Buvaneswari, complete fluorination, i.e. the complete conversion of hydroxyapatite in fluorapatite, was not reached, probably because of the low interaction time (24h), and most likely because a much higher

concentration of F^- is required to have a chemical gradient strong enough to force F^- ions to enter in the apatite lattice. In fact, since the initial F/HA value has been calculated in order to have a final *x*=2 (i.e. fluorapatite), the final *x*=1 calculated value seems to suggest that fluoride is partitioned half in the solution and half in the crystal lattice. After some adjustment, this technique could provide the obtaining of F-controlled enriched fluorapatites.

11.2 Samples with Ca/P=1.50 nominal ratio

The A-1.50 and B-1.50 fluorinated samples have been obtained with the procedure stated before in section 4.5, and the resulting XRD patterns are reproduced in figure 11.2.1. For comparison, the fast XRD characterization of a $HA_{1.50}$ sample, treated for 24h in pure water and then dried is reported inside the same figure, labelled "TCP24h".

The first observation is dedicated to the apatite phase stabilization in both the A-1.50 and B-1.50 samples. Because this stabilization is not observed in the TCP24h sample, this means that the formation of apatite is due to the fluoride presence in the aqueous medium and not simply to the water treatment.

The Rietveld refinement of these two samples have been performed and data are resumed in table 11.2.1. For the determination of the Ca/P value starting from the mass composition, the same procedure adopted for the previous samples have been used.

	Mass fraction (%)					
Sample label	**Apatite**	**β-TCP**	**α-TCP**	**$Ca(OH)_2$**	**CaO**	**estimated Ca/P**
A-1.50	92.43	-	7.51	-	0.05	1.6690
B-1.50	93.46	6.51	-	0.03	-	1.6660

Table 11.2.1: Rietveld refinement data of A-1.50 and B-1.50 samples

These samples do not show a pure apatite phase composition. For a pie-chart overview, see figure 11.2.2, in which are reported, for the reader's comfort, also the mass composition of $HA_{1.50}$ and $FA_{1.50}$ samples.

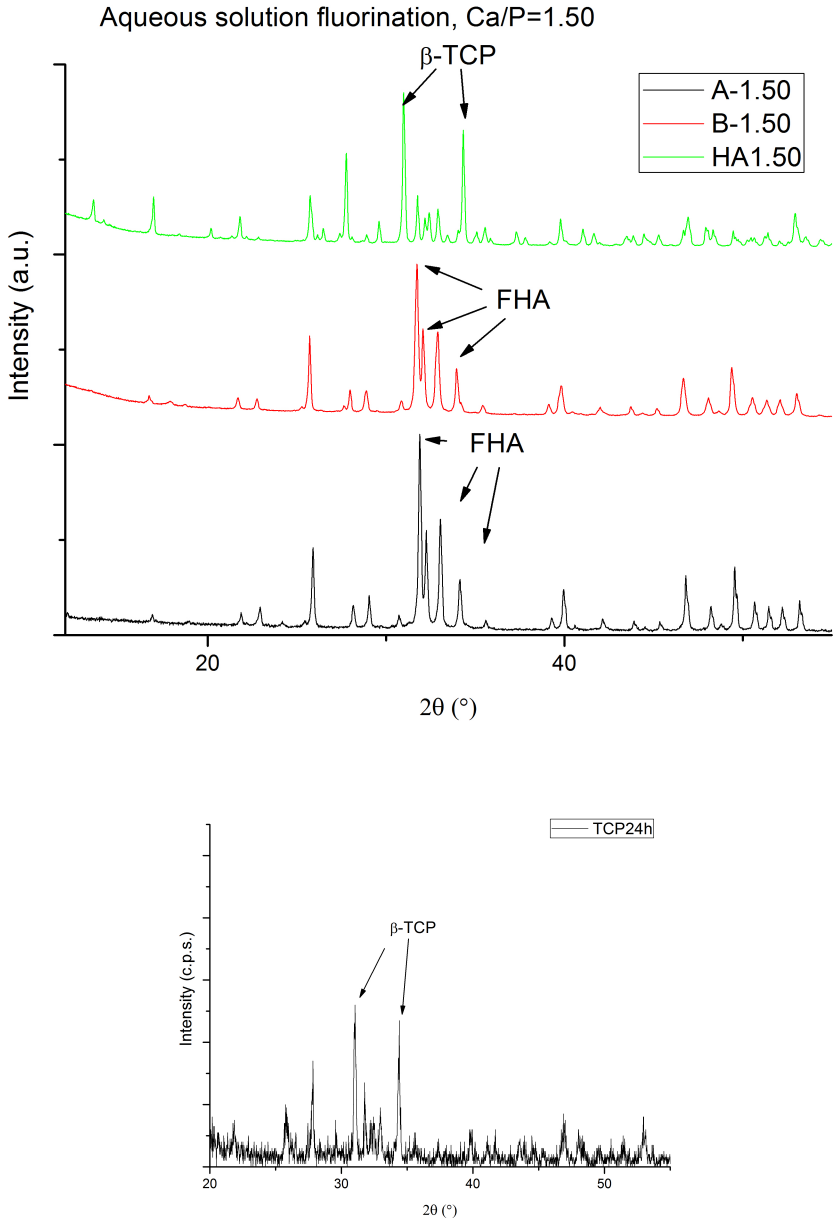

Figure 11.2.1: XRD patterns of aqueous solution-fluorinated samples with nominal Ca/P=1.50

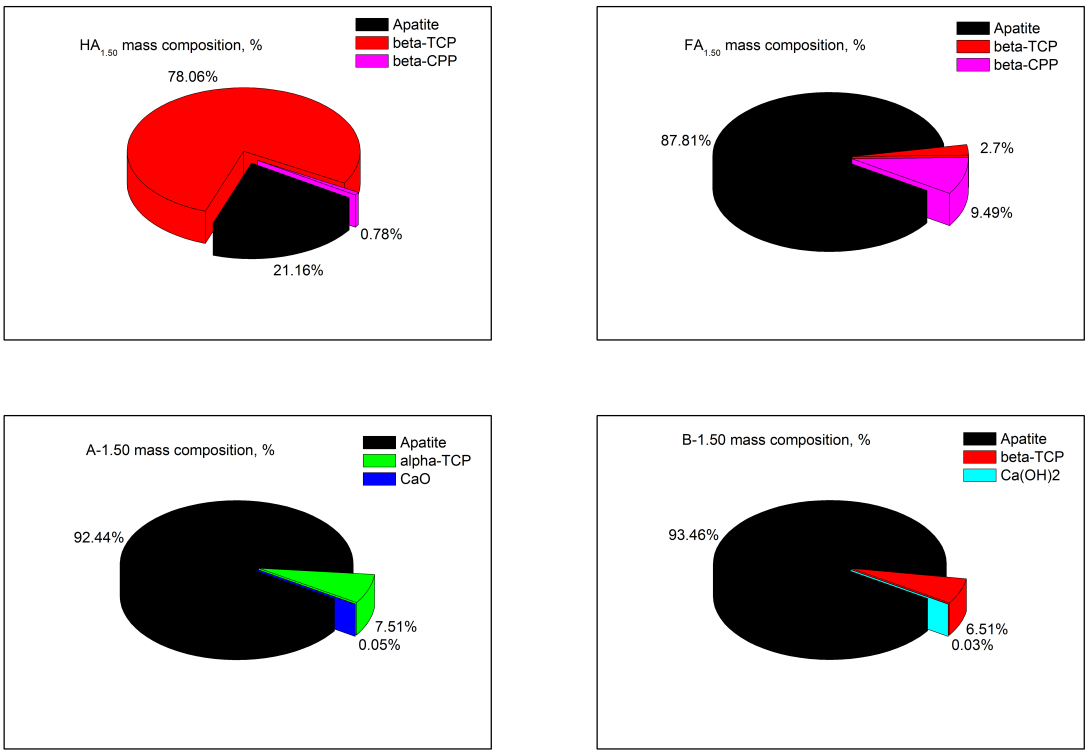

Figure 11.2.2: Pie-chart view of phase composition of $HA_{1.50}$, $FA_{1.50}$, A-1.50 and B-1.50 samples

11.2.1 B-1.50

The B-1.50 sample is resulted to be composed mainly by apatite phase, but a residual 6.51% of β-TCP is left. Moreover, a small amount of portlandite ($Ca(OH)_2$) is found. With respect to the $HA_{1.50}$ sample, from which the B-1.50 sample is derived, one can easily see that no β-CPP is found. The apatite phase content is then extremely increased. We remember that this sample has been just dried at 102.5°C after the fluorination, and no further calcination has occurred. This means that the formation of apatite is promoted by F^- ions even without heating up to 900°C, differently from the previously mentioned B-1.67 sample. So, the high β-TCP content of the pre-treated sample is driven to dissolve in pure water by the F^- ions presence, and then precipitate as fluoridated-hydroxyapatite. Without fluoride, as in the TCP24h sample, no conversion is observed. As one can see, the calculated Ca/P molar ratio is very close to the apatite's one, and much higher than

the starting nominal value of 1.50. Thus, phosphate groups are supposed to be released and left in the fluoride-containing solution. The content of fluoride in the B-1.50 product have been calculated via ion chromatography, although it was not possible to obtain the complete dissolution of the sample, the causes of which need yet to be investigated.

β-TCP is known to be transformed in hydroxyapatite when in contact with biological fluids, or with the simulated body fluid (SBF) [95]. The conversion in a neutral-pH environment enriched with fluorine, however, could provide more indications about the employment of this product in oral applications. Not so much work, as far as we know, has been done in this sense. Sakamoto and co-workers [86, 87], who gave a great contribution in this field, used a procedure similar to the one described in this work to obtain fluorapatite moving from β-TCP and/or α-TCP containing powders. They suggest a "cluster model" to clarify both the α and $\beta-$TCP forms transformation in apatite phase, but no further description of these clusters are given, and a general $10Ca_3(PO)_2+(3x)NH_4F \rightarrow 3Ca_{10}(PO_4)_6(OH)_{2-x}F_x+x(NH_4)_3PO_4$ reaction is supposed to be followed. This reaction explains the loss of phosphates in the fluoridating solution, and the resulting increase of the Ca/P molar ratio. As far as we know, no complete conversion has been reached by any author, but a residual β-TCP content is always observed. The *x* value estimated by ion chromatography is 1.636, thus a good incorporation of fluoride has been achieved. Rietveld refined lattice parameters of the apatite fraction contained in the B-1.50 sample confirm this value, as showed in table 11.2.2.

Sample	**a [Å]**	**c [Å]**	**unit cell volume [Å^3]**	***x* calculated from Vegard's linear regression**	***x* from ion chromatography**
B-1.50	9.38473	6.88074	524.819	1.529	1.636

Table 11.2.2: Refined lattice parameters of B-1.50 sample, and calculated *x* in FHA formula

The *x* has been calculated via linear regression of the *cell volume* parameter according to the Vegard's law starting from the data of pure hydroxyapatite and fluorapatite found in the $HA_{1.67}$ and $FA_{1.67}$ samples, respectively. The so obtained value is very close to the ion-chromatography provided one. According to Sakamoto et al., when hydroxyapatite precipitates as explained, a weak carbonation of the product is possible, caused by the carbonate content of the water. This means that a CO_3^{2-} ions replace PO_4^{3-} with a charge

unbalance that is balanced by a loss of 1/2 mole of Ca^{2+} ions. Those ions can easily combine with OH^- groups to form portlandite. Although Sakamoto and co-workers do not declare the detection of this phase, we performed the refinement of Ca1 and Ca2 occupancy factors, and found out an increasing from 0.33333 to 0.33650 for Ca1 and a decreasing of Ca2 from 0.5 to 0.49657. The sum of the two is 0.83307 instead of the nominal 0.83333 (i.e. 99.969% of sites are occupied with respect to stoichiometric HA), thus an outcome of Ca atoms from the lattice could be fully justified. Because of the very small amount of portlandite, we think that this phenomenon had most likely no significant influence on the lattice parameters, and previous estimations of the *x* value remain valid.

11.2.2 A-1.50

In the A-1.50 sample, no β-TCP is found, but a 7.51% of α-TCP is detected. Let's remember that this sample moves from pre-calcination fluoridated Ca/P=1.50 powders, which are then heated up to 900°C. This suggests that the β form of TCP is converted in the α form at the 900°C temperature when a considerable amount of apatite phase forms, like we've already underlined in the $FHA_{1.67}$ set. Apparently, the presence of fluoride ions in the pre-calcination powders leads to a different crystallization in the calcination step: the Calcium phosphate in the almost-amorphous form tends to crystallize in the apatite and α-TCP form. Normally, this phase is stable at temperature above 1125°C. The role of fluoride ion on the stabilization of this form should be investigated with further synthesis.

The amount of lime is quite similar to the one of portlandite observed in the previous sample, and similar conclusions can be drawn; indeed the overall Ca occupancy factor is 0.83194, i.e. the 99.833% of the sites are stoichiometrically occupied[2]. It seems obvious that lime is found because portlandite to lime transition temperature is below 900°C. Table 11.2.3 gives an overview on the Rietveld refined cell parameters of the apatite phase contained in the A-1.50 sample, and the *x* values have been calculated by the two methods indicated above.

As one can see, both the methods describe the formation of a half-substituted product (i.e. $Ca_{10}(PO_4)_6(OH)F$). The F^- incorporation is thus less emphasized than before, although the same quantity of NH_4F has been added in the solution. But since the initial

[2]This value is a bit smaller than before, and in fact the final lime content is slightly higher than the previous sample portlandite one.

Sample	a [Å]	c [Å]	unit cell volume [Å^3]	*x* calculated from Vegard's linear regression	*x* from ion chromatography
B-1.50	9.39253	6.88473	525.997	1.067	1.013

Table 11.2.3: Refined lattice parameters of A-1.50 sample, and calculated *x* in FHA formula

product is an almost-amorphous calcium phosphate, it was not possible to exactly calculate the real F/HA ratio. Figure 11.2.3 shows the plot of the apatite cell volume vs the *x* calculated via ion chromatography, and the good agreement with Vegard's law is confirmed.

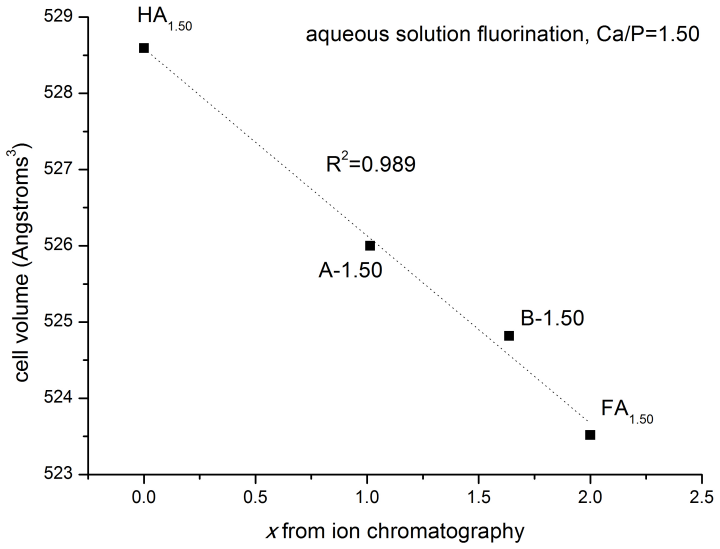

Figure 11.2.3: The apatite cell volume parameter vs F content in the apatite lattice, aqueous solution fluorination Ca/P=1.50 set

11.3 Crystallographic aspects

It's worth to notice that all the samples obtained through the aqueous solution fluorination method do not show significant differences, from the microstructural point of view, with the analogous samples obtained through the "one-step method". Table 11.3.1 resumes the

coherent domain size and the crystallinity degree, calculated as described above, of the mentioned samples.

Sample label	CDS (nm)	$X_C(\%)$	K (a.u.)
A-1.67	66	89.63	0.0940
B-1.67	76	91.44	0.0848
A-1.50	76	89.46	0.0894
B-1.50	93	85.23	0.0768

Table 11.3.1: CDS and crystallinity degree (with correlated *K* value) of the aqueous solution fluorinated samples

First of all, crystallinity degree of the Ca/P=1.67 samples results to be almost the unvaried with respect to the corresponding $FHA_{1.67}$ set. As we declared before, in fact, the A-1.67 sample is composed manly by an hydroxy/fluorapatite half-substituted, and once we compare its X_C with the one of $1FHA_{1.67}$ sample, we can easily see that the difference is minimal. The CDS values of the two mentioned samples are also very close. This means that no particular influence in the crystallographic behavior is provided by the synthesis method. The same observation can be done on the B-1.67 sample, which corresponds to a pure hydroxyapatite phase, and which can be fully compared to the $HA_{1.67}$ sample ($CDS_{HA_{1.67}}$=80 nm, X_C=90%).

The A-1.50 sample should be compared instead to the $1.5FHA_{1.67}$ sample, and in fact both its X_C and CDS values are close to the ones of that sample.

Surprisingly, even the B-1.50 sample, which contains β-TCP-transformed apatite precipitated in aqueous solution, show a quite high crystallinity degree. Thus, more detailed tests should be performed to attribute this high crystallinity to Fluoride's apatite crystallization capacity.

Chapter 12

Conclusions

The aim of the present work was to investigate the crystallographic properties of F-substituted and Sr-F co-substituted hydroxyapatite nanopowders for potential biomedical applications.

Fluoridated hydroxyapatite series with nominal Ca/P ratio equal to 1.67, 1.50 and 1.28, with nominal fluorine atomic substitution ranging from 0% to 100% have been synthesized by a precipitation method in aqueous solution, followed by a heat treatment up to 900°C. Samples were characterized by X-ray diffraction and Rietveld refinement to assess their structural properties, such as phase composition, lattice parameters, coherent domain size, and cristallinity degree. An original ion-exchange chromatography characterization method has been developed to calculate the fluoride incorporation in the product, i.e. the *x* value in the $Ca_{10}(PO_4)_6(OH)_{2-x}F_x$ formula.

Powders with nominal Ca/P molar ratio equal to 1.67 resulted to be composed mainly by apatite phase (either hydroxyapatite or fluoro-hydroxyapatite), with a slight content of α-TCP in the case of non-doped and lowest-doped samples, most likely due to the basic synthesis conditions. Sample with 100% atomic substitution showed fluorapatite phase together with very small content of lime. Rietveld analysis allowed to calculate the lattice parameters; while the *c* parameter is almost unchanged by the insertion of the fluorine atom in the hydroxyapatite lattice, the *a* parameter shows a linear decrease when the F content in the product increases. This result agrees fairly well with the Vegard's law and the current literature. The fluorine amount in the apatite cell has been calculated both by linear regression of the Vegard's law (using either the refined a lattice paramater or cell volume data) and by ion-exchange chromatography, which allowed to confirm the presence of the F^- ion

in the product. Both the techniques returned converging results in determining the above mentioned *x* value. Fluorine insertion in hydroxyapatite seems to decrease the apparent coherent domain size except for the pure fluorapatite product, which shows a mean CDS much higher that the other samples. This is most likely due to fluorapatite's lower activation energy barrier for grain growth, as suggested by other authors. Gas-adsorption specific surface area measurements reveals that synthesized products are basically non-porous; the weighting of the products before and after the heat treatment showed a general improvement of thermal stability of hydroxyapatite when F^- ion is incorporated, in agreement with other authors results. Crystallinity degree has been calculated with the method suggested by Landi et al. [52]. A general high level of crystallinity (approx. 90%) has been found, the highest value being recorded on the fluorapatite sample (approx. 95%), which confirms that this sample behaves differently from the others from the microstructural point of view.

Powders with nominal Ca/P molar ratio equal to 1.50 have been synthesized to assess fluoride ion's skill in apatite phase stabilization. The phase composition evolution of the samples as a function of the nominal F content in the product confirmed that a fluorine-enriched hydroxyapatite ($x \approx 1.7$-2) is stabilized even at low F-doping levels, while the β-TCP content decreases as the F-doping increases. The overall Ca/P ratio is balanced by the formation of β-$Ca_2(P_2O_7)$ phase. No α-TCP phase has been detected. The insertion of F in the Ca/P=1.50 powders could then be a good method to tune the apatite and β-TCP content in biphasic calcium phosphate ceramics for biomedical applications, after having developed a procedure to eliminate the residual β-$Ca_2(P_2O_7)$. CDS, SSA and weight loss upon calcination analyses confirmed the results reported for the first set of fluorinated-hydroxyapatite powders. Even with lower values of nominal Ca/P molar ratio (1.28) the F-rich apatite phase stabilization is shown but no further characterizations have been performed on these samples.

Sr-F co-substituted hydroxyapatite series has been synthesized with the so-called "diagonal" codoping, i.e. as Sr content increases, F content increases too. Nominal (Ca+Sr)/P molar ratio was set to 1.67. Since Sr in known to stabilize the β-TCP phase, while F, as we said before, tends to make stable the apatite phase, this kind of synthesis allowed to investigate the effects of the contemporary double doping in the phase composition. At low levels of F and Sr doping, the apatite phase is quite stable, with the presence of both α and β-TCP as secondary phases. For a 50% atomic F for OH substitution with a 10% atomic Sr for Ca substitution, apatite results to be less stable and an important dose of β-TCP is

found. When F doping increases, even with a huge Sr doping (up to 50% atomic) apatite is again the main phase detected in the samples. The Sr ion size being bigger than the Ca one, the unit cell volumes of the two TCP forms increase linearly when Sr is added in the synthesis solution, in fair agreement with the Vegard's law. On the contrary, apatite unit cell volume did not show linear variation because of the opposite effect of fluoride: this confirms that F is hosted just in the apatite lattice and not in other phases. For a full F for OH substitution, apatite is highly stable (almost 93% wt.), even with 50% atomic Sr for Ca substitution, and the two TCP forms unit cell volumes result not to increase further, while the apatite cell volume records a huge increase. This indicates that Sr is entering massively in the apatite lattice when apatite phase is highly stabilized (this corresponds to a huge F doping), otherwise Sr is hosted preferentially in the TCP lattice. Since (Ca+Sr)/P molar ratio calculated from the Rietveld refinement mass composition is less than the nominal 1.67 because of the presence of TCP, the formation of a Ca,SrO amorphous phase, undetectable by XRD and already reported in previous literature is supposed to occur. The refinement of the occupancy factors of Sr and Ca sites in apatite lattice confirms this hypothesis: Sr overall O.F. is never as high as expected if the nominal substitution would be respected; however, as the apatite phase becomes more stable, the overall Sr O.F. comes close to the nominal one. The Sr which is not entering in apatite lattice is thus supposed to be hosted in the amorphous phase. The same refinement confirms the tendency of the Sr atoms to occupy preferentially the Ca2 6h site, which allows the bigger Sr^{2+} ion to be hosted thanks to a slide of the O4 centers (occupied by OH groups or F atoms) outwards along the z axis. As observed in the previous Ca/P=1.50 fluorinated powders samples set, when a huge amount of TCP is formed, the remaining apatite fraction is particularly F-enriched, i.e. the x values calculated by ion chromatography are higher than the nominal ones. The synthesis of a full-F/low-Sr substituted apatite sample provided a pure fluorapatite product with approx. 3.6% atomic Sr for Ca substitution, most likely together with an amorphous fraction of Ca,SrO phase. Specific surface area values of all the Sr-F co-substituted samples are generally higher than the corresponding Ca/P=1.67 fluorinated powders set, although the samples can be still considered as non-porous; the CDS values do not show an obvious trend with the doping, and no significant differences with the corresponding non-Sr-substituted samples is observed. Crystallinity is generally lower than the previous sets, especially when Sr influence is higher (e.g. when apatite phase is less stable); the effect of decreasing the degree of crystallinity by Sr doping has been already observed by

other authors. Sr and F co-substitution can thus be tuned to obtain controlled-composition biphasic calcium phosphates with improved biological activity for bone scaffolds, bone grafts, dental protheses or other bone replacement devices.

The release of F^- and PO_4^{3-} ions in 2M nitric acid solution by F-doped samples has been studied as a preliminary investigation of the substituted hydroxyapatite dissolution rates at very low pH values. Those conditions have been selected to accelerate the testing time, and a constant-mass approach has been used. Although SSA values of different samples are not identical, they are similar enough to conclude that the presence of fluoride in the hydroxyapatite lattice helps to slow down the release of phosphate from the samples; this can be attributed to the decrease of the *a* unit cell parameter length when inserting F atoms in hydroxyapatite lattice, as confirmed by previous literature results. The low Sr-substituted fluorapatite sample showed higher phosphate release rate, but the contribution of the higher SSA value cannot be separated from the one given by the Sr doping. Apatite dissolution is never stoichiometric, i.e. the F^-/PO_4^3 ratio is never constant, and different from the nominal one. The trend of anion release from the samples is explainable according to the model described by S.V. Dorozhkin. Controlling the product's dissolution rate in biological conditions is a powerful instrument to design resorbable bone replacement devices, and since Sr and F have positive effects on hard tissues remineralization, it could be interesting to tune the release of both the ions in the biological environment. To investigate further this aspect, longer neutral-pH dissolution studies should be performed.

Calcium phosphate powders with nominal Ca/P molar ratio equal to 1.50 or 1.67 have been immersed in aqueous solutions containing F^- ions, in neutral pH conditions, at T=37°C, to investigate the possibility of an "aqueous solution fluorination". Calcination of the samples has been performed either before or after the fluorination step. Powders with Ca/P molar ratio equal to 1.67 result to incorporate fluoride, although not in total amount, only if calcination comes *after* the fluorination step, because of the higher energy provided to the F^- ion to migrate inside the apatite lattice. The simple water treatment and following drying at 102.5°C produces the elimination of the secondary α-TCP phase detected in the non-treated sample. When Ca/P=1.50, the β-TCP fraction is converted in F-rich hydroxyapatite phase in every sample. When the treatment is performed with no F^- in the water, no significant TCP to HA conversion is observed in the same conditions. If calcination is performed before the fluorination step, residual β-TCP phase is left, together with low amount of $Ca(OH)_2$, but when calcination is made after fluorination, α-TCP phase is

found, together with CaO. The assessed Fluoride ion's ability to enhance F-rich hydroxyapatite phase stabilization even at neutral pH condition and normal human body temperature could for instance be exploited as dental lesion-filler applications: a TCP-containing product could be placed in the lesion and be subsequently treated with F^--containing solution to convert the phosphate in fluoro-hydroxyapatite, which is known to have better mechanical properties.

We tried to investigate crystal structure and microstructural properties of F and Sr/F-substituted apatites, and this led to the above stated conclusions. Further physico-chemical characterizations could be performed, such as NMR or ICP-AES to have better quantitative analysis of F and/or Sr content in the products, sintering trials (together with DTA/TGA analyses) or mechanical tests to investigate the co-doping effect on monolithic samples, and of course long-time immersions in biological-simulating fluids as the DMEM or SBF. The possibility to control the product's solubility in biological medium is provided by the Sr+F co-substitution, and the biological long-time effects of these atoms in biomedical devices can be an interesting point to investigate in the future.

Part IV

Appendix

12.1 Sample of FullProf control file

```
COMM 'HA Ca/P=1.67'
! Current global Chi2 (Bragg contrib.) =       6.548
! Files => DAT-file: HA,  PCR-file: HA
!Job  Npr  Nph  Nba  Nex  Nsc  Nor  Dum  Iwg  Ilo  Ias  Res  Ste  Nre  Cry  Uni  Cor  Opt  Aut
  0    7    1   50    1    0    1    1    0    0    1    1    1    0    0    0    0    0    0
!
!  Resolution file for Pattern#   1
 res_function.irf
!Ipr  Ppl  Ioc  Mat  Pcr  Ls1  Ls2  Ls3  NLI  Prf  Ins  Rpa  Sym  Hkl  Fou  Sho  Ana
 2    0    1    1    1    0    0    0    0    1    0    1    1    0    1    0    1
!
! lambda1  Lambda2     Ratio     Bkpos     Wdt     Cthm      muR     AsyLim    Rpolarz  ->Patt# 1
 1.540560  1.544390   0.5000     0.000   6.0000   1.0000   0.0000    40.00     0.0000
!
!NCY  Eps   R_at   R_an   R_pr   R_gl      Thmin         Step         Thmax     PSD     Sent0
 20   0.05   0.80   0.80   0.80   0.80     3.0064     0.016711    120.0020    0.000   15.000
!
!2Theta/TOF/E(Kev)    Background   for Pattern# 1
         ...
!
! Excluded regions (LowT  HighT) for Pattern#  1
 3.00          7.00
!
!
      82     !Number of refined parameters
!
!    Zero   Code    SyCos     Code      SySin    Code     Lambda     Code  MORE ->Patt# 1
-0.04578  31.00  0.00000    0.00      0.00000  0.00     0.000000   0.00  0
!---------------------------------------------------------------------------------------
! Data for PHASE number:   1  ==> Current R_Bragg for Pattern#  1:      2.96
!---------------------------------------------------------------------------------------
Hydroxylapatite, Ca5(PO4)3(OH), *data for   ICSD #99358
!
!Nat Dis Ang Pr1 Pr2 Pr3 Jbt Irf Isy Str Furth        ATZ     Nvk Npr More
7    0   0 0.0 0.0 1.0    0   0    0   0    0       1002.620    0   7    0
! P 63/m                    <--Space group symbol
!Atom Typ        X         Y         Z       Biso       Occ      In  Fin  N_t  Spc  /Codes
Ca1   CA       0.33333   0.66667   0.00141   0.66874    0.33333    0    0    0     0
                0.00      0.00     161.00    291.00      0.00
Ca2   CA       0.24648   0.99280   0.25000   0.66874    0.50000    0    0    0     0
               171.00    181.00      0.00    291.00      0.00
P1    P        0.39803   0.36815   0.25000   0.66325    0.50000    0    0    0     0
191.00    201.00      0.00    301.00      0.00
O1    O        0.32747   0.48315   0.25000   0.68389    0.50000    0    0    0     0
211.00    221.00      0.00    311.00      0.00
O2    O        0.58719   0.46541   0.25000   0.68389    0.50000    0    0    0     0
231.00    241.00      0.00    311.00      0.00
```

```
O3    O        0.34170   0.25703   0.06963   0.68389    1.00000    0    0    0     0
251.00    261.00    271.00    311.00        0.00
O4    O        0.00000   0.00000   0.19788   0.68389    0.16667    0    0    0     0
0.00      0.00    281.00    311.00        0.00
!-------> Profile Parameters for Pattern #  1
!  Scale          Shape1        Bov        Str1       Str2       Str3    Strain-Model
 0.89713E-02    0.00000    0.00000    0.00000    0.00000    0.00000         0
      11.00000       0.000       0.000       0.000       0.000       0.000
!       U          V          W          X          Y        GauSiz    LorSiz  Size-Model
   0.001755   0.000000   0.000000   0.000000   0.043181   0.003167   0.000000     0
     801.000       0.000       0.000       0.000     821.000     811.000       0.000
!      a          b          c        alpha       beta        gamma       #Cell Info
   9.419541   9.419541   6.880673  90.000000  90.000000 120.000000
   41.00000   41.00000   51.00000    0.00000    0.00000   41.00000
!  Pref1      Pref2      Asy1       Asy2       Asy3       Asy4       S_L        D_L
  0.99252   0.00000   0.08045   0.03326   0.00000   0.00000   0.00000   0.00000
   101.00      0.00    111.00    121.00      0.00      0.00      0.00      0.00
```

12.2 List of abbreviations

Throughout all the present work, many abbreviations have been used. We report here the most recurring ones here for the reader's comfort.

a.u. = arbitrary units

BCP = Biphasic Calcium Phosphate

BET = Brunauer - Emmett - Teller theory

CDS = Coherent domain size

CPP, DCDP = Calcium pyrophosphate, that is Dicalcium Diphosphate

c.p.s. = counts per step (unit of measurement of XRD patterns intensity)

FA = fluorapatite

$\boldsymbol{x}$**FHA**$_n$ = fluoridated hydroxyapatite with nominal Ca/P molar ratio equal to n and atomic substitution equal to x.

FWHM = Full width at half maximum of a peak

HA = hydroxyapatite

ISCD = FIZ-Karlsruhe Inorganic Crystal Structure Database

JCPDS = Joint Committee on Powder Diffraction Standards

$\boldsymbol{K}$ = Agreement parameter in the X_c formula

O.F. = Occupancy factor

$\mathbf{R}^2$ = linear correlation factor

$\mathbf{R}_{exp}$, $\boldsymbol{c}\mathbf{R}_{exp}$ = Rietveld's expected and background-corrected expected profile factor

R*p*, R*wp* = Rietveld's profile factor and the weighted profile factor

SSA = Specific Surface Area

TCH = Thompson-Cox-Hastings function

TCP = Tricalcium phosphate

χ^2 = Rietveld's function providing the agreement of the fit

X_c = Crystallinity Degree

***y*Sr*x*F** = Sr-F codoped apatites with y=Sr content and x=F content

Acknowledgments

First, I need to thank prof. Jean-Marie Nedelec, who is the co-director of this thesis and who gave me the opportunity to work in the LMI laboratories, providing useful indications in the interpretation of the results and in the editing of this work. Prof. Alessandro Martucci deserves some special thanks for the patience, the availability and the courtesy in directing this work. Prof. Massimo Guglielmi is gratefully acknowledged for the precious final judging of the whole thesis.

I need to thank my "colleagues" (even if I'm not at their high levels) for the great period I spent in Clermont-Ferrand: I met very beautiful and sociable people, and I want to say *merci et a bientôt* to doct. Adéline Hardy-Dessources, doct. Olivier Raissle, doct. Jérémy Soulié. I thank very much also prof. Miroslaw Chorazewski and miss Joséphine Lacroix, together with doct. Sandrine Renaudin who provided me some important advices in the very beginning of my work.

I want to thank very very much Dr. Guillaume Renaudin who was a real guiding light in the hard task of learning and performing the Rietveld refinement all over the work. I thank also the ENSCCF and the LMI staff, particularly Cécile Ésparcieux who gave me a precious help in developing the HPLC procedure, and Joel Cellier who performed almost all the XRD characterization reported in this work.

I want to thank my family who gave me the opportunity to live this important experience.

Bibliography

[1] B. BADRAOUI, A. AISSA, A. BIGI, M. DEBBABI, AND M. GAZZANO, *Synthesis and characterization of Sr(10-x)Cdx(PO4)6Y2 (Y=OH and F): A comparison of apatites containing two divalent cations*, Materials Research Bulletin, 44 (2009), pp. 522–530.

[2] A. BAGNO AND C. DI BELLO, *Interazioni tra biomateriali e tessuti*, Pàtron, 2009.

[3] B. BASAR, A. TEZCANER, D. KESKIN, AND Z. EVIS, *Improvements in microstructural, mechanical, and biocompatibility properties of nano-sized hydroxyapatites doped with yttrium and fluoride*, Ceramics International, 36 (2010), pp. 1633–1643.

[4] C. G. BELLOWS, J. E. AUBIN, AND J. N. M. HEERSCHE, *Differential Effects of Fluoride During Initiation and Progression of Mineralization of Osteoid Nodules Formed In Vitro*, Journal of Bone and Mineral Research, 8 (1993).

[5] J. BEUKENKAMP, W. RIEMAN, AND S. LINDENBAUM, *Behavior of the Condensed Phosphates in the Anion-Exchange Chromatography*, Analytical Chemistry, 26 (1954), pp. 505–512.

[6] A. BIANCO, I. CACCIOTTI, M. LOMBARDI, L. MONTANARO, E. BEMPORAD, AND M. SEBASTIANI, *F-substituted hydroxyapatite nanopowders: Thermal stability, sintering behaviour and mechanical properties*, Ceramics International, 36 (2010), pp. 313–322.

[7] A. BIGI, E. BOANINI, C. CAPUCCINI, AND M. GAZZANO, *Strontium-substituted hydroxyapatite nanocrystals*, Inorganica Chimica Acta, 360 (2007), pp. 1009–1016.

[8] S. BOUDIN, A. GRANDIN, M. M. BOREL, A. LECLAIRE, AND B. RAVEAU, *Redetermination of the β-Ca2P2O7 structure*, Acta Crystallographica Section C, 49 (1993), pp. 2062–2064.

[9] J. BRAUX, F. VELARD, C. GUILLAUME, S. BOUTHORS, E. JALLOT, J.-M. NEDELEC, D. LAURENT-MAQUIN, AND P. LAQUERRIÈRE, *A new insight in the dissociating effect of strontium on bone resorption and formation.*, Acta biomaterialia, (2011).

[10] S. BRUNAUER, P. EMMETT, AND E. TELLER, *Adsorption of gases in multimolecular layers*, Journal of the American Chemical Society, 60 (1938), pp. 309–319.

[11] Y. CAI, S. ZHANG, X. ZENG, Y. WANG, M. QIAN, AND W. WENG, *Improvement of bioactivity with magnesium and fluorine ions incorporated hydroxyapatite coatings via sol-gel deposition on Ti6Al4V alloys*, Thin Solid Films, 517 (2009), pp. 5347–5351.

[12] G. W. CHINTHAKA SILVA, L. MA, O. HEMMERS, AND D. LINDLE, *Microstructural characterization of precipitation-synthesized fluorapatite nano-material by transmission electron microscopy using different sample preparation techniques.*, Micron (Oxford, England, 39 (2008), pp. 269–74.

[13] J. CHRISTOFFERSEN, M. R. CHRISTOFFERSEN, N. KOLTHOFF, AND O. BÄRENHOLDT, *Effects of strontium ions on growth and dissolution of hydroxyapatite and on bone mineral detection.*, Bone, 20 (1997), pp. 47–54.

[14] M. CURZON, *Effects of a combination of strontium and fluoride on dental caries in the rat*, Nutrition Research, 8 (1988), pp. 321–326.

[15] M. DARROUDI, H. ESHTIAGH-HOSSEINI, R. HOUSAINDOKHT, AND A. YOUSSEFI, *Preparation and characterization of Fluorohydroxyapatite nanopowders by nonalkoxide sol-gel method*, 5 (2010), pp. 29 – 33.

[16] A. DENTON AND N. ASHCROFT, *Vegard's law*, Physical Review A, 43 (1991), pp. 3161–4.

[17] L. DESGRANGES, D. GREBILLE, G. CALVARIN, G. CHEVRIER, N. FLOQUET, , AND J.-C. NIEPCE, *Hydrogen thermal motion in calcium hydroxide: Ca(OH)2*, Acta Crystalligraphica B, 49 (1993), pp. 812–817.

[18] S. DOROZHKIN, *Acidic dissolution mechanism of natural fluorapatite. I. Milli- and microlevels of investigations*, Journal of Crystal Growth, 182 (1997), pp. 125–132.

[19] ——, *Acidic dissolution mechanism of natural fluorapatite. II. Nanolevel of investigations*, Journal of Crystal Growth, 182 (1997), pp. 133–140.

[20] ——, *A Review on the Dissolution Models of Calcium Apatites*, Progress in Crystal Growth and Characterization, 8974 (2002), pp. 4–9.

[21] S. V. DOROZHKIN, *Bioceramics of calcium orthophosphates.*, Biomaterials, 31 (2010), pp. 1465–85.

[22] E. D. EANES AND A. H. REDDI, *The effect of fluoride on bone mineral apatite*, Metabolic Bone Disease and Related Research, 2 (1979), pp. 3–10.

[23] H. ESLAMI, M. SOLATI-HASHJIN, AND M. TAHRIRI, *The comparison of powder characteristics and physicochemical, mechanical and biological properties between nanostructure ceramics of hydroxyapatite and fluoridated hydroxyapatite*, Materials Science and Engineering: C, 29 (2009), pp. 1387–1398.

[24] M. FATHI AND E. MOHAMMADI ZAHRANI, *Mechanical alloying synthesis and bioactivity evaluation of nanocrystalline fluoridated hydroxyapatite*, Journal of Crystal Growth, 311 (2009), pp. 1392–1403.

[25] M. H. FATHI AND E. MOHAMMADI ZAHRANI, *Fabrication and characterization of fluoridated hydroxyapatite nanopowders via mechanical alloying*, Journal of Alloys and Compounds, 475 (2009), pp. 408–414.

[26] J. D. B. FEATHERSTONE, C. P. SHIELDS, B. KHADEMAZAD, AND M. D. OLDERSHAW, *Acid Reactivity of Carbonated Apatites with Strontium and Fluoride substitutions*, Journal of Dental Research, 62 (1983), pp. 1049–1053.

[27] B. H. FELLAH AND P. LAYROLLE, *Sol-gel synthesis and characterization of macroporous calcium phosphate bioceramics containing microporosity.*, Acta biomaterialia, 5 (2009), pp. 735–42.

[28] R. GALLO AND S. TIOZZO, *Vetri per applicazioni biomedicali - Breve analisi dello stato dell'arte nella progettazione dei biovetri*, 2010.

[29] R. GANGULY, V. SIRUGURI, I. K. GOPALAKRISHNAN, AND J. V. YAKHMI, *Stability of the layered Sr3Ti2O7 structure in La1.2(Sr1-xCax)1.8Mn2O7*, J. Phys.: Condens. Matter, (2000), p. 1683.

[30] V. GEETHA AND G. BUVANESWARI, *Ammonium hydrogen difluoride induced fluorination of hydroxyapatite*, Materials Research Bulletin, 45 (2010), pp. 1866–1870.

[31] C. GIACOVAZZO, *Fundamentals of crystallography*, Oxford University Press, Oxford, 2002.

[32] S. GOMES, G. RENAUDIN, A. MESBAH, E. JALLOT, C. BONHOMME, F. BABONNEAU, AND J.-M. NEDELEC, *Thorough analysis of silicon substitution in biphasic calcium phosphate bioceramics: a multi-technique study.*, Acta biomaterialia, 6 (2010), pp. 3264–74.

[33] K. GROSS, *Sintered hydroxyfluorapatites. Part I: Sintering ability of precipitated solid solution powders*, Biomaterials, 25 (2004), pp. 1375–1384.

[34] ——, *Sintered hydroxyfluorapatites. Part II: Mechanical properties of solid solutions determined by microindentation*, Biomaterials, 25 (2004), pp. 1385–1394.

[35] K. GROSS AND K. BHADANG, *Sintered hydroxyfluorapatites. Part III: Sintering and resultant mechanical properties of sintered blends of hydroxyapatite and fluorapatite*, Biomaterials, 25 (2004), pp. 1395–1405.

[36] L. E. L. HAMMARI, A. LAGHZIZIL, P. BARBOUX, K. LAHLIL, AND A. SAOIABI, *Retention of fluoride ions from aqueous solution using porous hydroxyapatite. Structure and conduction properties.*, Journal of hazardous materials, 114 (2004), pp. 41–44.

[37] J. HARRISON, A. J. MELVILLE, J. S. FORSYTHE, B. C. MUDDLE, A. O. TROUNSON, K. A. GROSS, AND R. MOLLARD, *Sintered hydroxyfluorapatites–IV: The effect of fluoride substitutions upon colonisation of hydroxyapatites by mouse embryonic stem cells.*, Biomaterials, 25 (2004), pp. 4977–86.

[38] L. L. HENCH, *Bioceramics: From Concept to Clinic*, Journal of American Ceramic Society, 74 (1991), pp. 1487–1510.

[39] L. L. HENCH AND W. CAO, *Bioactive Materials*, Ceramics International, 22 (1996), pp. 493–507.

[40] L. L. HENCH, D. E. DAY, W. HÖLAND, AND V. M. RHEINBERGER, *Glass and Medicine*, International Journal of Applied Glass Science, 1 (2010), pp. 104–117.

[41] L. L. HENCH, J. W. HENCH, AND D. GREESPAN, *Bioglass(R): A short history and bibliography*, J. Aust. Ceram. Soc., 40 (2004), pp. 1–42.

[42] R. HILL, *The influence of strontium substitution in fluorapatite glasses and glass-ceramics*, Journal of Non-Crystalline Solids, 336 (2004), pp. 223–229.

[43] R. HODGES, N. MACDONALD, R. NUSBAUM, R. STEARNS, F. EZMIRLIAN, P. SPAIN, AND C. MCARTHUR, *The Strontium content of human bones*, J. Biol. Chem, (1950), pp. 519–524.

[44] M. S.-H. HOSSEIN ESLAMI AND M. TAHRIRI, *Synthesis and characterization of nanocrystalline fluorinated hydroxyapatite powder by a modified wet-chemical process*, Journal of Ceramic Processing Research, 9 (2008), pp. 224–229.

[45] M. JOHN AND J. SCHMIDT, *High-resolution hydroxyapatite chromatography of proteins.*, Analytical biochemistry, 141 (1984), pp. 466–71.

[46] P. KANCHANA AND C. SEKAR, *Influence of sodium fluoride on the synthesis of hydroxyapatite by gel method*, Journal of Crystal Growth, 312 (2010), pp. 808–816.

[47] S. KANNAN, F. GOETZ-NEUNHOEFFER, J. NEUBAUER, AND J. M. F. FERREIRA, *Ionic Substitutions in Biphasic Hydroxyapatite and β-Tricalcium Phosphate Mixtures: Structural Analysis by Rietveld Refinement*, Journal of the American Ceramic Society, 91 (2007), pp. 1–12.

[48] S. KANNAN, A. REBELO, AND J. M. F. FERREIRA, *Novel synthesis and structural characterization of fluorine and chlorine co-substituted hydroxyapatites.*, Journal of inorganic biochemistry, 100 (2006), pp. 1692–1697.

[49] S. KATO, H. NAKAGAKI, Y. TOYAMA, T. KANAYAMA, M. ARAI, A. TOGARI, S. MATSUMOTO, M. STRONG, AND C. ROBINSON, *Fluoride profiles in the cementum and root dentine of human permanent anterior teeth extracted from adult residents in a naturally fluoridated and a non-fluoridated area.*, Gerodontology, 14 (1997), pp. 1–8.

[50] H.-W. KIM, Y.-J. NOH, Y.-H. KOH, AND H.-E. KIM, *Enhanced performance of fluorine substituted hydroxyapatite composites for hard tissue engineering.*, Journal of materials science. Materials in medicine, 14 (2003), pp. 899–904.

[51] J. KLIPPEL, *Primer on the rheumatic diseases*, Springer, 2008.

[52] E. LANDI, A. TAMPIERI, G. CELOTTI, AND S. SPRIO, *Densification behaviour and mechanisms of synthetic hydroxyapatites*, J. Eur. Ceram. Soc., 20 (2000), pp. 2377–2387.

[53] E. LANDI, A. TAMPIERI, G. CELOTTI, S. SPRIO, M. SANDRI, AND G. LOGROSCINO, *Sr-substituted hydroxyapatites for osteoporotic bone replacement.*, Acta biomaterialia, 3 (2007), pp. 961–969.

[54] N. H. D. LEEUW, *Resisting the Onset of Hydroxyapatite Dissolution through the Incorporation of Fluoride*, Society, (2004), pp. 1809–1811.

[55] R. LEGEROS AND J. LEGEROS, *Dense Hydroxyapatite*, World Scientific, Singapore, 1993, ch. 9, pp. 139–180.

[56] R. Z. LEGEROS, *Effect of carbonate on the lattice parameters of apatite*, Nature, 205 (1965), pp. 403–404.

[57] R. Z. LEGEROS, R. KIJOWSKA, W. JIA, AND J. P. LEGEROS, *Fluoride-cation interactions in the formation and stability of apatites*, Journal of Fluorine Chemistry, 41 (1988), pp. 53–64.

[58] Y. LI, W. WENG, AND K. C. TAM, *Novel highly biodegradable biphasic tricalcium phosphates composed of alpha-tricalcium phosphate and beta-tricalcium phosphate.*, Acta biomaterialia, 3 (2007), pp. 251–4.

[59] J. LIN, S. RAGHAVAN, AND D. W. FUERSTENAU, *The Adsorption of Fluoride ions by Hydroxyapatite from Aqueous Solution*, Colloids and Surfaces, 3 (1981), pp. 357–370.

[60] C. LIU, Y. HUANG, W. SHEN, AND J. CUI, *Kinetics of hydroxyapatite precipitation at pH 10 to 11.*, Biomaterials, 22 (2001), pp. 301–6.

[61] P. J. MARIE, *Strontium as therapy for osteoporosis*, Current opinion in pharmacology, 5 (2005), pp. 633–6.

[62] P. J. MARIE, P. AMMANN, G. BOIVIN, AND C. REY, *Mechanisms of Action and Therapeutic Potential of Strontium in Bone*, Calcified Tissue International, 69 (2001), pp. 121–129.

[63] M. MATHEW, L. W. SCHROEDER, B. DICKENS, AND W. E. BROWN, *The crystal structure of alpha-Ca 3(PO4)2*, Acta Crystallographica Section B, 33 (1977), pp. 1325–1333.

[64] H. G. MCCANN, *Reactions of fluoride ion with Hydroxyapatite*, J. Biol. Chem, (1952), pp. 247–259.

[65] L. B. MCCUSKER, R. B. VON DREELE, D. E. COX, D. LOUËR, AND P. SCARDI, *Rietveld refinement guidelines*, Journal of Applied Crystallography, 32 (1999), pp. 36–50.

[66] M. MCMASTER, *HPLC, a practical user's guide*, Wiley, Hoboken, 2007.

[67] B. MENZEL, *An infrared study of the hydroxyl groups in a nonstoichiometric calcium hydroxyapatite with and without fluoridation*, Journal of Colloid and Interface Science, 38 (1972), pp. 256–264.

[68] P. J. MEUNIER, C. ROUX, E. SEEMAN, S. ORTOLANI, J. BADURSKI, T. D. SPECTOR, J. CANNATA, A. BALOGH, E.-M. LEMMEL, S. PORS-NIELSEN,

R. RIZZOLI, H. K. GENANT, AND J.-Y. REGINSTER, *The effects of strontium ranelate on the risk of vertebral fracture in women with postmenopausal osteoporosis.*, The New England journal of medicine, 350 (2004), pp. 459–68.

[69] S. MIAO, W. WENG, K. CHENG, P. DU, G. SHEN, G. HAN, AND S. ZHANG, *Sol-gel preparation of Zn-doped fluoridated hydroxyapatite films*, Surface and Coatings Technology, 198 (2005), pp. 223–226.

[70] E. M. MICHIE, R. W. GRIMES, S. K. FONG, AND B. L. METCALFE, *Predicted energies and structures associated with the mixed calcium strontium fluorapatites*, Journal of Solid State Chemistry, 181 (2008), pp. 3287–3293.

[71] I. MOBASHERPOUR, M. HESHAJIN, A. KAZEMZADEH, AND M. ZAKERI, *Synthesis of nanocrystalline hydroxyapatite by using precipitation method*, Journal of Alloys and Compounds, 430 (2007), pp. 330–333.

[72] F. MÜLLER, C. ZEITZ, H. MANTZ, K.-H. EHSES, F. SOLDERA, J. SCHMAUCH, M. HANNIG, S. HÜFNER, AND K. JACOBS, *Elemental depth profiling of fluoridated hydroxyapatite: saving your dentition by the skin of your teeth?*, ACS journal of surfaces and colloids, 26 (2010), pp. 18750–9.

[73] O. NAKADE, H. KOYAMA, J. ARAI, H. ARIJI, J. TAKADA, AND T. KAKU, *Stimulation by low concentrations of fluoride of the proliferation and alkaline phosphatase activity of human dental pulp cells in vitro.*, Archives of oral biology, 44 (1999), pp. 89–92.

[74] K. G. NELSON AND W. I. HIGUCHI, *Mechanism of fluoride uptake by hydroxyapatite from acidic fluoride solutions. I. Theoretical considerations.*, Journal of dental research, 49 (1970), pp. Suppl:1541–8.

[75] H. B. PAN, Z. Y. LI, W. M. LAM, J. C. WONG, B. W. DARVELL, K. D. K. LUK, AND W. W. LU, *Solubility of strontium-substituted apatite by solid titration.*, Acta biomaterialia, 5 (2009), pp. 1678–85.

[76] Y. PANG, *Influence of temperature, ripening time and calcination on the morphology and crystallinity of hydroxyapatite nanoparticles*, Journal of the European Ceramic Society, 23 (2003), pp. 1697–1704.

[77] S. RAMAKRISHNA, M. RAMALINGHAM, T. S. S. KUMAR, AND W. O. SOBOYEJO, *Biomaterials: A Nano Approach*, CRC Press, 2010.

[78] A. C. RAMSEY, E. J. DUFF, L. PATERSON, AND J. L. STUART, *The Uptake of F- by Hydroxyapatite at Varying pH*, Caries Research, 7 (1973), pp. 231–244.

[79] A. RAVAGLIOLI AND A. KRAJEWSKI, *Bioceramica e corpo umano*, Faenza Editrice, Faenza, faenza edi ed., 1984.

[80] G. RENAUDIN, P. LAQUERRIÈRE, Y. FILINCHUK, E. JALLOT, AND J. M. NEDELEC, *Structural characterization of sol-gel derived Sr-substituted calcium phosphates with anti-osteoporotic and anti-inflammatory properties*, Journal of Materials Chemistry, 18 (2008), p. 3593.

[81] H. M. RIETVELD, *A profile refinement method for nuclear and magnetic structures*, Journal of Applied Crystallography, 2 (1969), pp. 65–71.

[82] J. RODRÍGUEZ-CARVAJAL, *An Introduction to the program FullProf 2000*, CEA/Saclay, 91191 Gif sur Yvette Cedex, FRANCE, laboratoir ed., 2001.

[83] L. RODRÍGUEZ-LORENZO, *Influence of fluorine in the synthesis of apatites. Synthesis of solid solutions of hydroxy-fluorapatite*, Biomaterials, 24 (2003), pp. 3777–3785.

[84] L. M. RODRIGUEZ-LORENZO AND K. A. GROSS, *Encapsulation of Hydroxyapatite Microspheres with Fluorapatite Using a Diffusion Process*, Fluoride, 818 (2004), pp. 814–818.

[85] L. M. RODRIGUEZ-LORENZO, J. HART, AND K. GROSS, *Influence of fluorine in the synthesis of apatites. Synthesis of solid solutions of hydroxy-fluorapatite*, Biomaterials, 24 (2003), pp. 3777–3785.

[86] K. SAKAMOTO, *Fluoride ion-promoted reaction of β-tricalcium phosphate to fluoridated hydroxyapatite*, Journal of Fluorine Chemistry, 110 (2001), pp. 75–79.

[87] K. SAKAMOTO, S. YAMAGUCHI, . A. J. ICHIHARA, . A. M. OKAZAKI, Y. T. ÃÃÃ, J. C. E. ÃÃÃÃ, A. E. F. À, AND J. C. ELLIOTT, *Formation of Fluoridated*

Hydroxyapatite by Competitive Attack of OH À and F À ions onto - or -Tricalcium Bis (Orthophosphate), Journal Of The Ceramic Society Of Japan, 12 (2004), pp. 6–12.

[88] L. SINGER AND W. D. ARMSTRONG, *Determination of Fluoride iln Bone with the Fluoride Electrode*, Analytical Chemistry, 40 (1968), pp. 613–614.

[89] M. SIVAKUMAR, *Preparation of hydroxyapatite/fluoroapatite-zirconia composites using Indian corals for biomedical applications*, Materials Letters, 50 (2001), pp. 199–205.

[90] M. A. SPINELLI, F. BRUDEVOLD, AND E. MORENO, *Mechanism of fluoride uptake by hydroxyapatite*, Archives of Oral Biology, 16 (1971), pp. 187–203.

[91] M. A. STRANICK AND M. J. ROOT, *Influence of strontium on monofluorophosphate uptake by hydroxyapatite XPS characterization of the hydroxyapatite surface*, Colloids and Surfaces, 55 (1991), pp. 137–147.

[92] H. TANAKA, A. YASUKAWA, K. KANDORI, AND T. ISHIKAWA, *Surface structure and properties of fluoridated calcium hydroxyapatite*, Colloids and Surfaces, 204 (2002), pp. 251–259.

[93] T. T. THUY, H. NAKAGAKI, K. KATO, P. A. HUNG, J. INUKAI, S. TSUBOI, H. NAKAGAKI, M. N. HIROSE, S. IGARASHI, AND C. ROBINSON, *Effect of strontium in combination with fluoride on enamel remineralization in vitro.*, Archives of oral biology, 53 (2008), pp. 1017–22.

[94] C. J. TREDWIN, *Sol-Gel Derived Hydroxyapatite , Fluorhydroxyapatite and Fluorapatite Coatings for Titanium Implants A thesis submitted for the degree of Doctor of Philosophy by Restorative Dental Sciences London*, (2009).

[95] T. UCHINO, K. YAMAGUCHI, G. KAWACHI, K. KIKUTA, M. KAMITAKAHARA, AND C. OHTSUKI, *Formation of hydroxyapatite on ceramics consisting of tricalcium phosphate in a simulated body fluid*, Journal of the Ceramic Society of Japan, 116 (2008), pp. 96–99.

[96] H. UCHTMANN AND H. DUSCHNER, *Electron spectroscopic studies of interactions between superficially applied fluorides and surface enamel*, J. Dent. Res., 61 (1982), p. 423.

[97] L. VEGARD, *Die Konstitution der Mischkristalle und die Raumfullung der Atome*, Zeitschrift fur Physik, Bd. V. (1921), pp. 19–26.

[98] Y. WANG, S. ZHANG, X. ZENG, L. L. MA, K. A. KHOR, M. QIAN, AND W. E. T. AL, *Initial attachment of osteoblastic cells onto sol-gel derived fluoridated hydroxyapatite coatings*, Journal of Biomedical Materials Research Part A, (2007).

[99] M. WEI, J. H. EVANS, T. BOSTROM, AND L. GRONDAHL, *Synthesis and characterization of hydroxyapatite , fluoride-substituted hydroxyapatite and fluorapatite*, Journal of materials science. Materials in medicine, 14 (2003), pp. 311–320.

[100] J. F. WHITFIELD AND P. MORLEY, *Anabolic treatments for osteoporosis*, CRC Press, 1998.

[101] L. YANG, S. PEREZ-AMODIO, F. Y. F. BARRÈRE-DE GROOT, V. EVERTS, C. A. VAN BLITTERSWIJK, AND P. HABIBOVIC, *The effects of inorganic additives to calcium phosphate on in vitro behavior of osteoblasts and osteoclasts.*, Biomaterials, 31 (2010), pp. 2976–2989.

[102] F. YAO, J. P. LEGEROS, AND R. Z. LEGEROS, *Simultaneous incorporation of carbonate and fluoride in synthetic apatites: Effect on crystallographic and physicochemical properties.*, Acta biomaterialia, 5 (2009), pp. 2169–2177.

[103] M. YASHIMA, *Crystal structure analysis of β-tricalcium phosphate Ca3(PO4)2 by neutron powder diffraction*, Journal of Solid State Chemistry, 175 (2003), pp. 272–277.

[104] Y. ZHAI, K. LI, H. LI, C. WANG, AND H. LIU, *Influence of NaF concentration on fluorine-containing hydroxyapatite coating on carbon/carbon composites*, Materials Chemistry and Physics, 106 (2007), pp. 22–26.

[105] Y. ZHU, X. ZHANG, Y. CHEN, Q. XIE, J. LAN, M. QIAN, AND N. HE, *A comparative study on the dissolution and solubility of hydroxylapatite and fluorapatite at 25Â°C and 45Â°C*, Chemical Geology, 268 (2009), pp. 89–96.

[106] Z. ZHU, H. YU, Q. ZENG, AND H. HE, *Characterization and biocompatibility of fluoridated biphasic calcium phosphate ceramics*, Applied Surface Science, 255 (2008), pp. 552–554.